Aerodynamic Study of Single Stage Multi-Blade Drag-Based Vertical Axis Wind Turbines

A thesis submitted in fulfilment of the requirements for the degree of Doctor of Philosophy

Bavin Raj Loganathan

BEng in Mechanical Engineering

RMIT University

School of Engineering

College of Science, Engineering and Health

RMIT University

July, 2018

DECLARATION OF ORIGINALITY

I, Bavin Raj Loganathan, certify that except where due acknowledgement has been made, the work is that of the author alone; the work has not been submitted previously, in whole or in part, to qualify for any other academic award; the content of the thesis is the result of work which has been carried out since the official commencement date of the approved research program; any editorial work, paid or unpaid, carried out by a third party is acknowledged; and, ethics procedures and guidelines have been followed.

I acknowledge the support I have received for my research through the provision of an Australian Government Research Training Program Scholarship.

Bavin Raj Loganathan

Date: 18/07/2018

Acknowledgements

First of all, I want to express my whole hearted gratitude to my senior supervisor, my mentor, Professor Firoz Alam, for his guidance, encouragement, advice, constructive criticism and assistance. I am also indebted to Dr Harun Chowdhury for his inspiration, support and providing me with innovative ideas to assist in my project.

I owe my heartfelt thanks to my post graduate colleagues whom their moral supports were invaluable during my research. I would also like to express my sincere thanks to Mr Abdul Kadir Ali and Mr Abdulaziz Aldiab for assisting me in my experimental work at RMIT Industrial Wind Tunnel.

I would like to acknowledge the assistance and advice of the technical staff especially Mr Patrick Wilkins and Mr Gil Atkins, School of Aerospace, Mechanical and Manufacturing Engineering. I also acknowledge Mr Julian Bradler and Mr Huw James for his assistance and expertise in data accusation and modelling of the wind turbine blades.

Finally, I must express my sincerest appreciation to my father, Mr Loganathan Arthanary and my mother, Mrs Kunagesvari Murugiah for their encouragement, patience and tolerance during the time it took to complete this work. I would also like to express my sincere appreciation to my sister Ms Mittra Loganathan for her encouragement and support.

Table of Contents

List of Figures

List of Tables

Nomenclature

P_D	Dynamic Pressure (Pa)
Re	Reynolds Number
V	Air Speed (m/s)
μ	Dynamic Viscosity (N.s/m²)
v	Kinematic Viscosity (m²/s)
ρ	Air Density (kg/m^3)

P_{Wind}	Wind Energy (W)
$P_{Turbine}$	Turbine Power Output (W)
F_D	Drag Force (N)
C_D	Drag Coefficient
F_L	Lift Force (N)
C_L	Lift Coefficient
L/D	Lift/Drag ratio
Q	Volume Flow Rate (m^3/s)
$\dot{m}$	Mass Flow Rate (kg/s)
P	Pressure (Pa)
P_T	Total Pressure (Pa)
P_S	Static Pressure (Pa)
A	Cross Sectional Area (m^2)
ω	Angular Velocity (Rad/s)
a'	Tangential Induction Factor
C_P	Power Coefficient
C_T	Coefficient of Torque
T	Torque (N.m)
λ	Tip Speed Ratio
E	Kinetic Energy
U_A	Axial Velocity (m/s)
U	Relative Wind Velocity (m/s)
α	Angle of Attack (0°)
σ	Blade Solidity

θ	Yaw Angle (0°)
$stddev$	Standard Deviation
I_{uu}	Turbulence intensity component
$u^{'}$	Time varying (non-mean) velocity component

List of Abbreviations and Acronyms

CFD	Computational Fluid Dynamics
CSIRO	Commonwealth Scientific and Industrial Research Organisation
HAWT	Horizontal Axis Wind Turbine
HATST	Horizontal Axis Tidal Stream Turbine
OPEC	Organization of the Petroleum Exporting Countries
RET	Renewable Energy Target
RMIT	Royal Melbourne Institute of Technology
TSR	Tip Speed Ratio
IER	Institute for Energy Research
EIA	US Energy Information Administration
WEC	World Energy Council
IEA	International Energy Agency
WNA	World Nuclear Association
BP	BP Statistical Review of World Energy
IGU	International Gas Union
REN21	Renewables Global Status Report
CEC	Clean Energy Council

ABSTRACT

Harnessing wind energy in built-up areas to generate power by a wind turbine for domestic application still remains a challenge despite considerable research has been undertaken in this area. The complex wind conditions in built-up areas, manufacturing complexity and the cost make most wind turbines unattractive for domestic application. For the use in built-up areas, vertical axis wind turbines are preferable due to their omni-directional characteristics, aesthetics, low noise and safety.

Despite having these advantages, most vertical axis wind turbines available in the market are not producing appreciable power. An innovative and low cost vertical axis wind turbine with appreciable power generation capacity can provide a competitive edge to its peer. The primary objective of this study is to develop a micro vertical axis wind turbine suitable for built-up areas.

To achieve this objective, a series of vertical axis wind turbines with multiple blades have been designed, manufactured and studied experimentally. A total of thirteen single stage multi-blade drag-based vertical axis wind turbines (6 with 300 mm diameter, four with 200 diameter and three with 600 mm diameter) with various blade configurations were investigated using RMIT Industrial Wind Tunnel. The blade shape of each turbine is semi-circular with zero twisting. Each turbine's rotational speed (RPM), torque (T) and power (P) were determined under the wind speed ranging from 4.5 m/s (16 km/h) to 8.5 m/s (31 km/h). Smoke and wool tuff flow visualisations techniques were used to understand airflow characteristics in and around each prototype turbine. For each prototype wind turbine, a graphical relation between power and rotational speed, power coefficient and tip speed ratio, and maximum torque and number of blades were constructed. The effect of wind turbulence on power output has also been studied.

At all speed range studied, the 300 mm diameter turbine with 32 blades produced highest torque and power amongst all 300 mm diameter configurations. Similarly, the 200 mm diameter turbine with 19 blades generated highest torque and power amongst 200 mm diameter turbines. An empirical relationship has been established to determine the optimal blade number for a constant diameter multi-blade single stage drag-base vertical axis wind

turbine. The experimental data obtained for two different diameter prototype turbines have confirmed the validity of the developed empirical relationship.

Power is highly dependent on blade number and blade spacing. With the increase of blade number, the power increases till it reaches an optimal blade number thereafter it starts to decrease. The optimal blade spacing was determined to be in between 5.5 mm and 6.5 mm for all turbines studied.

A flow enhancing device (cowling) was designed and employed to explore its effectiveness on turbine rotational speed (RPM) and torque. The flow enhancing device had shown a positive impact on the turbine RPM however, the overall torque and power was found to be lower compared to turbines without its employment.

Wind turbulence intensity has significant impact on power output. The power decreases with an increase of turbulence. However, the airflow rate or volume flow rate has much higher impact on the power output.

The power can be increased by approximately two times when the blade diameter is scaled up. Doubling the blade diameter increases the amount of wind energy the turbine blades are able to extract. However, it is found that the power output does not increase proportionally as the optimal power output depends on a) blade number, b) blade spacing, c) blade angle, d) turbulence intensity, and e) airflow rate.

In an open environment, small scale vertical axis wind turbine blades can experience wind with varied gustiness due to variety of structures. This can have effect on aerodynamic parameters optimised in controlled wind conditions in the wind tunnel. Therefore, it would be useful to undertake a field study to determine the wind gustiness effect on power output.

CHAPTER 1

Background and Literature Review

In this chapter an overview of global power generation scenario with focus on renewable wind power generation by turbines is presented with particular references to drag based vertical axis wind turbine. Relevant wind turbine theory and background literature are also presented and the Chapter concludes with major objectives and layout of the work.

1.1 Current Global Power Generation

As global economic growths increases, developing countries led by China and India are increasingly looking at various energy sources to fuel their growth. The need for power to fuel the economic growths has put tremendous pressure on concerned bodies' responsibility to protect the environment at the same time ensuring low energy cost.

The cheapest source of power is from nuclear generation at 2 cents per kilowatt hour (IER, 2012). However, higher construction cost and safety fears due to radiation have made nuclear energy unattractive to common masses. Power generation by coal remains the dominant method in most countries due to its low generation and construction cost. The coal power generation cost is around 2.5 cents per kilowatt hour. The construction cost is about 2 times lower per kilowatt equivalent compared to nuclear power plant (EIA, 2016), (WNA, 2018). Among the renewable sources, hydro power is the cheapest to generate at 4 cents per kilowatt hour. Wind energy is nearly 2 times cheaper to generate compared to solar per kilowatt hour (based on 24% capacity) as shown in Table 1.1. Cost of generating from solar photovoltaic on residential house rooftops is 20 cents per kilowatt hour making it the most expensive power source (IRENA, 2018).

Table 1.1: Per Unit Cost of Power in 2016

	Construction cost † (AUD/kWhe)	Generation Cost (AUD¢/kWh)	Life with rated efficiency (years)
Coal	1000	2.5	50
Gas	400	4.0	25
Nuclear	3000	2.0	80
Micro -Hydro	1000	4.0	20
Wind	6000	6.0	20
Solar			
-based on 24% capacity	-	15	20
-based on 9% capacity	-	20	-

† kilowatt hour equivalent

The coal consumption for power generation has increased by 64%, led by economic growths in China and India since 2000. The global power generation by coal is around 41% of the total global power generation of 23,816 TWh in 2015, as shown in Figure 1.1 (REN21, 2017). The power generated by natural gas is around 22% followed by liquid fuel at 4%. In 2016, nearly 79% of the world power is generated by fossil fuel (REN21, 2017), (EIA, 2016) and (IEA, 2016). Till to date, coal remains a major primary source of energy in the world due to its low cost. Among the non-fossil energy source, hydro power is 16% of total global power followed by nuclear energy at 11%, wind power at 3%, biomass at 2% and solar power at around 1% (EIA, 2016) and (IEA, 2016).

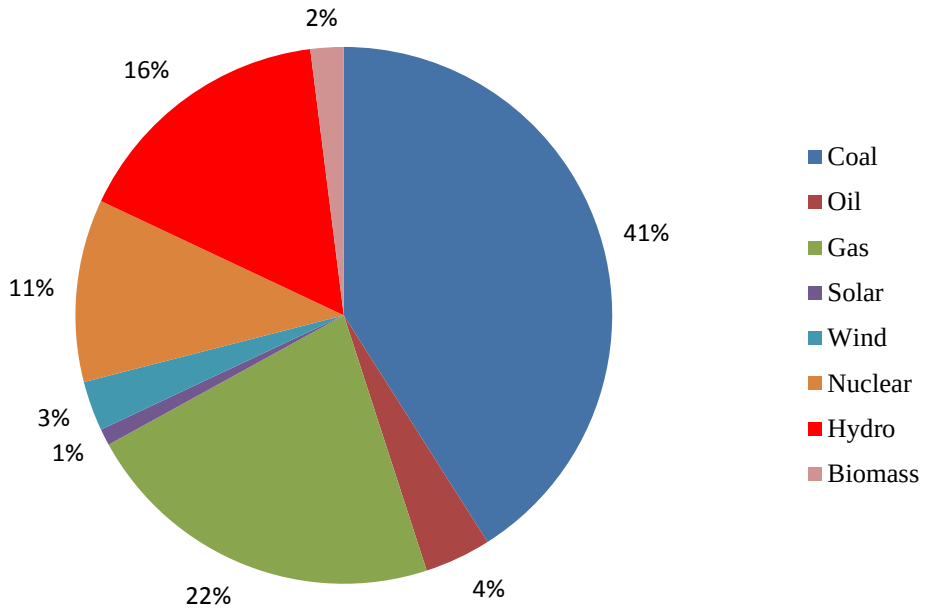

Figure 1.1: Global power production in 2016 (adapted from REN21, 2017)

The power sector is responsible for around 25% of global greenhouse emissions. The global average per capita power consumption in 2016 is around 2,674 kWh as shown in Figure 1.2. The per capita power consumption varies significantly based on household income, weather condition, house size, appliance standards and environmental consciousness. For example, the average Norwegian household used in 2016 about 25 times more power than a typical developing country's household which uses around 1000 kWh per year and approximately 4.5 times more power than a typical European home (WEC, 2017). This is because Norway remains one of the few countries where electricity is the main heating source. The main heating source for about 73% of the households is based on electricity, either by electric space heaters (48%), electric floor heating (7%), air heat pumps (21%) or central heating with electricity (Statistics Norway, 2016). With the rapid increase of economic prosperity and household income in developing countries, the demand for power is also increasing. This results in more greenhouse gas emission as most power currently generated is from fossil fuels (coal, gas and liquid fuel). At present, the residential sector consumes over one-third of the total power consumption (WEC, 2017).

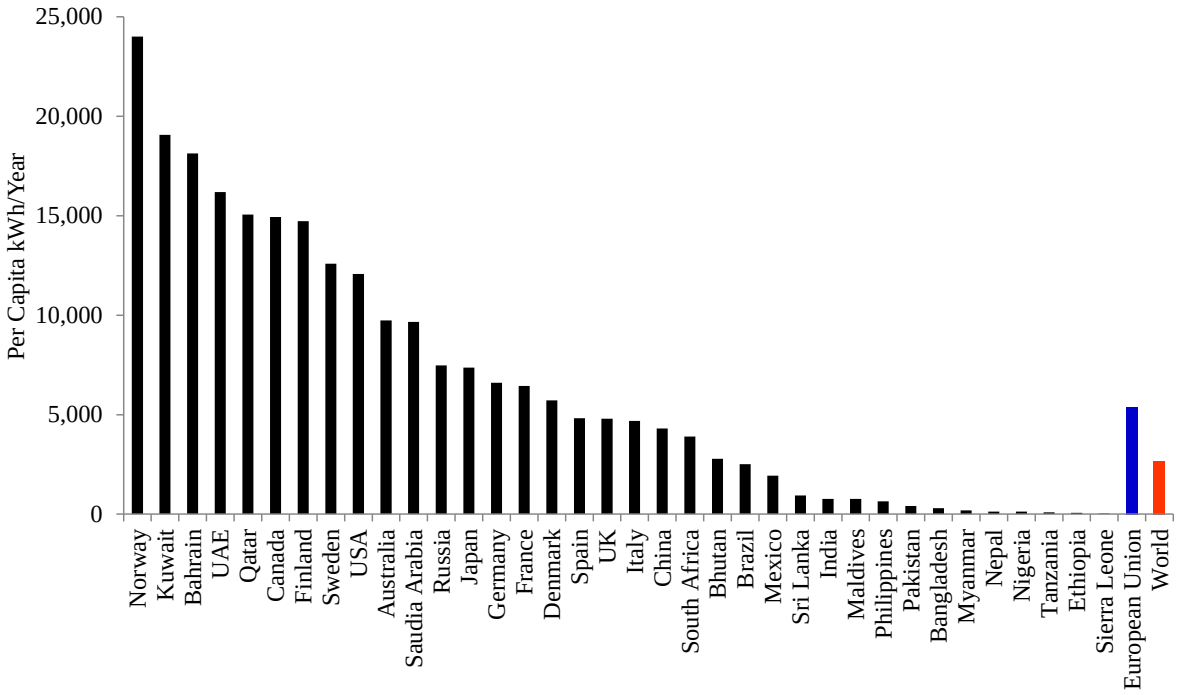

Figure 1.2: Per capita power consumption for selected countries in 2016 (adapted from WEC, 2017)

The world's total power generation in 2016 was 23,816 TWh (IEA, 2016) and (Enerdata, 2016) out of which 4% by liquid fuel, 22% by natural gas and 41% by coal. The remaining 33% are generated by nuclear and renewable energy sources (16% by hydro, 11% by nuclear, 3% by wind, 1% by solar and 2% by biomass) (IEA, 2016) and (EIA, 2017). It is estimated based in reserve to production ratio, liquid fuel, natural gas and coal will be depleted by 2068, 2070 and 2170 (BP, 2016), (EIA, 2017) and Abas et al. (2015).

1.2 World's Liquid Fuel Production

The current world reserve of crude oil is 1,726,685 million of barrels (MMbbl) and the production is around 80,622,000 (bbl/day) (EIA, 2017). The major reserves are located in Saudi Arabia, Venezuela, Canada, Iran, Iraq and Kuwait. The oil exporting countries have created an organisation "Organisation of the Petroleum Exporting Countries (OPEC)" to have an edge in global oil market dominance. The OPEC members are Algeria, Angola, Ecuador, Iran, Iraq, Kuwait, Libya, Nigeria, Qatar, Saudi Arabia, United Arab Emirates and Venezuela which accounted for the highest global crude oil export at nearly 49% in 2016. The top ten oil

exporting countries are shown in Figure 1.3 (REN21, 2017). These countries account for two-thirds of global oil exports. Saudi Arabia is the largest crude oil exporter accounting for nearly 20.1% of global exports and is nearly double the second largest exporter Russia which account for nearly 11% of global exports. Saudi Arabia exported nearly 7,165 000[1] bbl/day in 2015. The third largest exporter is Iraq which contributes 6.8% of global exports. Canada, UAE, Kuwait, Iran, Nigeria, Angola and Norway each accounted for 5.8%, 4.5%, 4.3%, 4.0%, 3.7% and 3.3% of global oil exports (REN21, 2017). Russia, Canada and Norway are non - OPEC member oil exporting countries.

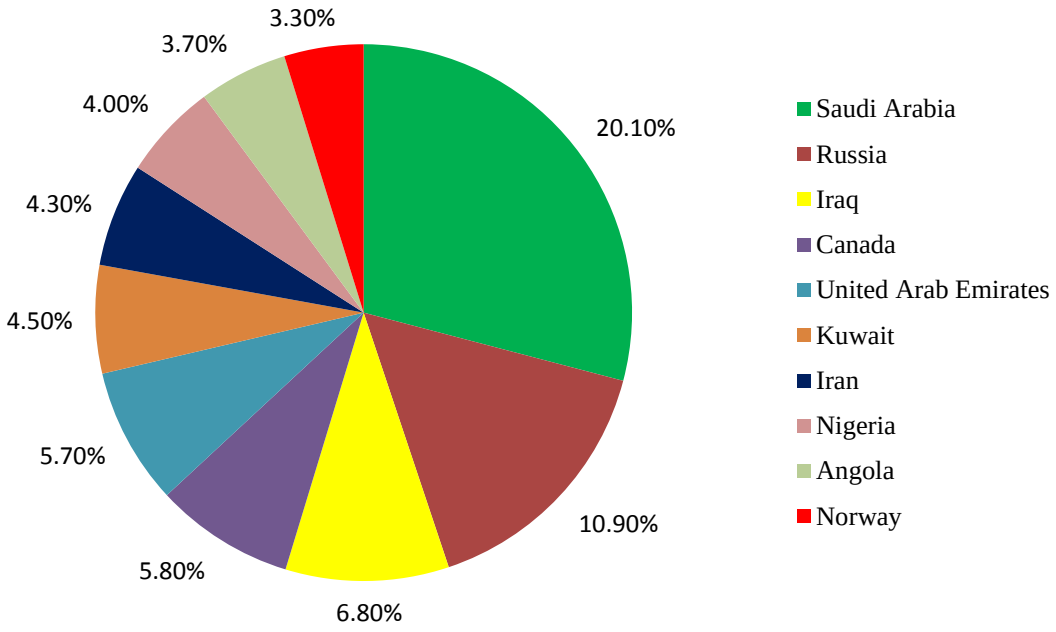

Figure 1.3: Crude oil exports market share by country in 2016 (adapted from REN21, 2017)

According to International Energy Agency (2017), the worldwide demand for crude oil for power generation is projected to decline due to high cost of liquid fuel and the falling cost of renewable source of energy and the world-wide push to tackle climate change and improve air quality and the rise of US shale gas output. Crude oil is being replaced by natural gas, renewables (hydro, wind solar and solar) and nuclear energy in power generation.

[1] Barrel per day (bbl/day)

[2]Current OECD member States: Australia, Austria, Belgium, Canada, Chile, Czech Republic, Denmark, Estonia, Finland, France, Germany, Greece, Hungary, Iceland, Ireland, Israel, Italy, Japan, Korea, Luxembourg, Mexico, the Netherlands, New Zealand, Norway, Poland, Portugal, Slovak Republic, Slovenia, Spain, Sweden,

1.3 Global Coal Scenario

The world's current coal deposits are estimated to be around 816 billion metric tons (WEC, 2016). The major coal deposits are in US, Russia, China, India and Australia. Coal currently supplies 41% of global electricity and is expected to grow in coming decades (WEC, 2016).

The leading coal exporters accounted for nearly 95% of all coal exports in 2016. The top ten coal exporting countries are shown in Figure 1.4 (REN21, 2017). The largest coal exporter was Australia, which exported nearly 463 million tonnes (Mt) in 2016 or nearly 38.3% of total global coal exports which is nearly double the second highest coal exporting country Indonesia. Indonesia exported nearly 17.4% followed by Russia at 12%. United States, Colombia, South Africa, Canada, Netherlands, North Korea and Mongolia accounted for 6%, 5.9%, 5.2%, 4.5%, 3.2%, 1.6% and 1.3% of total coal exports respectively (REN21, 2017), (IEA, 2016) and (EIA, 2017).

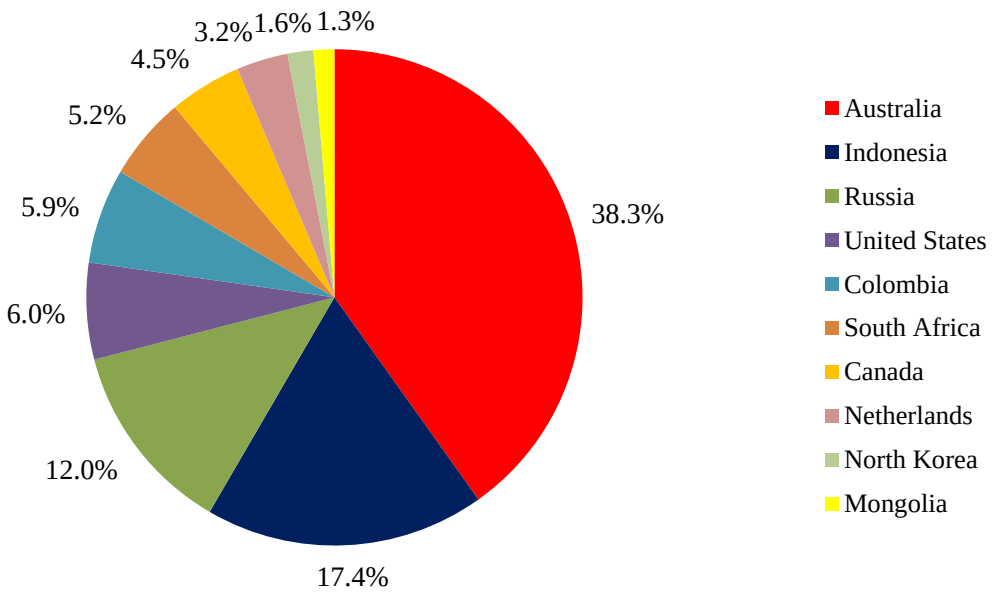

Figure 1.4: Coal exports market share by country in 2016 (adapted from REN21, 2017)

According to US. Energy Information Administration (2017), the global coal use is projected to remain flat. The total coal demand in Organisation for Economic Co-operation and Development (OECD)[2] regions and China is predicted to decline offsetting the growth in India and other non-OECD Asian nations.

In order to reduce the dependency on coal and environment pollution, the use of natural gas for power generation is increasing rapidly. Currently, generation by natural gas is around (21.6%) (IEA, 2016) and (EIA, 2017). Most peaking power generation in developed countries (Australia, USA, and UK) is undertaken by natural gas. However, due to limitation of access to other fuels, some countries fully or over 80% of their power generation are achieved by using gas (Qatar, United Arab Emirates, Bangladesh, and Nigeria) (IEA, 2016). The fast developing nations and some developed nations in Asia use natural gas for power generation. These countries do not have enough gas from their domestic source. Hence they import gas from foreign countries as Liquefied Natural Gas (LNG) to make easier transportation.

1.4 Power Generation by Natural Gas

The countries that do not have access to their own natural gas are importing natural gas by pipeline (if geographically possible) and natural gas as liquid form (e.g. Liquefied Natural Gas - LNG). Natural gas accounts for around 23% of the world's power generation around 5579 TWh (EIA, 2017). Gas in the form of LNG is the easiest means to import as these regions are not easily served by pipelines. Japan remains the world's largest importer of LNG around 30% of the world's LNG import followed by South Korea (15%), Taiwan (5%), China (4%) and India (3%).

LNG accounted nearly three-quarters of capacity growth between 2000 and 2017 in developed economies. The shift towards gas power generations is due to lower capital cost and shorter project lead times compared to coal and nuclear power plants. Furthermore,

[2]Current OECD member States: Australia, Austria, Belgium, Canada, Chile, Czech Republic, Denmark, Estonia, Finland, France, Germany, Greece, Hungary, Iceland, Ireland, Israel, Italy, Japan, Korea, Luxembourg, Mexico, the Netherlands, New Zealand, Norway, Poland, Portugal, Slovak Republic, Slovenia, Spain, Sweden, Switzerland, Turkey, UK, and US.

flexibility in providing either peak or base load power or supplement to intermittent renewable source makes it an attractive energy source.

The use of Liquefied Natural Gas (LNG) for power generation has been rapidly increasing as an alternative to coal. The leading top ten exporters accounted for nearly 59% of total global exports in 2016. The order of top five exporters by share is Qatar (29.9%), Australia (17.2%), Malaysia (9.7%), Nigeria (7.2%), Indonesia (6.4%), Algeria (4.5%), Russia (4.2%), Trinidad (4.1%), Oman (3.2%) and Papua New Guinea (2.9%) (IGU, 2017). The total exports in Million Ton Per Annum (MTPA) are shown in Figure 1.5. Australia export is a nearly half of Qatar's export but is expected to surpass Qatar by 2021.

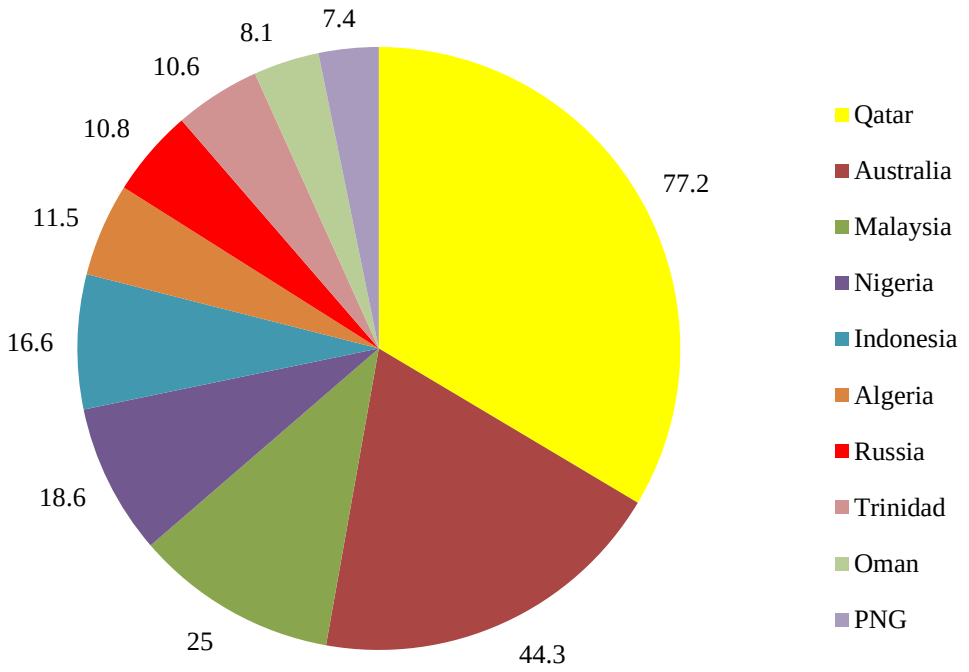

Figure 1.5: Renewable energy share of global power production in 2016 (adapted from IGU, 2016)

LNG is Natural Gas cooled down to condensate at around -161 °C. Natural gas consists primarily of methane. Impurities and heavy hydrocarbons from the gas fuel are removed before the cooling process. The volume of the liquid gas is approximately 1/600th of the gaseous volume at atmospheric conditions. It is odourless, colourless, non-toxic and non-corrosive. LNG is cost efficient to transport over long distances where pipelines do not exist. A typical LNG shipment infrastructure (ship terminal, storage and liquefaction trains) is shown in Figure 1.6.

Figure 1.6: A LNG transportation network at Gladstone in Queensland, Australia by ship (adapted from ABC, 2016)

LNG consumption is predicted to increase by over 40% from 2015 to 2040 (IGU, 2017) out of which power generation is responsible for nearly 75% of the increase. LNG fired power plants are attractive due to low capital cost, favourable heat rates and relatively low fuel cost. However, the energy usage for gas liquefaction plant and high risk factors include flammability after vaporization into a gaseous state, freezing and asphyxia are still a major concern, World Energy Outlook- IEA (2016) and (EIA, 2017). Another important issue is that the price of LNG is tagged with the international price of crude oil. Hence, there is an unpredictability of the price.

1.5 Future Primary Energy Source

By 2060, the global power generation will increase to 44,914 TWh, an increase of around 89% when compared to 2015 (WEC, 2017). The non-fossil energy source is predicted to provide around 54% of the total global power generation as shown in Figure 1.7. Nuclear and hydro power sector is expected to lead the way with 15% each followed by wind, solar and biomass at 13%, 7% and 4% respectively. Gas and coal are projected to be major contributor from fossil fuel sources at 27% and 18% respectively (IEA, 2016) and (EIA, 2017).

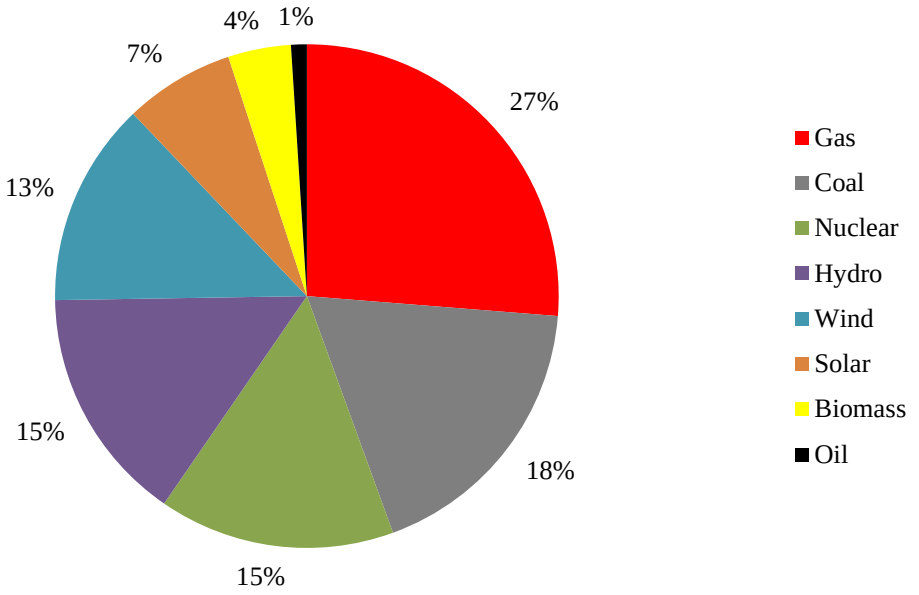

Figure 1.7: Future global power production in December 2060 (adapted from WEC, 2016)

The demand for oil is projected to experience reduction in coming years due to Paris Agreement[3] which aims to stabilize the global average temperature and limit greenhouse gas emissions. Unless new oil reserves are discovered, fossil fuel is projected to deplete by 2060 at current world energy consumption rate.

[3] The Paris Agreement entered into force on 4 November 2016, thirty days after the date on which at least 55 Parties to the Convention accounting in total for at least an estimated 55 % of the total global greenhouse gas emissions have deposited their instruments of ratification, acceptance, approval or accession with the Depositary.

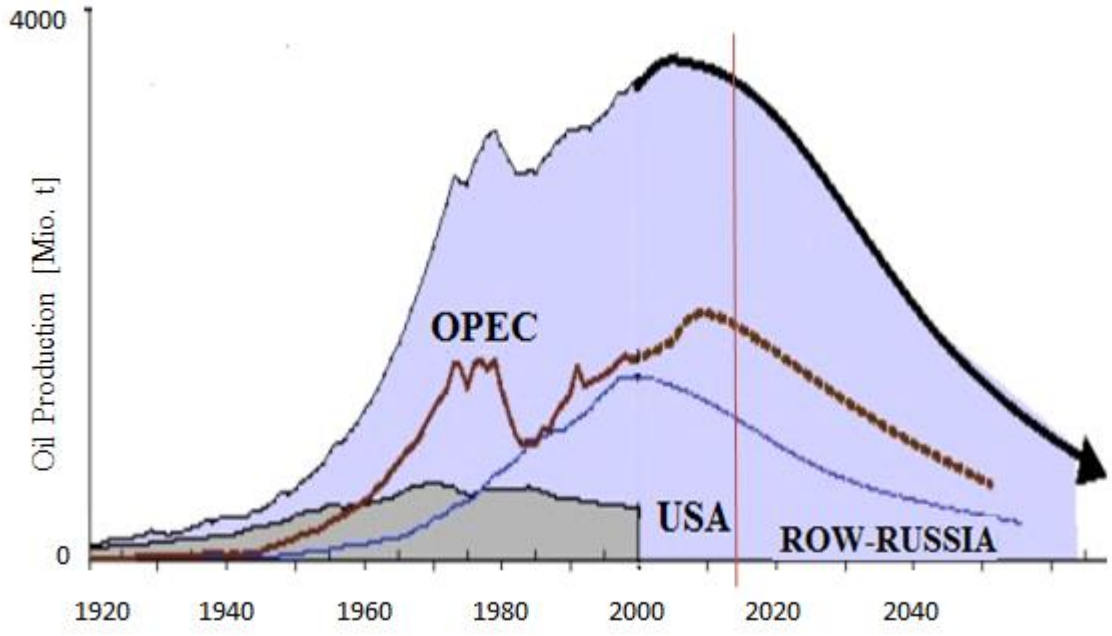

Figure 1.8: World oil production forecast (adapted from L-B-Systemtechnik, 2008)

The peak and decline of oil production countries are shown in Figure 1.8. The USA's oil production peaked in the 1970s followed by steady decline in oil production. Russia's crude oil production peaked in 2000s while OPEC regions crude oil production peaked in 2010s. Global crude oil production is expected to follow similar pattern. Coal is forecast to fuel 18% of the total global power production by 2060. Since 2000, coal consumption for power has increased by 64%. As mentioned previously, coal remains a major primary source of energy in Asia due to low cost which is around (2.5 ¢ per kWh) and is expected to be the main power source in the foreseeable future (WEC, 2016).

The use of Nuclear Power is on the rise globally. In 2015, 65 nuclear reactors for power generation were under construction with a total capacity of 64,000 MW. Forty of such units under construction were located in four countries: China, India, Russia and South Korea. Liquefied Natural Gas (LNG) is expected to play a role in power generation. However the price tag of LNG with Liquefied fuel (e.g. Crude oil) has made LNG a cost vulnerable for power generation.

1.6 Power Generation by Renewable Energy

Although hydro resources currently dominate in renewable power generation, it is expected by 2060, non-hydro renewable energies will represent between 21% to 42% of future power generation mix (REN21, 2017). Nearly 24.5% of global power production in 2016 came from renewable energy, with 16% coming from hydropower, 3% from wind power, 2% from bio fuel (ethanol, methanol, biodiesel from algae especially from (3rd generation biogas) and 1% from solar panels as shown in Figure 1.9. Other renewable (ocean, concentrated solar power (CSP) and geothermal power) accounted for another 0.4% (REN21, 2017).

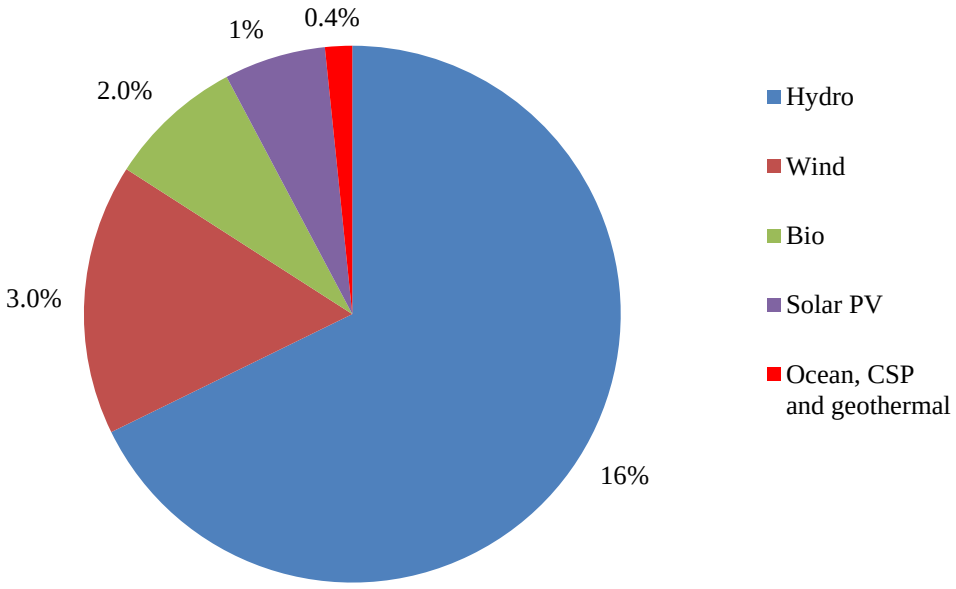

Figure 1.9: Renewable energy share in 2016 (adapted from REN21, 2017)

1.6.1 Power Generation by Hydro Energy

The utilisation of hydro energy has been a popular for many decades. Hydropower produced nearly 1,096,000 MW or 16.6% of total global power production in 2016. China is the largest hydropower generating country. It accounts for 28% of the global hydropower capacity,

followed by Brazil, USA and Canada at 9%, and India and Russia at 4% which together accounted for about 62% of installed capacity at the end of 2016. Global hydropower generation was estimated to be 4102 TWh in 2016, up about 3.2% over 2015. The 'Three Gorges Dam' that spans the Yangtze River in China is shown in Figure 1.10. It is the world's largest hydro power plant in terms of installed capacity. The 'Three Gorges Dam' installed capacity is 22,500 MW (Thomson Reuters Corporation, 2017).

Figure 1.10: The Three Gorges Dam, China (adapted from Business Insider, 2015)

Hydropower is relatively clean and can be used as cheap flood control (primary reason for dams). Dam is constructed for storing water to generate hydraulic head. The main parameter of hydro resources viability for power generation is hydraulic Head (h). Hydraulic head is defined as the difference between the headwater level in the reservoir upstream of the dam and the tail water level below the hydroelectric dam. It represents the amount of energy that can be transformed into electricity by the turbines and generators. A typical hydro power plant layout and its basic components are shown in Figure 1.11. The higher the water level, the more potential energy that the water has.

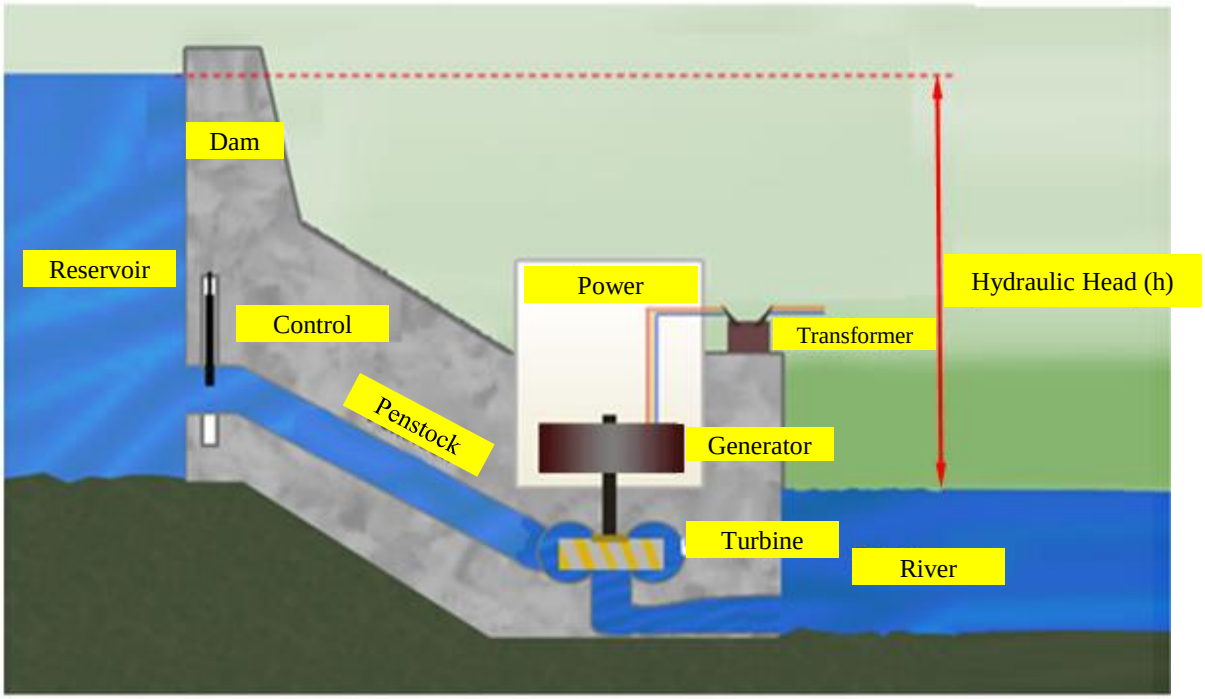

Figure 1.11: A typical hydro power plant layout (adapted from US Geological Survey, 2015)

The control gate allows water to flow through the penstock to the turbine. The control gate controls the volume of water to the turbine. The turbines are coupled to an electrical generator. Kinetic energy from the water drives the turbine coupled to the electrical generator producing electrical power.

However potential power output is limited globally to about 5 to 10% of energy needs. Its dependability is an issue due to prolonged droughts and seasonal variability that can cut power production severely. Furthermore dams have drawbacks, including loss of nutrient flow down river, loss of sediment flow down river, flooding of scenic, farming areas and ecosystem downstream and upstream, Cresswell et al (2009). Hence, power generation by wind currently remains a viable true renewable energy source for power generation.

1.6.2 Power Generation by Solar Photovoltaic (PV) Cells

Solar installed capacity globally has reached approximately 227,000 MW in 2016, equivalent to producing 1% of the power used globally. China is the global leader accounting for 27% of global Solar PV followed by Japan accounting for 15% and Germany, 11.5%. The top three countries account for nearly half the global power generation by solar PV. China alone added nearly 80% in total solar PV capacity in 2016 compared to previous year. Solar PV installation is expected to increase every year, REN21 Renewables Global Status Report (2017).

Figure 1.12: Solar PV on a residential house rooftop in Australia

Energy from the sun has some advantages. The surface of the earth receives 120,000 terawatts of solar radiation (sunlight) – 20,000 times more power than the planet needs. As the solar panel does not have any moving parts, its applications are desirable in built-up areas. A typical residential rooftop solar PV layout is shown in Figure 1.13.

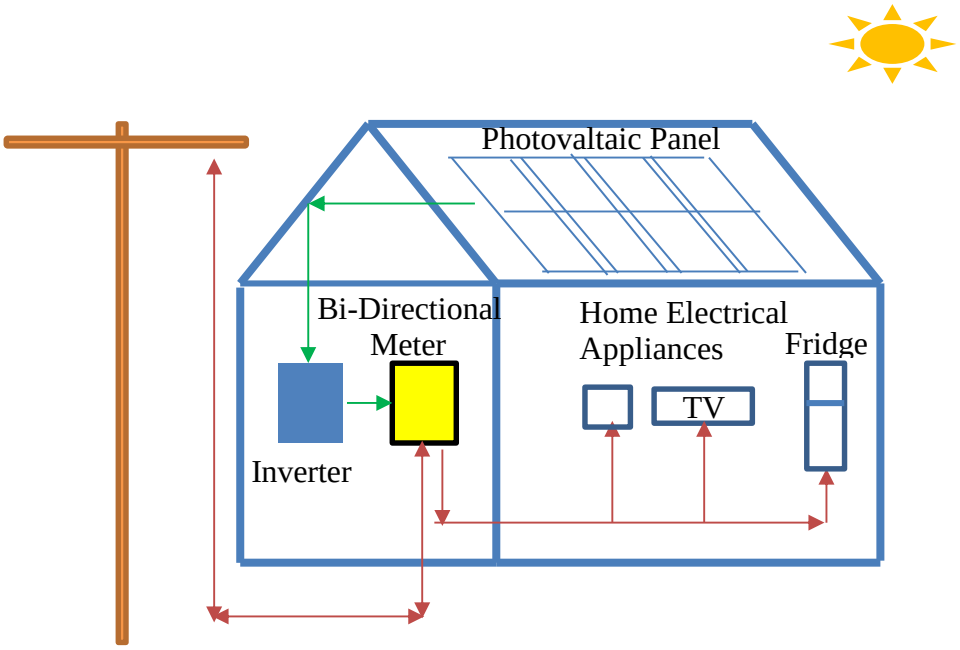

Figure 1.13: A typical residential rooftop Solar PV layout

The photovoltaic (PV) panels convert sun's rays into power by exciting electrons in silicon cells. The power produced is direct current (DC). The inverter is used to convert the DC power to alternating current (AC) as most home appliances use AC power. The power from the inverter is then passed through the bi-directional meter. Bi- directional meters measures electricity flow in two directions. It's used to measure how much power is consumed and also how much power is fed back into the power grid.

Although the cost of solar power generation has been decreasing, it is still the most expensive renewable energy source for generating power. The cost of power is 15 cents per kilowatt hour (kWh) based on 24% capacity. Whereas, the cost of wind power is 6 cents. It is nearly two and a half times more expensive than wind power. Moreover, the need for large areas to set up solar panels and the recyclability of solar panels after the end of use has an enormous impact on the environment. Furthermore, solar energy is an intermittent energy source. Access to sunlight is limited at certain times (e.g. night). This requires a large backup generating capacity and poses challenges to grid reliability. These unpredictability are the reason why solar power is not first choice when it comes to meeting the base load power demand.

1.6.3 Wind Energy

Wind energy is the second largest renewable energy source (4%), behind hydro energy (~17%) for power generation. The global wind power capacity in 2016 is nearly 487,000 MW as shown in Figure 1.14. China is the largest wind power producing country with 168,732 MW which equates to around 34.7% of the total world wind power generation capacity. USA is the second largest wind power producing country with 82,184 MW, followed by Germany, India, Spain, United Kingdom, France, Canada, Brazil and Italy which combined produce 84% of the total world wind generated power (REN21, 2017) and (IEA, 2016).

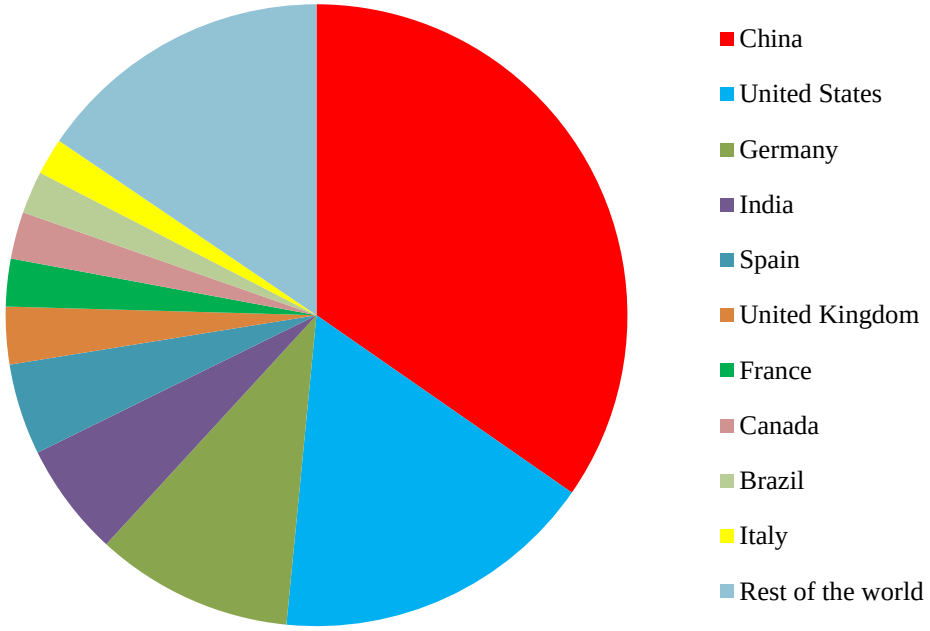

Figure 1.14: Global wind power installed capacity in 2016 (adapted from REN21, 2017)

The total global wind power capacity from 2008 to 2016 is shown in Figure 1.15 (REN21, 2017). Almost 55,000 MW of wind power (12%) capacity was added since 2015. China alone added 23,400 MW followed by US with 8,200 MW and Germany with 5,000 MW of wind power. UK, France, Canada, Brazil and Italy added 0.7, 1.6, 0.7, 2 and 0.3 MW respectively. The global estimated wind power capacity from small scale wind turbines is about 948 MW in 2015 (Pitteloud and Gsänger, 2017). The World Energy Association (WEA) (2016) estimates that China, US and UK represent around 84% of global small wind power

generation capacity. The small wind energy market is forecasted to achieve a cumulative installed capacity of about 1,900 MW by 2020 (Pitteloud and Gsänger , 2017).

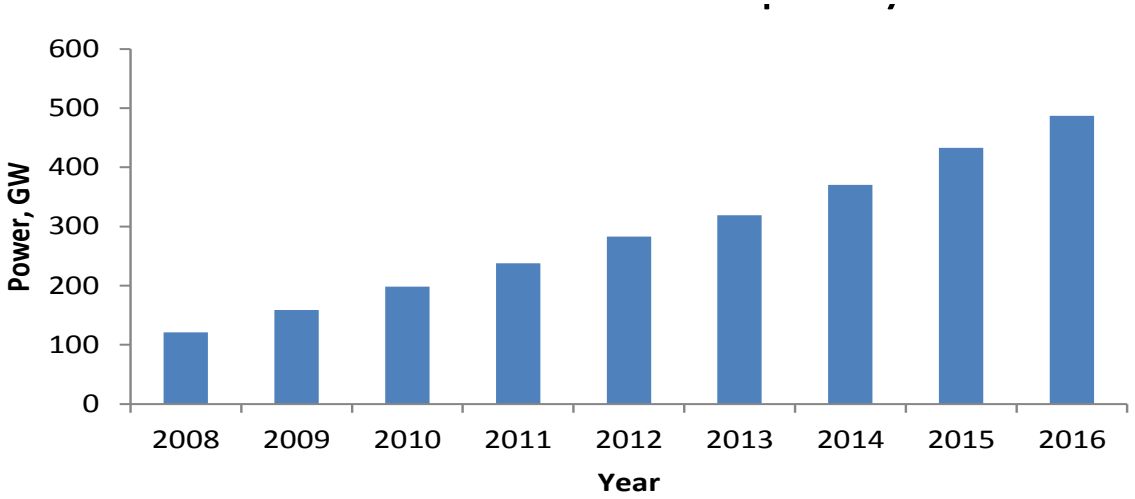

Figure 1.15: Global wind power growth from 2008 to 2016 (adapted from REN21, 2017)

At present, the residential sector consumes over one-third of the total global generated power (WEC, 2016) and (REN21, 2017). Hence, the use of renewable wind energy available in the built-up areas for power generation can reduce the dependency on fossil-fuel generated power for household application and the greenhouse gas emission.

For example, over 90% population of Australia live along the coastal belt which has proven vast wind resources as shown in Figure 1.16. The average wind speeds in urban areas is around 3-4 m/s. This provides unique opportunities for domestic scale wind turbines utilisation to harness the wind energy for power generation in residential areas. The average wind speed in Australian Costal areas varies from 4 m/s to 8 m/s. The average wind speed in Australian Southern Coastal areas is around 6-8 m/s which are ideal for commercially power generation.

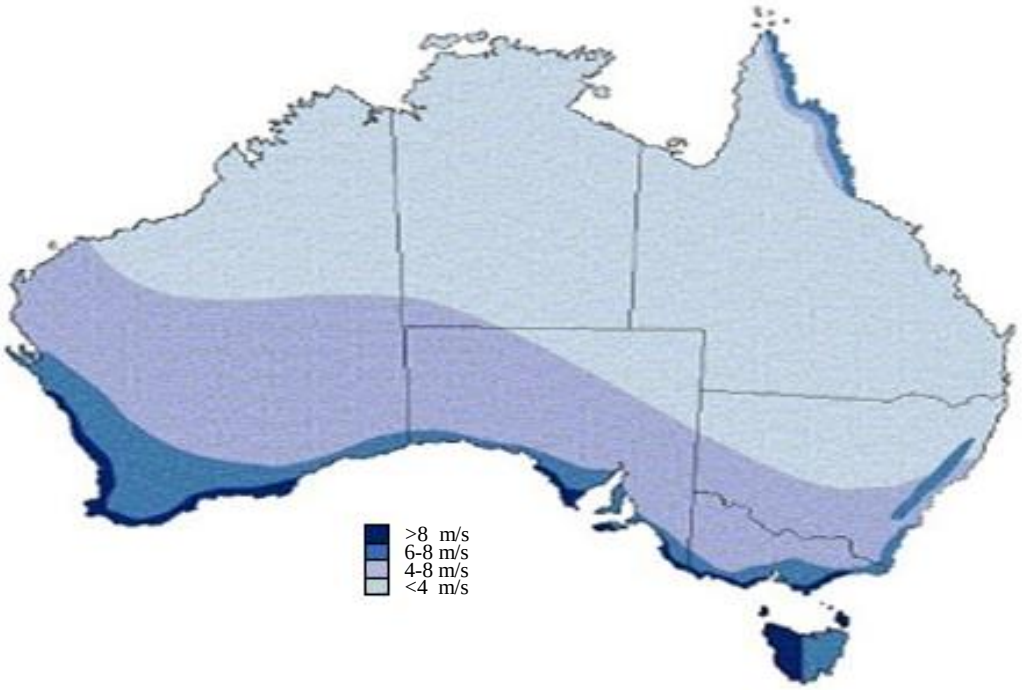

Figure 1.16: Australian wind map (adapted from Wind Resource Assessment in Australia-A planners guide, 2003)

Majority of current installed wind farms in Australia are situated along the 26,000 km costal belts as shown in Figure 1.17. The red doted circle in Figure 1.17 indicates the location of commercial wind farms with turbines. In 2016, nearly 79 wind farms was established in Australia contributing nearly 4,327 (MW) of installed power, which accounts for 5.3% of Australia's total power demand (12,903 GWh) (CEC, 2016). Most commercial wind power farms in Australia use Horizontal Axis Wind Turbines (HAWTs) between 1.5 to 3 MW generation capacities (CEC, 2016). Wind power is the second highest renewable source accounting for about 30% of the total percentage of renewable generation. Power is dispatched to consumers through transmissions. The transmission over long distances creates power losses. The overall losses between the power plant and consumers are around 10%. Each wind farms generally possesses around 15-140 wind turbines capable of producing 21 MW to 420 MW of power.

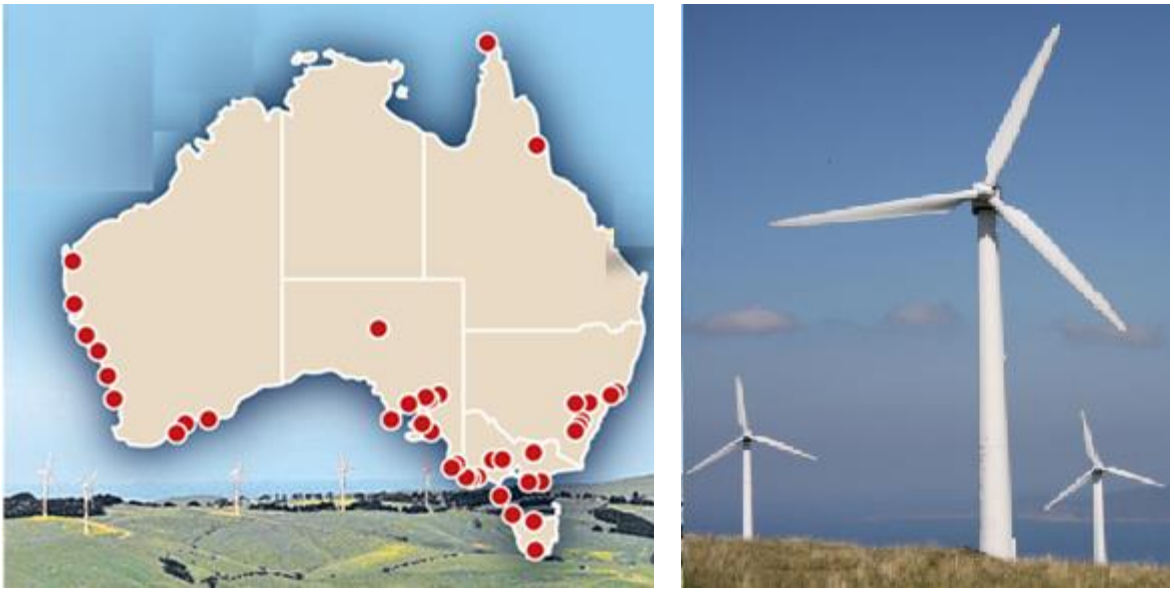

Figure 1.17: Australian wind farms (adapted from Coppin, 2003)

Power generation from urban resources using solar panels and wind turbines is a promising alternative renewable power source to minimize losses through power lines and minimising air pollutions. Solar panels have the advantage of being silent as there are no moving parts compared to wind turbines. However, solar panels only generate power during day time. Furthermore, silicone used in the panels is expensive. Alternatively, wind turbines generate power throughout the day. They are cheaper compared to solar power generation. Hence, power generation from urban wind resources using horizontal axis wind turbines (HAWTs) and vertical axis wind turbines (VAWTs) is a viable alternative renewable power generation.

1.7 Process of Wind Power Generation

Wind turbines extract kinetic energy from wind and convert it to power. The kinetic energy in the wind is used to rotate blades around a rotating shaft (rotor). It is not possible to harness all of the available kinetic energy as the wind needs to move from the turbine and it can never slow down to zero velocity. The maximum power that can be harnessed is governed by Betz law. Detailed explanation about Betz law is given in Section 1.10. Therefore, at 4 m/s wind speed, the maximum power that a turbine can extract from the wind is 59.3% of 38W per square metre of swept blade area, or 22.8W for a $1m^2$ turbine as shown in Figure 1.18. The

maximum power in comparison with larger diameter typically used in commercial wind turbines are shown in Figure 1.19. It can be observed that at 5 m/s wind speed (typically encounters in built-up arrears), a 20 m diameter turbine can produce 400 times more power compared to a 1 m diameter turbine.

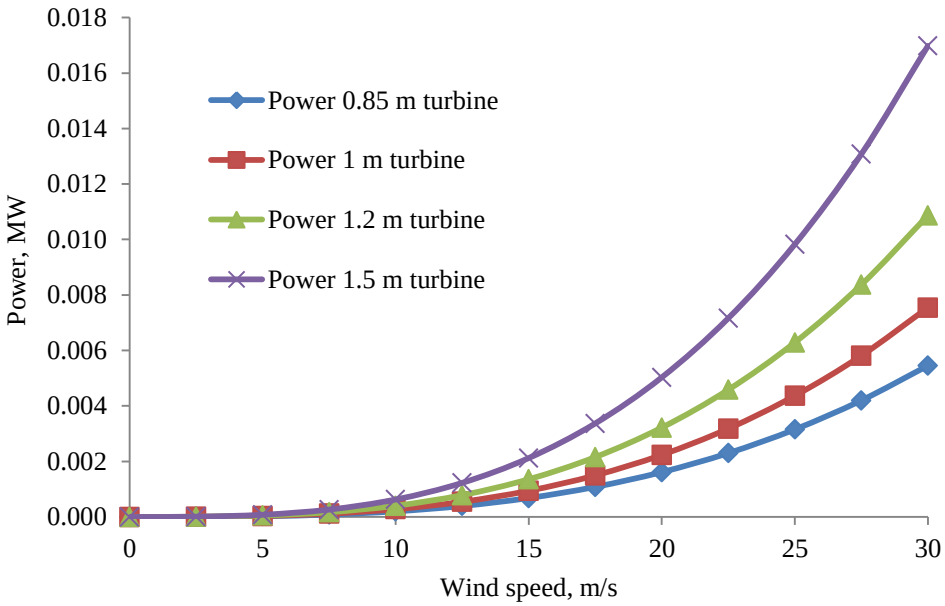

Figure 1.18: Maximum power from small scale turbines with Betz Limit

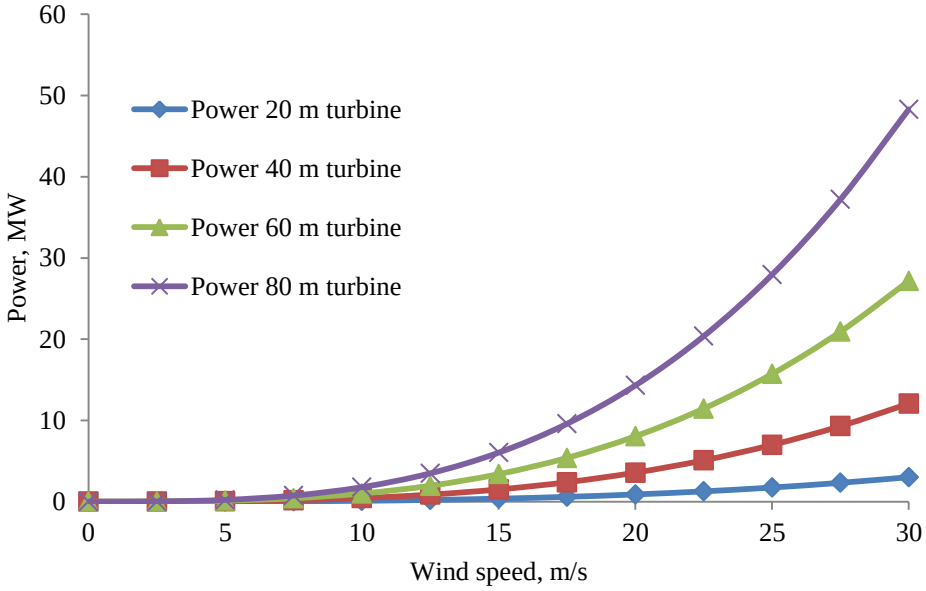

Figure 1.19: Maximum power from commercial turbines with Betz Limit

1.8 Commercial Horizontal Axis Wind Turbine (HAWT)

Horizontal axis wind turbines are the most common type of wind turbine employed commercially. The turbines axis of rotation is parallel to the direction of free stream air flow. Horizontal axis wind turbines work on the fundamental principle of lift. A commercial HAWT turbine is shown in Figure 1.20. The turbines axis of rotation is parallel to the direction of free stream air flow hence it is called a HAWT. It has an efficiency of nearly 48%, compared to latest photo voltaic (PV) cells which have efficiency around 24% (Hau, 2005).

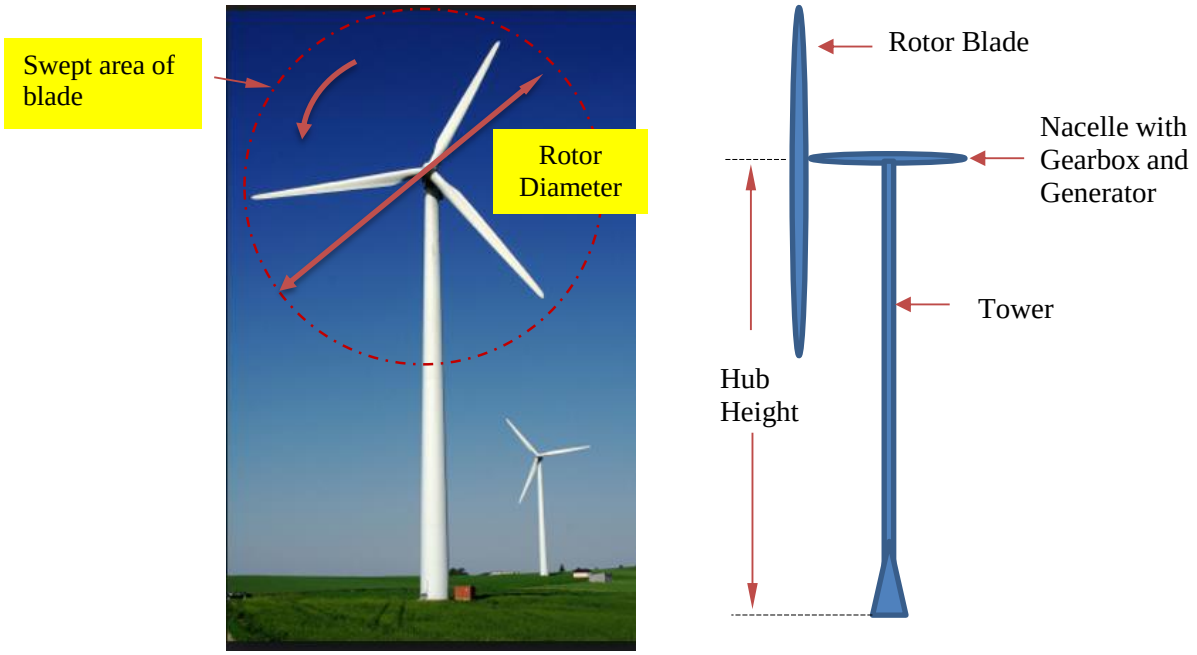

Figure 1.20: Commercial horizontal axis wind turbine (HAWT) (adapted from Open Source Ecology, 2016)

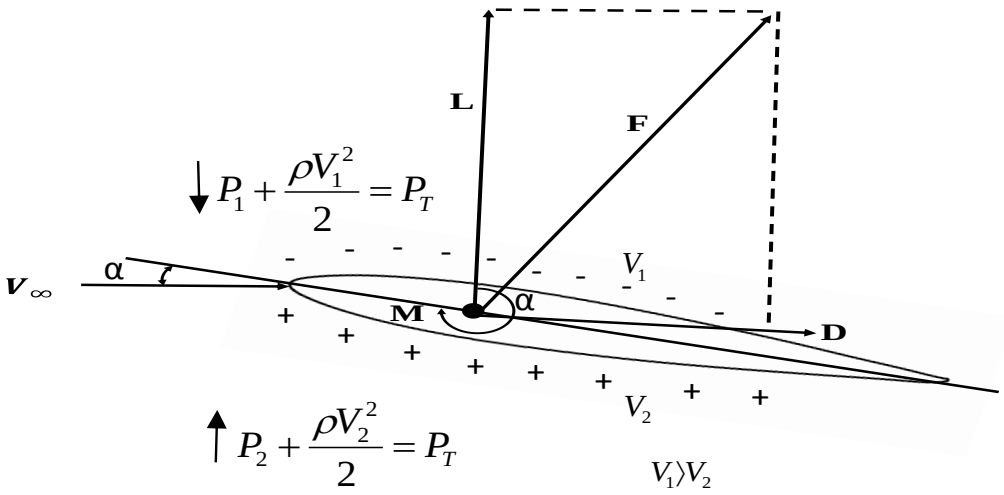

Figure 1.21: Horizontal axis wind turbine (HAWT) (adapted from Open Source Ecology, 2016)

Wind turbine aerofoil blades utilises lift to produce torque which then induces a rotational motion. The geometric shape and cross section of wind turbine blades are defined by the distribution of aerofoils radially. At each blade segment, an aerofoil is stationed with the respect to its chord length. This defines the cross sectional shape of the blades. The aerodynamic forces and moments generated are primarily due to pressure distribution and shear stress distribution. The pressure distribution acts normal or perpendicular to the surface and the shear stress distribution acts tangential to the surface. The pressure variation is mainly due to the changes experienced in air velocity. This can be explained using Bernoulli's principle, which states that the sum of static and dynamic pressure is total pressure. This is expressed as:

$$P_T = P_s + \frac{1}{2}\rho V^2 \tag{1.1}$$

Where P_T is total pressure, P_s is the static pressure, ρ is the density of the air and V is the local velocity along the aerofoil surface.

The pressure force exerted above and below the surface varies with changing angle of attack. The pressure differential produces a net force and moment on the aerofoil as shown in Figure 1.21. The net force generated is comprised of two components, lift and drag. Lift is the force component of the net force exerted on the aerofoil which acts perpendicular or normal to the flow direction. Drag, however is the force that resists the motion of an object and that is parallel to the direction of the flow. The magnitude of this force largely depends on the projected area of an object moving through a fluid and velocity. The lift and drag forces are expressed as:

$$F_L = C_L \frac{1}{2} \rho V^2 A \tag{1.2}$$

$$F_D = C_D \frac{1}{2} \rho V^2 A \tag{1.3}$$

Where ρ is the density of the fluid, A is the projected area and V is the free stream velocity. The variables of C_D and C_L are a non-dimensional terms that both relate to the characteristics of lift and drag. Both of these terms are dependent on speed and angle of attack. As the angle of attack increases, the lift force increase and consequently drag also increases. The drag force is made up of pressure difference of a body immersed in a fluid and frictional drag, which is a function of viscosity, which has a significant contribution to the overall drag acting on a solid body. The power output from turbine can be calculated using the equation 1.4.

$$P_{Turbine} = C_p \frac{1}{2} \rho A V^3 \tag{1.4}$$

1.9 Commercial Vertical Axis Wind Turbine (VAWT)

One notable difference of the vertical axis wind turbine (VAWT) from horizontal axis wind turbine (HAWT) is that the axis of rotation is perpendicular to the direction of the free stream air flow. There are two major types of VAWT: Darrieus and Savonius type. Darrieus turbines operate primarily on the principle of lift and are used in large commercial wind farms as shown in Figure 1.22. The other advantages of Darrius turbines are that the generator and gear box are located at ground level allowing for ease of service and maintenance.

However, it is not as efficient as a horizontal axis wind turbine as shown in Figure 1.20. Furthermore, it needs starting torque to spin. The schematic of the turbine is shown in Section 1.11.2.

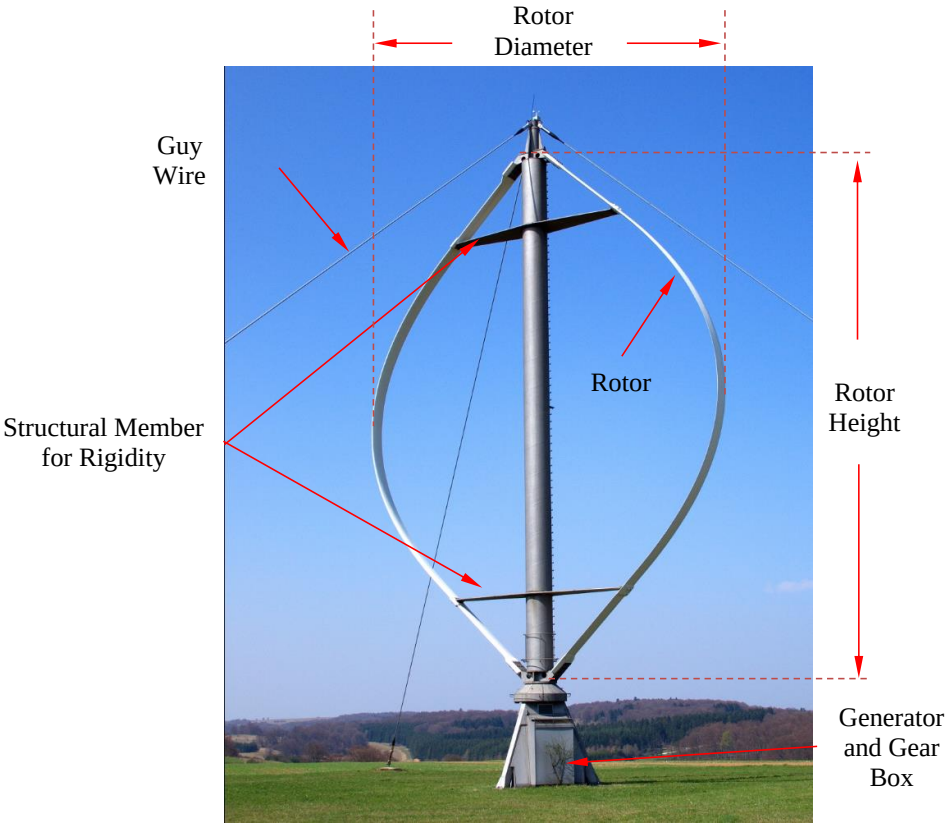

Figure 1.22: Darrieus turbine near Heroldstatt in Germany (adapted from Wacker, 2010)

1.10 Betz's Momentum Theory

The Betz limit states that it is only theoretically possible to convert a maximum of 59.3% of the kinetic energy in the wind to mechanical energy using a wind turbine, and that this maximum power output occurs when the downstream wind has 1/3 the speed of the upstream wind.

The kinetic energy (E) of an air mass (m) moving at a velocity (V) can be expressed as:

$$E = \frac{1}{2} mV^2 \tag{1.5}$$

Air moving through a cross sectional area, (A) (swept by the blades) as shown in Figure 1.20, the volume flow rate of the flow is:

$$Q = VA \tag{1.6}$$

and the mass flow rate with the air density ρ is:

$$\dot{m} = \rho Q = \rho AV \tag{1.7}$$

The equations expressing the kinetic energy of the moving air and the mass flow yield the amount of energy passing through cross-section A per unit time or power P in (W):

$$P_{Wind} = \frac{1}{2} \rho AV^3 \tag{1.8}$$

As mechanical energy is extracted from the kinetic energy contained in the wind stream, with an unchanged mass flow (conservation of mass flow rate), the flow velocity behind the wind turbine blades must decrease. Here, V_1 is the undelayed free-stream velocity, the wind velocity before it reaches the turbine blades, whereas V_2 is the flow velocity behind the turbine blades as shown in Figure 1.23. Neglecting any losses, the mechanical energy, which

the disk-shaped turbine blades extracts from the air flow, corresponds to the power difference of the air stream before and after the turbine:

$$\Delta P = \frac{\rho A V_1^{\,3} - \rho A V_2^{\,3}}{2} \tag{1.9}$$

Maintaining conservation of mass flow (continuity equation) requires that:

$$\rho V_1 A_1 = \rho V_2 A_2 \tag{1.10}$$

Substituting these values in Equation 1.9, we get:

$$P_{Turbine} = \frac{\dot{m}_1 V_1^{\,2} - \dot{m}_2 V_2^{\,2}}{2} = \frac{1}{2}\dot{m}\left(V_1^{\,2} - V_2^{\,2}\right) \tag{1.11}$$

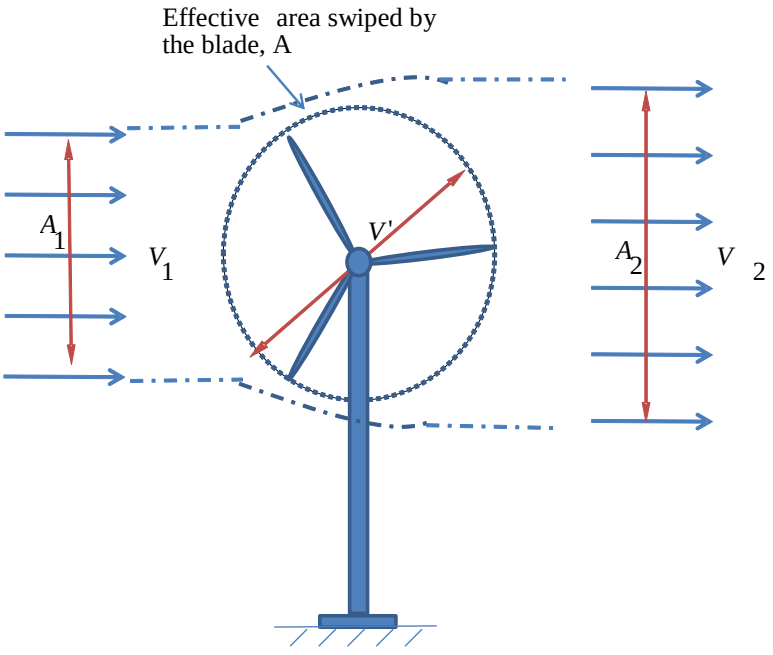

Figure 1.23: Flow conditions due to the extraction of mechanical energy from a free-stream air flow

From this equation, power would have to be at its maximum when V_2 is zero, when the air is brought to a complete standstill by the turbine blades. However, this is scientifically

impossible. If the out flow velocity V_2 behind the turbine is zero, then the inflow velocity before the turbine must also become zero, implying that there would be no more flow through the turbine at all. A physically meaningful result consists in a certain numerical ratio of V_2/V_1 where the extractable power reaches its maximum. This requires another equation expressing the mechanical power of the turbine. Using the law of conservation of momentum, the force which the air exerts on the turbine can be expressed as:

$$F = \dot{m}(V_1 - V_2) \tag{1.12}$$

This force, the thrust, must be counteracted by an equal force exerted by the turbine blades on the air flow. The thrust pushes the air mass at air velocity V', present in the plane of flow of the turbine blades. The power required for this is:

$$P = FV' = \dot{m}(V_1 - V_2)V' \tag{1.13}$$

Thus, the mechanical power extracted from the air flow can be derived from the energy or power difference before and after the turbine blades. Equating these two expressions yields the relationship for the flow velocity V':

$$\frac{1}{2}\dot{m}\left(V_1^{\,2} - V_2^{\,2}\right) = \dot{m}(V_1 - V_2)V' \tag{1.14}$$

Thus, the flow velocity in the turbine blades plane is equal to the arithmetic mean of $V_1$and V_2.

$$V' = \frac{V_1 + V_2}{2} \tag{1.15}$$

The mass flow thus becomes:

$$\dot{m} = \rho A V' = \frac{1}{2}\rho A(V_1 + V_2) \tag{1.16}$$

The mechanical power output of the wind turbine can be expressed as:

$$P_{Turbine} = \frac{\rho A\left(V_1^2 - V_2^2\right)\left(V_1 + V_2\right)}{4} \tag{1.17}$$

In order to provide a reference for this power output, it is compared with the power of the free-air stream which flows through the same cross-sectional area (A), without mechanical power being extracted from it. This power was:

$$P_{Wind} = \frac{\rho A(V_1^3)}{2} \tag{1.18}$$

The ratio between the mechanical power extracted by the turbine blades and that of the undisturbed air stream is called the "power coefficient" Cp:

$$C_P = \frac{P_{Turbine}}{P_{Wind}} = \frac{\frac{\rho A(V_1^2 - V_2^2)(V_1 + V_2)}{4}}{\frac{\rho A(V_1^3)}{2}} \tag{1.19}$$

The power coefficient can be expressed as a function of the velocity ratioV_2/V_1:

$$C_P = \frac{P_{Turbine}}{P_{Wind}} = \frac{1}{2}\left[1 - \left(\frac{V_2}{V_1}\right)^2\right]\left[1 + \left(\frac{V_2}{V_1}\right)\right] \tag{1.20}$$

The power coefficient, i.e., the ratio of the extractable mechanical power to the power contained in the air stream, therefore, now only depends on the ratio of the air velocities before and after the turbine blades. If this interrelationship is differentiated to get the maximum value of the power coefficient it can be obtained that the power coefficient reaches a maximum at a certain velocity ratio with V_2/V_1 =1/3. The maximum power coefficient (Cp_{max}) becomes

$$C_{p(\max)} = \frac{16}{27} = 0.593 \tag{1.21}$$

It is known a Betz Limit as German Scientist Betz is the first to introduce this concept. Knowing that the maximum, ideal power coefficient is reached at V_2/V_1 =1/3, the flow velocity V_1 in the rotor plane thus becomes:

At Betz's limit,

$$V^1 = \frac{2}{3}V_1 \tag{1.22}$$

Hence, the effective wind velocity that is used by the turbine blades is the maximum of 2/3 distance of the incoming free stream velocity.

The power coefficient Cp, ratio of the aerodynamic power of the turbine as a function of the speed ratio λ is given in Figure 1.24. The power coefficient is linked to the efficiency of a wind machine. The curves in Figure 1.24 show that the fast running horizontal axis wind machines (two- or three-bladed airscrew) have the best efficiencies. The Savonius turbine, which is a slow-running vertical axis wind machine, $\lambda \approx 1.0$ has a rather poor efficiency: $C_p \approx 0.13$ to 0.2 at best. Nevertheless, it can present some advantages for specific applications, in particular due its simplicity, robustness and low cost.

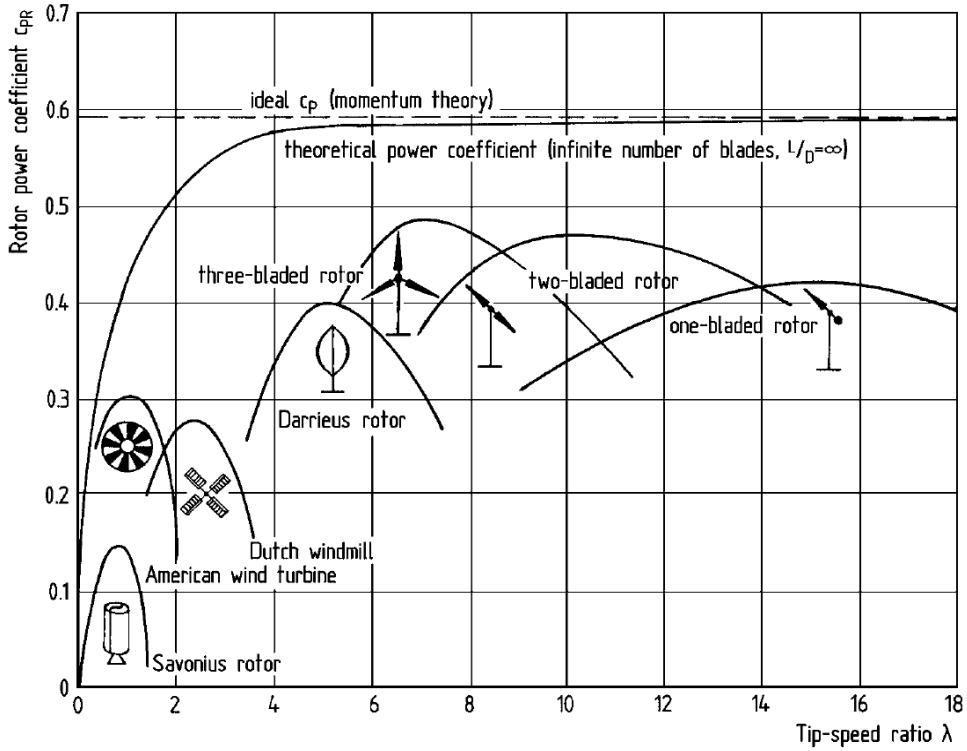

Figure 1.24: Power coefficient of different wind turbine design configuration (from Hau, 2005)

1.10.1 Betz Theorem Relevant To VAWT

The aerodynamics behaviour of a simple drag based vertical axis wind turbine is shown in Figure 1.25.

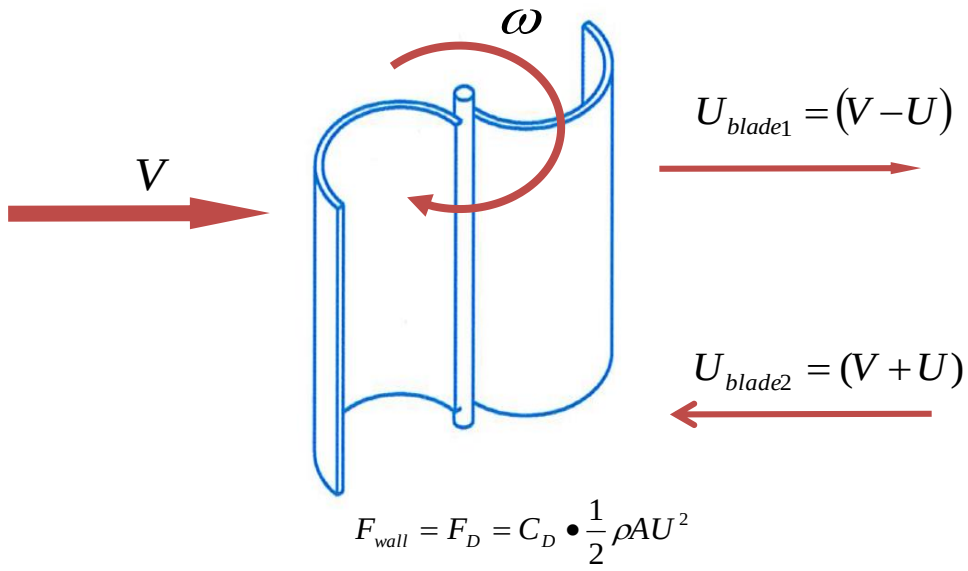

Figure 1.25: Flow conditions and drag force for vertical axis turbines

For a drag based turbine, the power P captured by the drag surface is

$$P_{Turbine} = F_D \times U \tag{1.23}$$

The relative speed V = V – U, which impacts the drag area:

$$F_D = \frac{1}{2}\rho A\left[c_{d1}(V-U)^2\right] - \left[c_{d2}(V+U)^2\right] \tag{1.24}$$

The power thus

$$P_{Turbine} = \frac{1}{2}\rho AU\left[c_{d1}(V-U)^2\right] - \left[c_{d2}(V+U)^2\right] \tag{1.25}$$

$$C_P = \frac{P_{Turbine}}{P_{Wind}} = \frac{\frac{1}{2}\rho AU\left[c_{d1}(V-U)^2\right] - \left[c_{d2}(V+U)^2\right]}{\frac{1}{2}\rho V^3 A} \tag{1.26}$$

Knowing that the maximum power coefficient C_P is theoretically reached at U/V = 1/3 as described in Section 1.10, the maximum value then amounts to

$$C_{p\,max} = \frac{4}{27} C_D \tag{1.27}$$

The maximum net aerodynamic drag coefficient of a concave and convex surface is about 1.2. Thus the maximum power coefficient of pure drag turbine becomes, $Cp\,max \approx 0.2$.

It should be noted that the maximum power coefficient of a pure drag wind turbine is only one third of the C_p value of 0.593 (Betz limit).

1.11 Domestic Scale or Micro Wind Turbines

In this section, examples of domestic scale wind turbines currently available in the market are shown. Domestic scale or small wind turbine is defined as a size that would suit the needs of a domestic residential dwelling of small business. Micro wind turbine is classified as turbine that produces power less than 1 kW. A small turbine is classified as turbine that produces power in-between 1-10 kW (Enhar, 2010).

1.11.1 Micro Horizontal Axis Wind Turbine

A domestic scale micro horizontal axis wind turbine installed on the rooftop in build-up areas of Melbourne metropolitan is shown in Figure 1.26. It is a lift based turbine.

Figure 1.26: Domestic scale horizontal axis wind turbine

Horizontal axis wind turbines possess relatively higher efficiency ($\approx$30%) however it needs to be installed on a tower. Furthermore, HAWTs are inefficient in urban and built-up arrears due to complex urban wind conditions. Detailed explanations on urban wind conditions are given in Section 1.12. HAWTs are also aesthetically unpleasing and undesirable in built-up areas.

1.11.2 Micro Vertical Axis Wind Turbine

A domestic micro vertical axis wind turbine shown in Figure 1.27 is a Maglev type VAWT. It uses drag and lift to produce power.

Figure 1.27: Domestic maglev vertical axis wind turbine

One of the major advantages of vertical axis wind turbines is that they do not need yawing mechanism. Furthermore, VAWTs are capable of operating during minimal wind speed (typically encountered in urban areas) less than 5 m/s. Another advantage is that it does not require a tower to install. They are also more aesthetically pleasing. A schematic of a lift based VAWT is shown in Figure 1.28.

A H-type vertical axis wind turbine typically has two or three aerofoil shape blades. The blades are connected to the turbine shaft at the mid segment. This type of turbine works on lift force. The schematic is shown in Figure 1.28 (a). Here, C is the chord length, L is the blade length, R is the effective radius of the turbine and ω is the angular velocity. Three lift forces acting on the three blades generate a torque about the turbine shaft that rotates the turbine. The schematic of forces acting on the blade are shown in Figure 1.28 (b) where V_∞ is the free stream wind velocity, V_R is relative velocity of blade, R is the effective radius of the turbine.

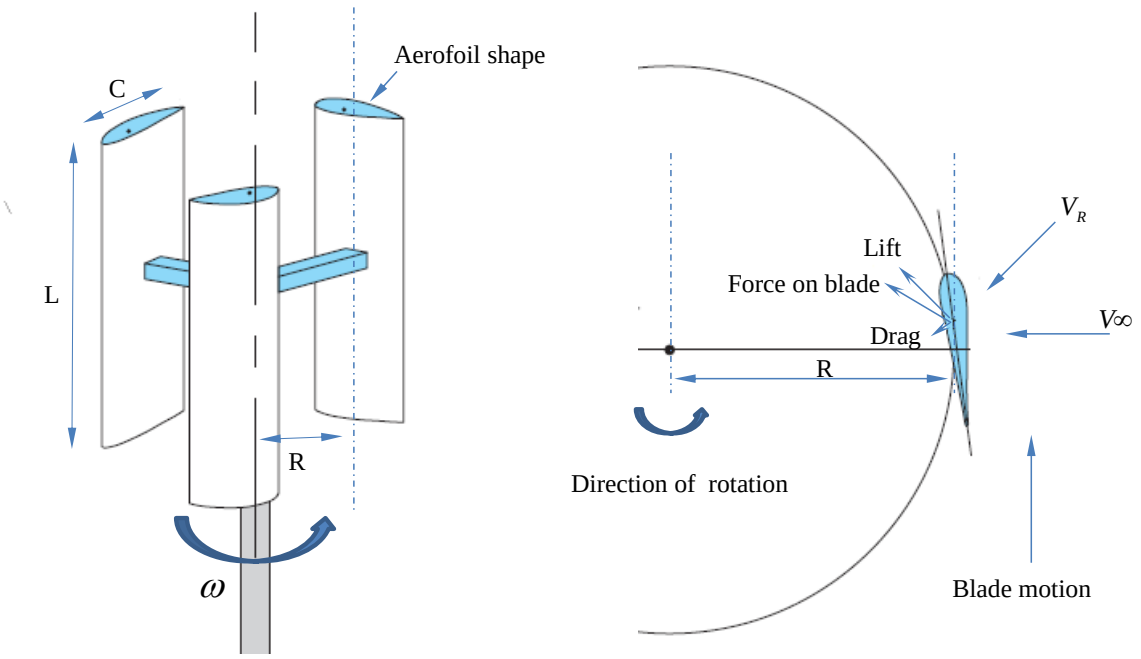

Figure 1.28: (a) Parameters of h-turbine type vertical axis wind turbine; (b) Free body diagram of blade section (adapted from Ahmed, 2013)

A simple drag-based multi-blades vertical axis wind turbine installed on residential rooftop is shown in Figure 1.29.

Figure 1.29: A typical domestic drag based vertical axis wind turbine

A simple drag-based two blades (consists of two half cylinders -concave and convex) vertical axis wind turbine is shown in Figure 1.30. Torque is generated by the difference in net drag

force between the concave ($D_2 = C_{D2} \times \frac{\rho V^2}{2} \times A$) and convex ($D_1 = C_{D1} \times \frac{\rho V^2}{2} \times A$) surface of the two blades times the distance (d). The aerodynamic drag coefficient (CD) for the concave surface is two times higher than the convex surface, Hoerner (1965). Taking moment at point A, $M = (D_2 \cdot d - D_1 \cdot d)$ the difference in drag force on the concave and convex surfaces of the turbine produces a net torque which rotates the turbine. The schematics of a simple drag-based turbine are shown in Figure 1.30 (a), where V is free stream wind velocity.

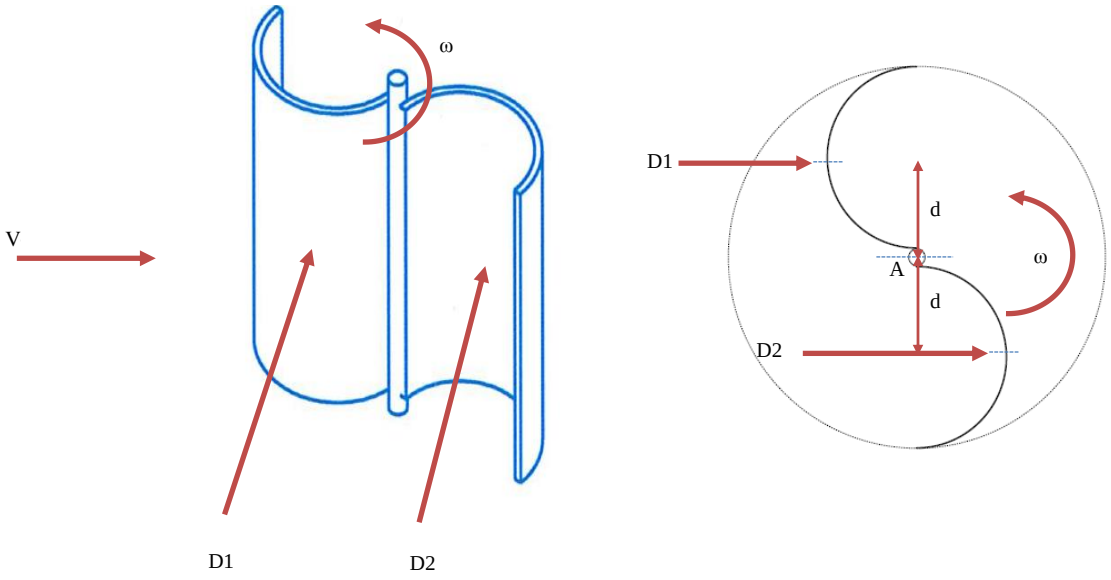

a) Side view b) Top view

Figure 1.30: (a) A Simple drag-based vertical axis wind turbine; (b) Free body diagram of blade section

Although VAWTs are not as efficient as HAWT, they are increasingly popular in urban residential areas. This is largely due to the fact that a VAWT possesses fewer moving parts and operates at a low tip speed ratio which makes it significantly quieter and thus well suited for urban residential areas, Eriksson et al. (2008). HAWTs require a yaw mechanism to redirect itself in the direction of the wind, whereas VAWTs are less sensitive to the changing wind direction and turbulence. Another advantage associated with VAWTs is the simplicity in design. Unlike HAWTs, the gearbox and generator is located at ground level which significantly reduces the complexity of the design and is also relatively easy to maintain and thus lowering the maintenance cost.

1.12 Wind Power Generation in Urban Environment

Urban wind conditions are complex and difficult to predict accurately. Most studies reported in the literature are based on either computational fluid dynamics modelling or low turbulence wind tunnel experimentation, Danao et al. (2014) and Lovett et al. (2016). The average turbulence intensity close to ground proximity (1.7 m above the ground) is over 2%, Blocken and Persoon (2009) and Mendis et al. (2007). However, this intensity is much higher in built-up areas. Therefore the efficiency obtained for a particular drag-based vertical axis wind turbine is based on computational modelling or low turbulence wind tunnel environment which does not correlate well with the in-situ efficiency, Loganathan et al. (2015)

A typical atmospheric boundary layers and wind conditions in rural and urban areas are shown in Figure 1.31. The wind conditions close the ground proximity (in urban boundary layer) in built-up areas vary notably with the structures' height, shape and location, Ikegaya et al. (2016) and Lubitz (2014). Due to complex nature of wind conditions in built-up areas, it is challenging to use HAWT and lift-based VAWT to harness the wind energy to generate power, Alam and Golde (2013) and Webb (2007). Among all available technologies, drag-based vertical axis wind turbine offers better suitability for harnessing wind energy for power generation in built-up areas, Ahmed (2013).

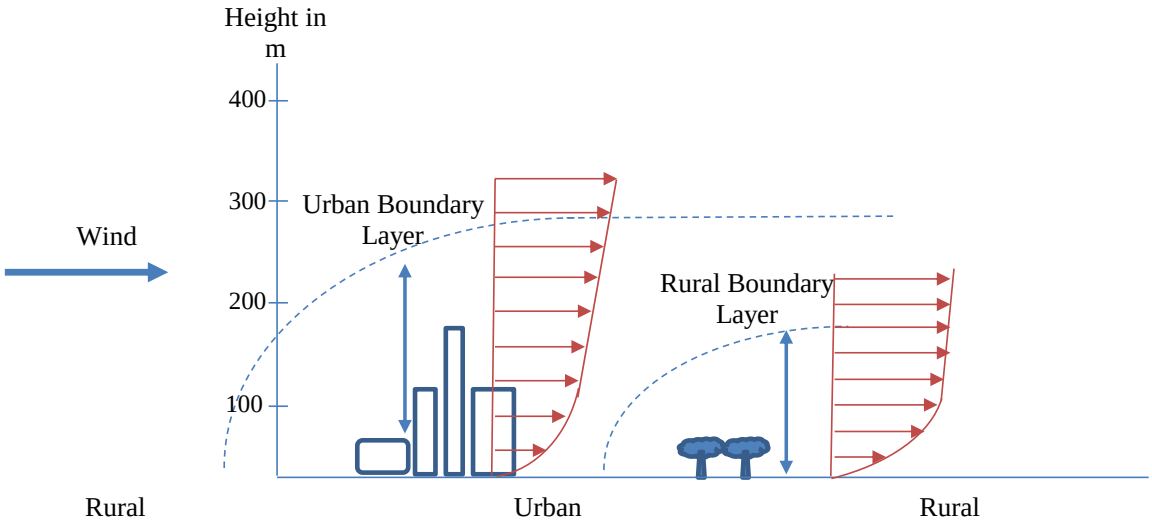

Figure 1.31: Urban and rural atmospheric boundary layer (adapted from Oke, 1976)

Furthermore, wind condition in built-up area remains largely unknown creating hurdles to develop an effective wind power extraction strategy. Currently available wind data using various modelling tools including the CSIRO and US National Renewable Energy Laboratory (NREL) wind mapping tools provides limited insight into the urban micro wind environments. For example, the CSIRO mapping tool incorporates wind characteristics at 65 m above ground level to a resolution of 3 km, Webb (2007). The micro wind environment (due to large resolution, e.g. 3 km) and effects of local landscape features (small hills, ridges, buildings, trees, structures, etc.) cannot be modelled with sufficient accuracy. Data obtained by other modelling tools are also impractical as they incorporate partial micro wind environment over the height of 10 m in urban areas where most roof heights are below 10 m.

1.13 Power Generation by Small Scale Drag Based VAWT

Small scale wind turbines in Australia are defined as turbines that are able to generate 1–10 kW of power. However, some small-scale systems may include turbines of up to 100 kW (Webb, 2007). Micro-wind generators are turbines that generate less than 1kW and are typically used for small battery charging.

1.13.1 Effect of Internal Overlaps

Overlap ratio is defined as ($OR = \frac{e'-e}{d}$) where e' is the shaft diameter, e is the gap between the two subsequent blades and d is the blade diameter as shown in Figure 1.32. This parameter is important in improving the performance of a Savonius turbine and thus numerous studies have been conducted to optimise this parameter. Overlap ratios found in literature reviews can be classified as Internal and External Overlap ratios.

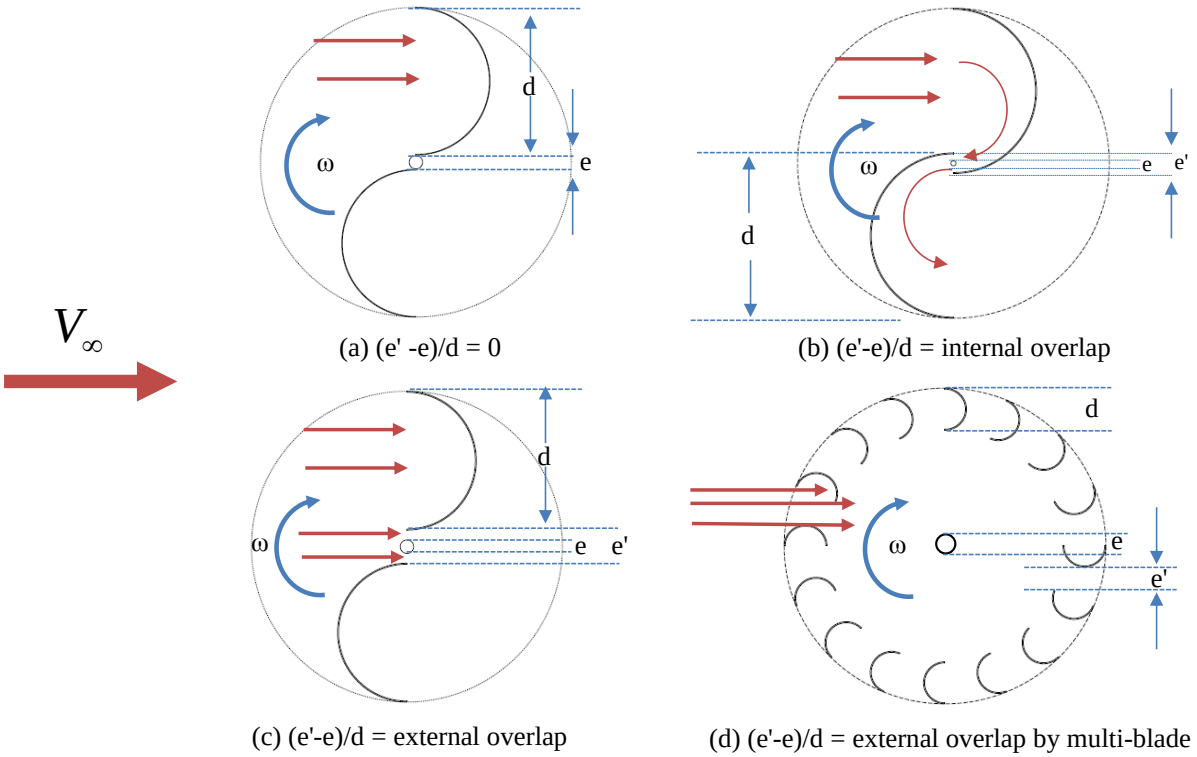

Figure 1.32: Vertical axis wind turbine with zero, internal and overlap ratios

1.13.2 Effect of Aspect Ratio

Aspect ratio, AR = H/D, is defined as the ratio of the height, H of the turbine and diameter, D of the turbine as shown in Figure 1.33.

Alexander and Holownia (1978) carried out experimental wind tunnel studies on the effect of aspect ratio on a Savonius turbine. Two turbines with 0.19 m and 0.38 m chord with aspect

ratios of 1.2, 2.4, 3.6 and 4.8 were tested. They kept the overlap ratio at zero. Their investigations were aimed at finding the effect of variables blade aspect ratio in increasing the efficiency of a single stage Savonius turbine in wind speeds of 6 m/s to 9 m/s. Their study indicated a possibility of increasing the efficiency from 6.5% to 24.3% by manufacturing a turbine with an aspect ratio (height divided by the radius) of 4.8. However, their study did not attempt to find an optimum blade configuration. Furthermore, the results are inconclusive and have not been independently verified by other authors.

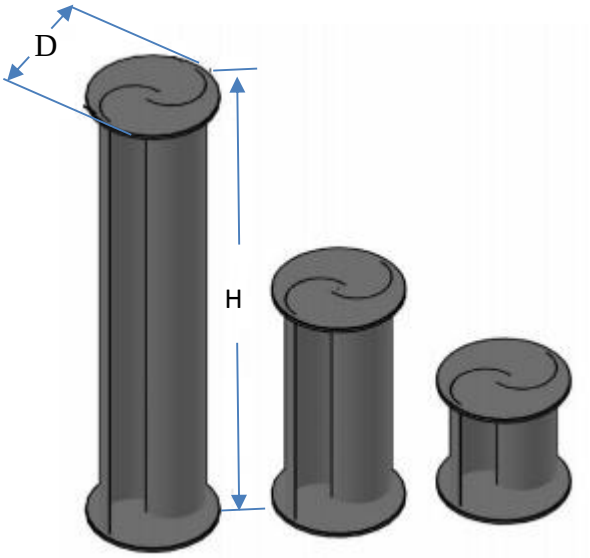

Figure 1.33: Vertical axis wind turbine with different aspect ratios (adapted from Kamoji et al. 2009)

Kamoji et al. (2009) investigated relationship between the aspect ratio and efficiency of a VAWT. They tested different configurations for aspect ratios of 0.6, 0.7, 0.77, and 1 by keeping other parameters constant. Their study found the maximum Cp for a turbine was at aspect ratio of 0.7. However, Kamoji and his colleagues did not investigate the effect of overlap ratio. Their investigation was limited to two blades and overlap ratio of 0.2.

1.13.3 Effect of Blade Number

Blackwell et al. (1977) carried out experimental investigation on the effect of blade number on a vertical axis wind turbine (VAWT) with zero overlap ratios. Their investigation was aimed at examining the effect of blade number on the efficiency of the VAWT. The study

showed that the number of blades has a significant influence on the efficiency (Cp). The maximum Cp of a two-bladed turbine increased by approximately 50% compared with that of a three-bladed turbine. The three-bladed turbine did not exhibit negative torque at any angular position, and the static torque variation was less than that in the two-blade turbine. However, Blackwell and his colleagues did not consider the effect of higher blade number without overlap typically found on multi-blade VAWT.

Mahmoud et al. (2012) investigated and tested two, three and four-bladed turbines with aspect ratios and varying number of stages but with the same overlap ratio of zero. The two-bladed turbine in single and double stages, with different aspect ratios, performed better than the three- and four-bladed turbines. Similar to Blackwell and his colleagues, this study did not to consider the effect of higher blade number without overlap typically found on multi-blade VAWT.

Saha et al. (2008) carried out wind tunnel tests to assess the aerodynamic performance of single, two and three-stage Savonius turbine systems. Experiments were carried out to optimize the different parameters like the number of stages, blade number (two and three) and geometry of the blade (semicircular and twisted). Their investigation revealed that most efficient configuration is the two bladed Savonius turbine with twisted geometry blade and overlap ratio of 0.2. However, this study failed to consider the effect of higher blade number without overlap typically found on multi-blade VAWT. Furthermore, adding twist increases complexity.

Ali (2013) conducted an experimental comparative study of two and three blades Savonius turbines. His investigation was aimed at examining the effect of blade number on the efficiency of a Savonius turbine. The two-bladed turbine improved Cp by approximately 25.5% when compared to the three-bladed turbine. The torque coefficient of the two-bladed turbine was also superior to that of the three-bladed turbine because the latter experienced more drag effect than the former. However, this study did not incorporate the effect of higher blade number without overlap, typically found on multi-blade VAWT.

1.13.4 Effect of Overlap Ratio

Fujisawa and Gotoh (1992) carried out experimental wind tunnel studies on the effect of gap between two cylindrical halves of a Savonius turbine. Their investigations were aimed at identifying the optimum overlap ratio. They reported that the flow rate increases with the increase in overlap ratio and the wake region produced by blockage decreases with the increase in flow rate. The effect increases the pressure force on the concave side of the returning blade. The optimum overlap was determined to be 0.15. However, the study did not reveal detailed correlation between the blade number, the turbine blade diameter and the turbine diameter.

Jian et al. (2012) investigated the influence of overlap ratio, phase-shift and stage on a Savonius turbine. They found that the single-stage, double-bladed turbine exhibited an optimum overlap ratio of 0.166. By contrast, the double-stage turbine with a phase shift angle of 0° exhibited maximum Cp at an overlap ratio of 0.333. The results show that appropriate choice of the phase-shift angle according to the overlap ratio can not only increase the power coefficient of the Savonius turbines but also eliminate the negative static torque and smooth the variation of the static torque coefficient. Moreover, the performance of the two-stage turbines indicates that the two stage turbine is a better candidate for this type of wind turbines.

1.13.5 Effect of Blade Shape

Roy and Saha (2015) studied the performances and compared the torques of the conventional Savonius turbine, a semi-elliptical turbine, the Benesh turbine, the Bach turbine, and a newly developed two-bladed Savonius turbine. The designs are shown in Figure 1.34. The result of the dynamic performance study with blockage correction showed that the newly developed turbine Figure 1.34 (e) has a maximum Cp of 0.27 at the tip speed ratio of 0.77 when tested at the Reynolds number (Re) of 6.0×10^4. The newly developed turbine was also found to demonstrate higher performance of approximately 28.6%, 17.4%, and 3.8% compared with

the conventional Savonius. However, Roy and Saha's did not study the effect of higher blade number. Modifying the blade shapes added to complexity and cost.

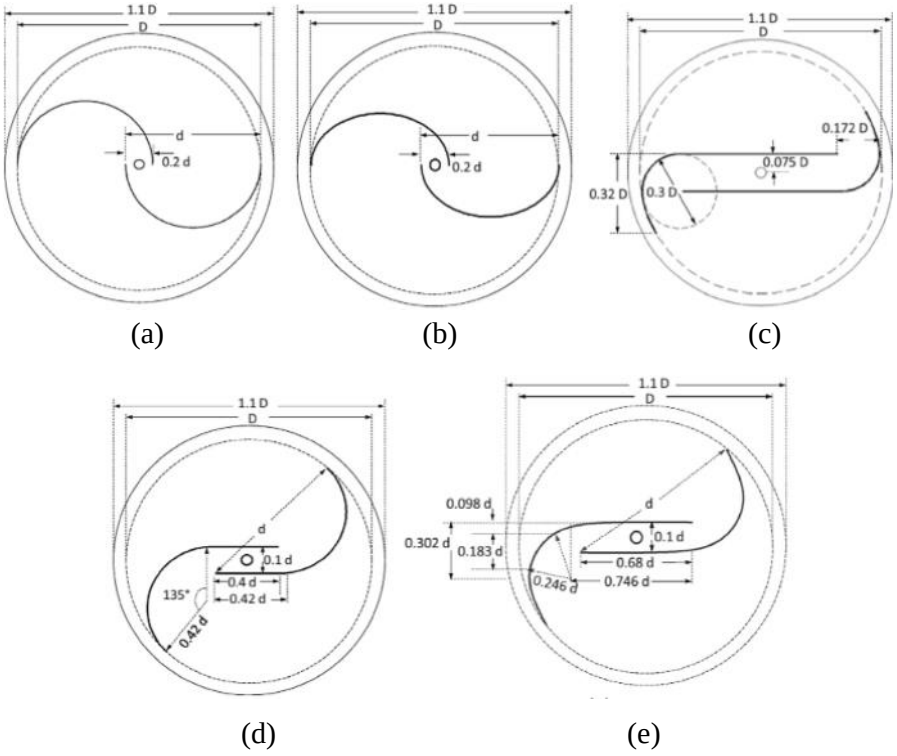

Figure 1.34: Top view of the s-turbines with dimensions: (a) Simple savonius turbine, (b) Semi-elliptical turbine, (c) Benesh turbine, (d) Modified Bach turbine, (e) Newly developed turbine (from Roy and Saha, 2015)

1.13.6 Effect of Twisting

The use of twist in Savonius turbine blades seems to improve efficiency as well as the starting ability. However limited studies have been reported in the literature, Saha and Rajkumar (2006). The performance of the Savonius turbine was found to increase with an increase of the twist angle. It is interesting to note that a larger twist angle was preferred at a lower wind speed to produce higher power and better starting characteristics. A twist angle of 15° gives an optimum performance at low wind speeds of V = 6.5 m/s. Such blades show a power coefficient (C_P) of 13.99% at a tip speed ratio (TSR) of 0.65 (i.e. at V = 8.23 m/s), whereas the semicircular blade with zero twist angle shows a power coefficient (C_P) of 11.04% at a tip speed ratio (TSR) of 1.0. Saha and Rajkumar (2006) also substantiated these findings in their studies with two and three-bladed turbine systems and observed a higher

power coefficient of 0.216 with twist angle of 30° for a two-bladed turbine. However, the study did not attempt to find an optimum blade configuration. Furthermore, twisting increases the cost and manufacturing complexity.

Irabu and Roy (2007) used guide-box tunnel to improve the power output as well as reducing the negative torque of the Savonius turbine. It is a rectangular box with a wind passage for testing the turbine. The maximum turbine rotational speed is obtained for a guide-box area ratio between 0.3 and 0.7. The power coefficient of the turbine with guide-box tunnel using an area ratio of 0.43 increases considerably (by a factor 1.5 using three blades and by a factor 1.23 using two blades) compared to the conventional design without guide-box. The optimum spacing ratio between the turbine tip and the side walls of the guide-box tunnel is around 1.4. However, Irabu and Roy did not consider the effect of yaw angle of the guide box. In urban areas, the wind is highly turbulent and intermittent. Furthermore, the guide-box considerably increases the system complexity.

Altan et al. (2008) introduced a deflector known as a curtain to improve the performance of a Savonius turbine. The curtain arrangement was also optimized. At optimum curtain arrangement, the Cp of a simple Savonius turbine increased to 38% compared with that of a Savonius turbine without a curtain. The curtain arrangement is shown in Figure 1.35. However, the study did not attempt to find an optimum blade configuration.

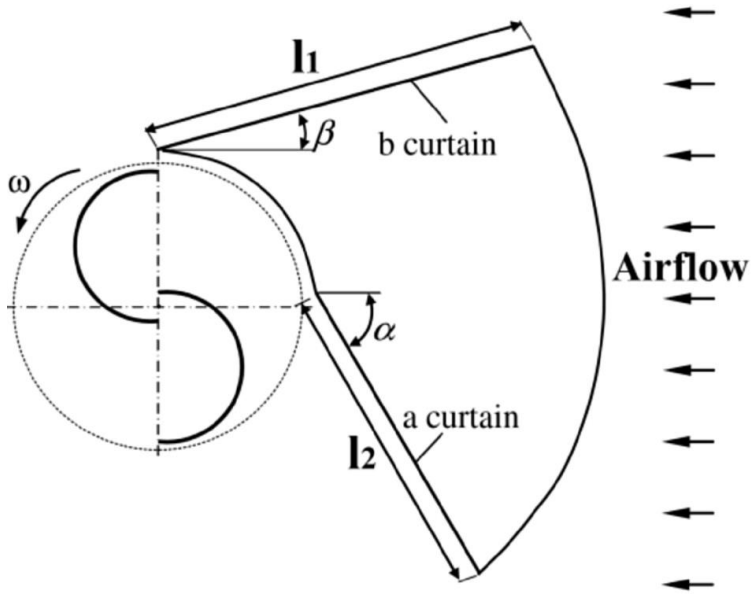

Figure 1.35: Arrangement of savonius turbine with curtain (from Altan, 2008)

Shaughnessy and Probert (1992) and Golecha et al. (2011) carried out experimental wind tunnel studies on the use of deflector plates. The deflecting plates have been used as a power augmenter in two ways, (a) local acceleration of airflow on the turbine surface moving with wind and (b) reduction of wind resistance on the turbine surface moving against the wind. Their investigations were aimed at finding the effect of enhancement in the power output for a single stage turbine. The study indicated a possibility to increase the power output by up to 50%. They also reported the enhancement in the power output was possible by 42%, 31% and 17%, respectively for a two-stage with 0° phase shift, for a two-stage with 90° phase shift and for a three-stage with 60° phase shift. However, the study did not attempt to find an optimum blade configuration.

1.13.7 Effect of Stage Numbers

Hayashi et al. (2005) investigated the effect of stage numbers on the efficiency of VAWT. The study revealed that the Cp of a three-stage turbine with a bucket phase shift of 120° decreased by approximately 25% compared with a single-stage turbine. The peak torque values of the three-stage turbine were also lower than those of the single-stage turbine. Despite this condition, the three-stage turbine exhibited better dynamic characteristics. Similar study by Jian et al. (2012) reported that a multistage turbine exhibited approximately 20% less power than a single-stage turbine. However, increasing the number of stages increases manufacturing complexity.

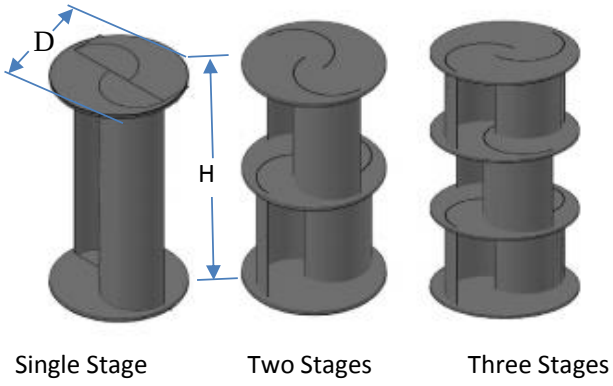

Figure 1.36: Single and multi- stage vertical axis wind turbines (adapted from Hayashi et al. 2005)

1.13.8 Effect of External Overlaps

Yoon et al. (2013) conducted a parametric study on a multi-blade (straight) vertical axis wind turbine as shown in Figure 1.37. They described the experimental results of a vertical axis wind turbine (VAWT) of 205 mm diameter with multiple blades, Yoon et al. installed the turbine in an open-type small-scale wind tunnel with the aim to study the variation of several wind design parameters (i.e., length and angle) on the system performance. The findings showed that the efficiency of this system increases with increasing wind velocities up to approximately 25 m/s, after which the efficiency dropped rapidly. They concluded that performance depends on the blade angle and it has a maximum value at 45°. The study however did not provide the performance curve for the system. Details about the torque, power and power coefficient were also not revealed. Parametric surveys of the wind blade design are still being conducted.

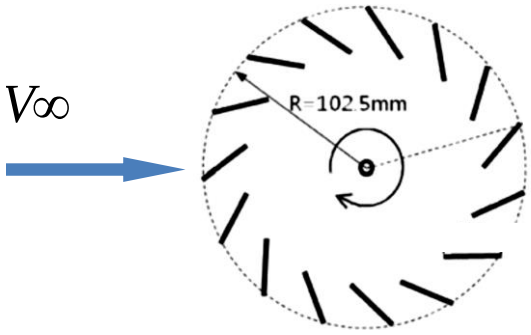

Figure 1.37: Specification of wind turbine with multiple blades (adapted from Yoon, 2013)

Driss et al. (2015) conducted an experimental investigation to study the effect of external overlap ratios on the performance of a two blades vertical axis wind turbine (VAWT). They studied four VAWT prototypes with overlaps of zero, 0.1, 0.2 and 0.3 mm. The overall performance evaluation of the turbine was based on the power and dynamic torque coefficient. The prototype with external overlaps is shown in Figure 1.38.

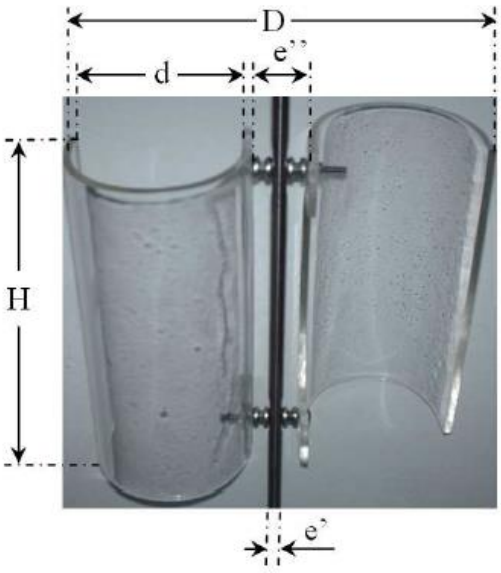

Figure 1.38: Geometrical arrangement with external overlap prototype (from Driss et al. 2015)

The results showed the most efficient configuration is the prototype with zero overlap ratios. They concluded that the performance decreased as the external overlap ratios increased. However, the study did not attempt to find an optimum blade configuration. Furthermore, their results are inconclusive and have not been independently verified by other researchers.

1.14 Vertical Axis Wind Turbine (VAWT) Power: Methods of Evaluation

There are mainly two different approaches used to assess the aerodynamics characteristics of VAWTs:

(a) Experimental techniques using wind tunnel experiment or field testing
(b) Computational methods

1.14.1 Experimental Methods

Experimental techniques consist of wind tunnel testing either with a full-size or a scale model. The wind tunnel provides that approximate flow over an experimental model within a

controlled environment. The accuracy of such controlled environment depends on the extent to which the environment is replicated in the wind tunnel, the geometric accuracy of the model, and the wind speed. In wind tunnel testing, the speed and direction of the flow can be held constant. Hence, the measurements made in a wind tunnel are generally very repeatable.

In a wind tunnel study, air flow is generally visualised using smoke and wool tufts. Fujisawa and Gotoh (1992) used such flow visualisation using wool tufts to understand the flow around a Savonius turbine in the wind tunnel.

Regardless of wind tunnel type, the most important consideration is the level of turbulence and blockage ratio. These two parameters of the wind tunnel must be low enough to provide an acceptable flow pattern with minimum interference. In this study, a close return circuit wind tunnel is used. The wind tunnel has low turbulence level as measured by about 1.8% and the maximum blockage ratio for the full-scale test was less than 10%.

1.14.2 Computational Methods

Computational Fluid Dynamics (CFD) deals with the numerical analysis of fluid flows. CFD utilises the Navier-Stokes equations, which govern the motion of a Newtonian viscous fluid to solve fluid dynamics problems. Numerical solution for the three-dimensional, time-dependent motion of turbulent flow is expensive and requires super computers. CFD is mostly used in research studies in simple configurations at low Reynolds numbers.

CFD can be useful for flow visualisation and in understanding general flow behaviour. Although simplified numerical solutions exist for specific problems related to aerodynamic evaluation, few aerodynamic unsteady wind conditions can be solved analytically or computationally with sufficient accuracy due to strong unsteadiness of motions created by separated, separated and re-attached, and attached flows.

1.15 Conclusion from Prior Work

The studies reviewed here show that vertical axis wind turbines (VAWT) effective use in built-up areas is significantly constrained due to its less than expected *in-situ* performance. Current understanding of VAWT aerodynamics is limited to steady wind performance. Very

few attempts have been made to establish how a VAWT operates in unsteady wind conditions and why.

Currently, most VAWT development is being carried out experimentally as few aerodynamic unsteady wind condition can be solved analytically or computationally with sufficient accuracy due to strong unsteadiness of motions created by separated, separated and re-attached, and attached flows.

Despite some studies have been undertaken to enhance the power output of vertical axis wind turbines by varying the overlap ratios and by using semi-circular and straight blades, no work has been reported in the public domain on a single stage multi-blade drag-based vertical axis wind turbine with semi-circular shaped blades. The literature review clearly indicates that various studies have been conducted to understand the effects of wind on the frontal and rear blades. It is assumed no effect of wind passing through blades (section A-A). However there is a significant knowledge gap and deficiency in the comprehensive understanding of effects of gaps between subsequent blades (c) as shown in Figure 1.39 under a range of wind conditions.

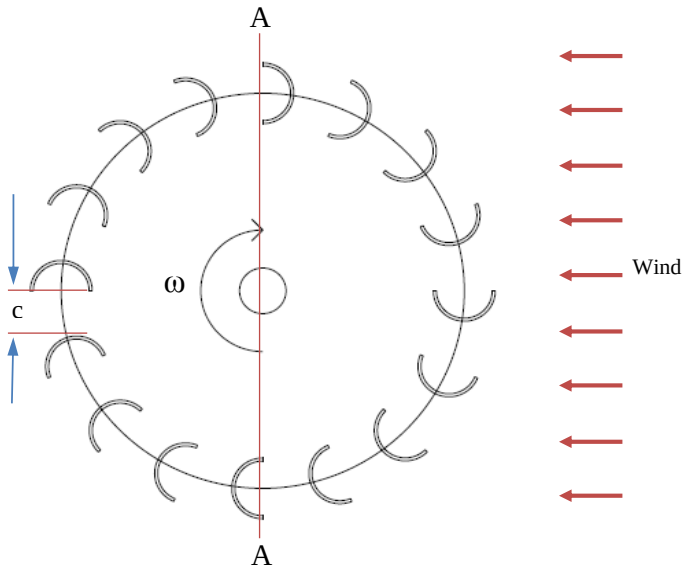

Figure 1.39: Schematic of multi-blade vertical axis wind turbine

Moreover, no information is available about the optimal clearance between two subsequent blades of a multi-blade drag-based vertical axis wind turbines and the effect of blade number and diameter. A summary of current body of knowledge on micro VAWTs is shown in Table 1.2.

Table 1.2: Summary of related published research work

	Methodology	Blade number	Type of blade	External/ Internal overlaps	Shield	Twist	Solidity	Cp
Alexander and Holownia (1978)	Wind tunnel	2,3 and 4	Semi-circle	Internal	No	Yes	No	0.24
Kamoji et al (2009)	Wind tunnel	2	Semi-circle	Internal	No	Yes	No	0.21
Saha and rajkumar (2006)	Wind tunnel	2 and 3	Semi-circle	Internal	Yes	Yes	No	0.14
Irabu and Roy (2007)	Wind tunnel	2 and 3	Semi-circle	Internal	Yes	No	No	0.24
Cheng et al (2012)	CFD	2	Semi-circle	Internal	No	No	No	0.19
Yoon et al (2013)	Wind tunnel	15	Straight	External	No	No	No	No
Driss et al (2015)	Wind tunnel	2	Semi-circle	External	No	No	Yes	0.11

1.16 Objective and Scope of this Work

From examination of the prior work undertaken in this area, one may conclude that there are significant gaps in understanding the performance of a multi-blade vertical axis wind turbine. Therefore the primary objectives are:

- Understand the effect of geometric configuration of turbines, turbine diameter and blade number on VAWT performance
- Understand the effect of blade orientation on VAWT performance
- Investigate the effect of turbulent wind on VAWT performance
- Investigate effect of cowling on VAWT performance

Therefore, the research questions to be answered by this research project are as follows:

- How do the change of number of blades and blade gap affect the torque and power?
- What is the effect of scales (e.g., model scale up) on the torque and power?

- What is the effect of turbulence on a drag-based VAWT on power and torque?

The innovation of this research is to develop a single stage multi-blade drag based-vertical axis wind turbine that can be scaled for various power needs in built-up areas.

1.17 Thesis Layout

The structure of this thesis is as follows:

Chapter 1 (current chapter) outlines the background, reviews the relevant literature, the fundamental theories of aerodynamics related to drag and lift of Horizontal Axis Wind Turbines and Vertical Axis Wind Turbines and describes the aims and scope of this work

Chapter 2 describes the instrumentation and experimental facilities used in this research. A detailed description of RMIT research wind tunnel including the data acquisition system used for aerodynamic force measurements is given together with calibrations details.

Chapter 3 presents the design of wind turbines from an aerodynamic perspective. It describes the aerodynamic design parameters used and outlines the process involved in designing the wind turbine. It also presents the methodology used to design as well as the material of choice for the manufacturing of the turbine blades. It also presents a detailed description of the instrumentation, test equipment, data processing and experimental test setup.

Chapter 4 outlines the results for aerodynamic effects of a multi-blade single stage drag-based vertical axis wind turbine includes following geometric features: turbine radius (R), blade number (N), blade radius (r), and clearance between two subsequent blades (c). Power curves for the optimal blade configurations are also presented in this chapter.

Chapter 5 presents the development of an optimal blade-number prediction model for a single stage multi-blade drag-based vertical axis wind turbine. The industrial implications of the results from this work are also described in this chapter.

Chapter 6 outlines the major conclusion from this work and the suggestions for further studies.

Chapter 7 outlines the suggestions for further studies.

CHAPTER 2

Experimental Facilities and Instrumentation

This section details the experimental procedure and equipment that were utilised to acquire the data in the wind turbine as well as data processing. For reliable results to be obtained, it is important that the experiment is conducted professionally and in an efficient manner with the correct procedures and safety precautions taken into account.

2.1 RMIT Industrial Wind Tunnel

The experimental investigation was carried out in RMIT Wind Tunnel. The tunnel is a closed return circuit with a turntable to yaw a suitable model to the wind direction. It has a rectangular test section with 3 m wide, 2 m high and 9 m long. The cross sectional area of the rectangular test section is 6 m^2. The maximum speed of the tunnel in the test section is approximately 145 km/h. Its turbulence intensity is around 1.8%. The tunnel was calibrated prior conducting the experiment investigation and the mean air speeds at the entry and at the test position in the tunnel were measured with a modified National Physical Laboratory (NPL) ellipsoidal head Pitot-static tube connected through flexible tubing with a Baratron® pressure sensor made by MKS Instruments, USA.

The wind tunnel tests were conducted at a range of wind speeds (4.5 m/s to 8.5 m/s with an increment of 1 m/s) for all prototype models. At each speed, the turbine rotational speed (rpm) and torque (T) were measured. Measurements were taken three times for each configuration at all wind speeds tested. The acquired data was averaged to minimise the error. The minimum wind speed (4.5 m/s) was constrained by the ability of the turbine to overcome the bearing frictional and inertial resistance. The upper limit of wind speed (8.5 m/s) was limited by the structural rigidity and vibration. More details about the wind tunnel can be found in Alam (2000). A schematic plan view of the tunnel is shown in Figure 2.1.

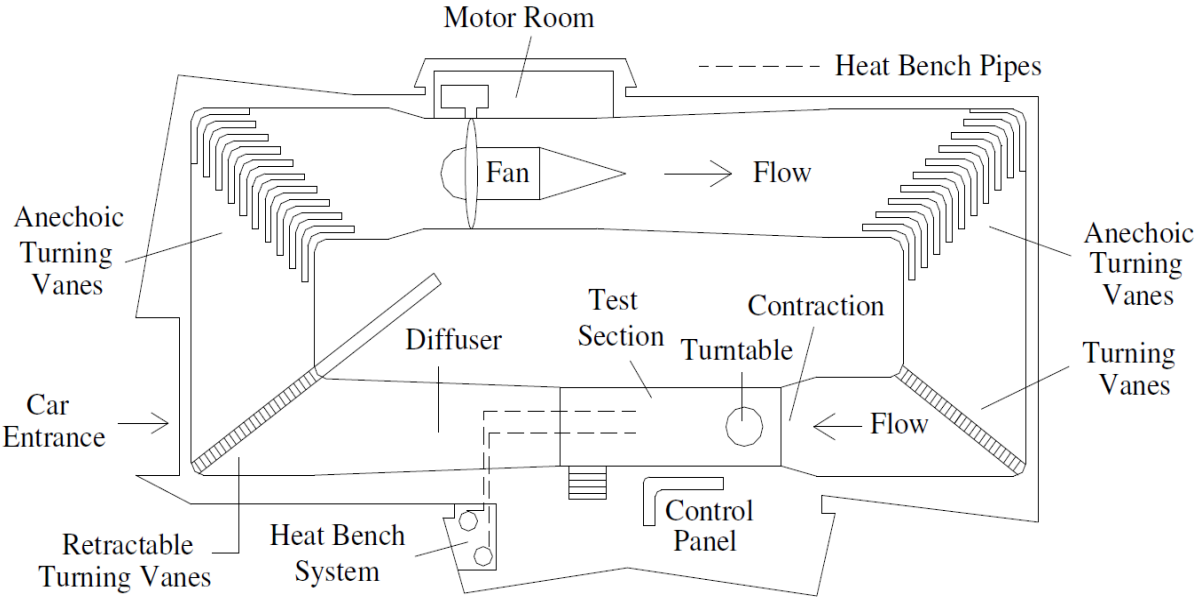

Figure 2.1: A schematic of RMIT industrial wind tunnel (from Alam, 2000)

2.2 Measurements of Dynamic Pressure, Velocity and Temperature

The air speeds inside the wind tunnel were measured with a modified National Physical Laboratory (NPL) ellipsoidal head Pitot-static tube (located at the entry of the test section) which was connected through flexible tubing with the Baratron pressure sensor (MKS Instruments, USA) as shown in Figure 2.2. The pressure readings from the pressure sensor is fed through to the wind tunnel computers which then computes flow properties such as the local flow speed, dynamic pressure and temperature.

Equation 2.1 represents the total pressure, (P_T) components: static pressure (P_S) and Dynamic pressure $\left(P_D = \frac{1}{2}\rho V^2 \right)$ measured by the Pitot-static tube. The wind speed (V) was calculated using equation 2.2.

$$P_{Static} + P_{Dynamic} = P_{Total} \tag{2.1}$$

$$V = \sqrt{\frac{2(P_{Total} - P_{Static})}{\rho}} \quad \text{(m/s)} \tag{2.2}$$

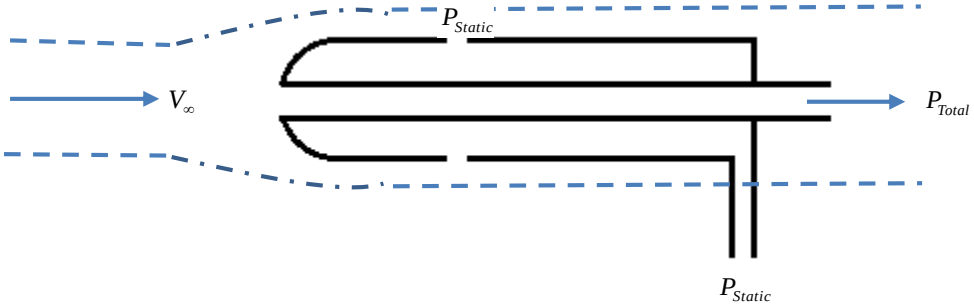

Figure 2.2: A schematic of a pitot-static tube

2.3 Wind Tunnel Calibration

Dynamic pressures (q) in the wind tunnel were measured vertically from 200 to 1800 mm in an increment of 200 mm from the tunnel floor at the location where the experimental arrangements were mounted. The nominal tunnel air speeds were 20, 40, 80 and 120 km/h with less than ±1% accuracy. The local pressure was normalised by dividing by the wind tunnel reference pressure (*qref*) and plotted against the height for the air speeds as shown in Figure 2.3. This indicated that the local pressure did not vary significantly when referenced to the tunnel wall-mounted reference pressure for the given speed. However, a small variation of normalised velocity can be seen near the tunnel floor (Figure 2.3). No correction of velocity was deemed necessary as local pressure (q) did not vary significantly with wall mounted reference pressure (*qref*) with height. The accuracy of the pressure measured with various speeds across the plane was calculated to be less than ±1%. Hence the tunnel reference pressure was used in the calculation of drag and lift coefficients.

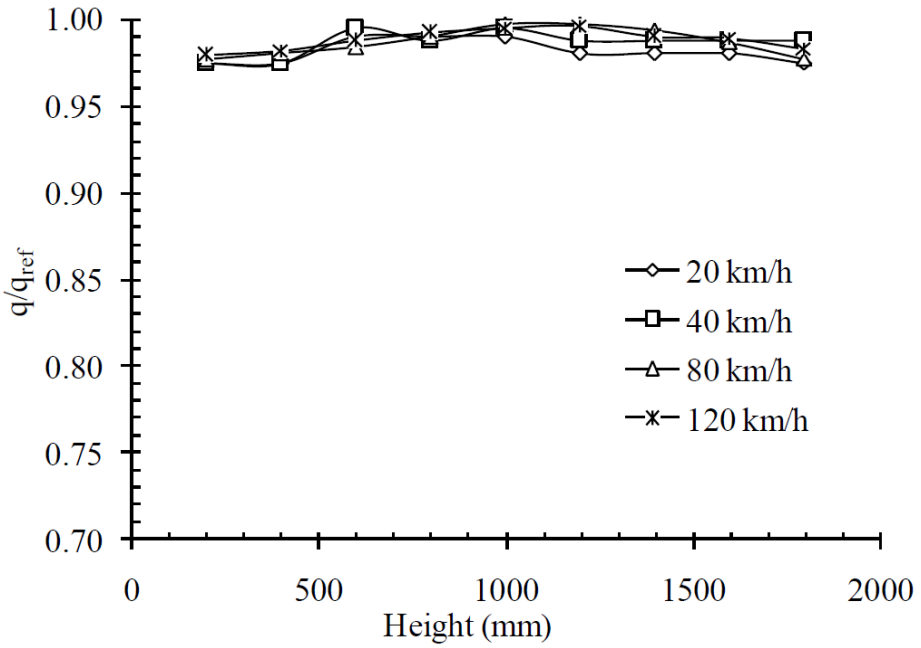

Figure 2.3: Normalised local pressure variation with height in relation to reference pressure (from Chowdhury, 2013)

2.4 Development of Methodology and Device for Measuring the Toque and Power of a Vertical Axis Wind Turbine

2.4.1 Data Collection

Power curves are used by engineers and manufacturers to characterize the performance of a wind turbine as shown in Figure 2.4. Power curves are generated using raw data: torque and rotational speed of the turbine at a given wind speed obtained during testing. Hence, it is essential to develop a scientific testing methodology to test the wind turbines.

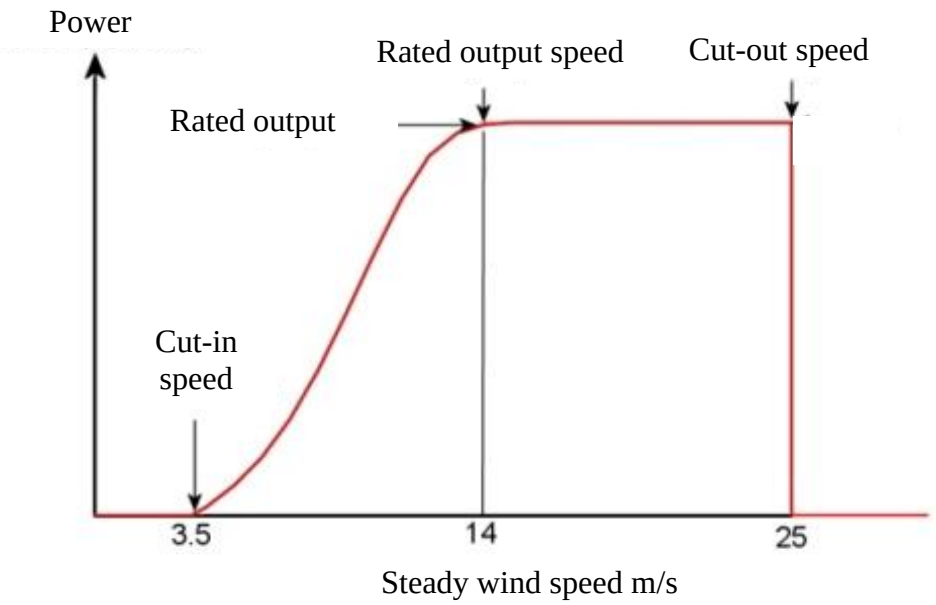

Figure 2.4: Typical wind power output with constant wind speed

As there are no Standard Test Methodology for wind tunnel data acquisition for wind turbine reported in the public domain, it was required to develop data acquisition system for this study.

A data acquisition system should be able to capture the following;

1) Instantaneous mechanical torque generated by the wind turbine
2) Instantaneous rotational speed of the turbine
3) Instantaneous wind speed

As there was no such data acquisition system readily available at RMIT or elsewhere, a data acquisition apparatus was designed and manufactured for this study as shown in Figure 2.5 and Figure 2.6. Details are shown in the Appendix.

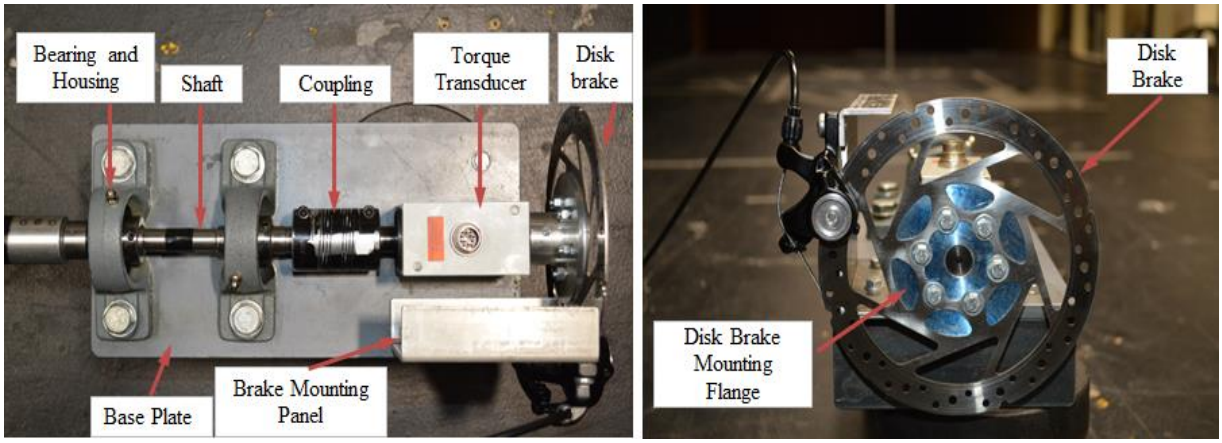

Figure 2.5: HBM torque transducer and disc brake

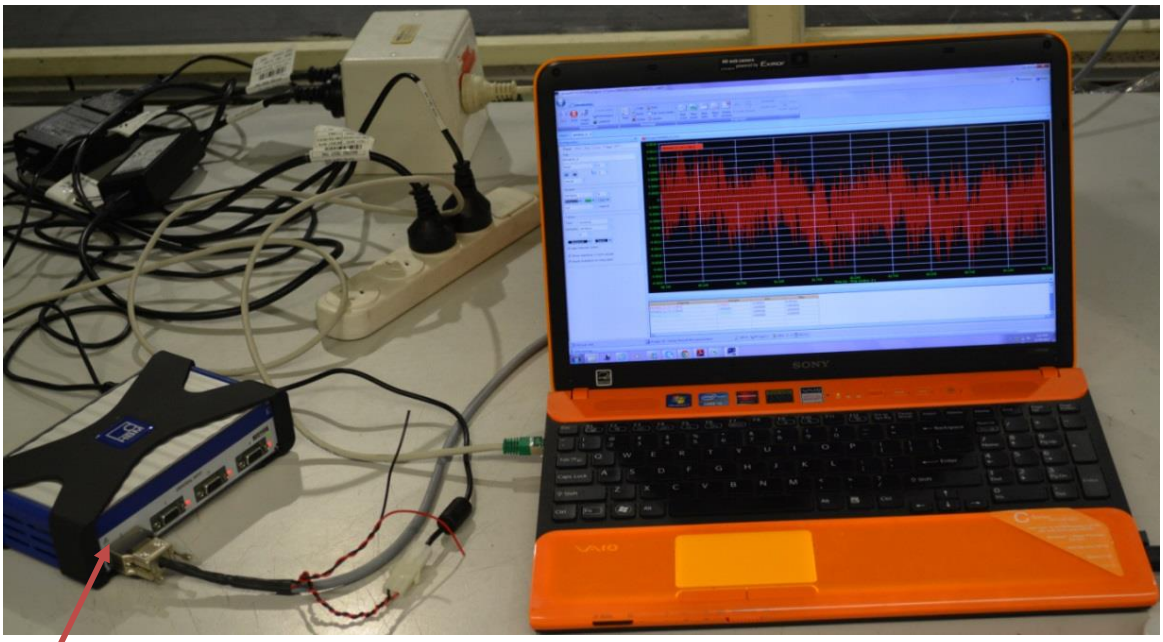

Figure 2.6: MX440A amplifier and HBM data acquisition software

2.4.2 Bearing and Housing

Two self-aligning ball bearings with bore diameter of 17 mm and outer diameter of 47 mm were used together with the housing. The bearings dynamic load ratings were 12543 N.

2.4.3 Flexible Coupling

A flexible beam coupling with bore diameter of 16 mm and length of 57.2 mm was used for the experiment of the wind turbine due to its robustness and light weight.

2.4.4 Torque Transducer

The HBM T20WN is primarily designed for measuring the static, dynamic torque and the rotational speed. It consists of an electronic sensor as well as an MX440A amplifier module. The HBM torque transducer has a nominal rotation speed of 10,000 revolutions per minute (RPM) and is capable of measuring both the torque and rotational speed simultaneously and has a maximum torque range of 5 N.m.

2.4.5 Overloading of Bicycle Shoe Brake

In the initial design, a bicycle shoe brake was used to provide Resistive torque. The bicycle shoe brake managed to provide resistive torque and bring the turbine to a stop. However, as the wind speeds increased at speeds above 20 km/h the bicycle shoe brake was unable to slow the turbine.

2.4.6 Changes to Test Set-up (Disk Brake)

A disk brake coupled with the turbine shaft and torque transducer was used to increase the resistive torque and to slow the turbine to a complete stop. The torque transducer was calibrated using pulleys and weights and the correlation between output voltage and applied load was found and validated.

2.4.7 Experimental Data Collection

Data was collected for the following three variables: torque generated, turbine rotational speed and controlled wind speed. Data was collected using a custom Catman® AP data acquisition software written by HBM. This application was run on aRMIT laptop.

2.4.7.1 Torque

A bicycle disk brake was used to provide resistance torque loads. All readings were taken dynamically as the turbine was slowly brought to a stall from its free spinning speed. The instantaneous torque readings was obtained from the Catman® AP data acquisition software.

2.4.7.2 Turbine Rotational Speed

The rotational speed of the turbine was measured instantaneously using the torque transducer. The Catman® AP data acquisition software was written to record instantaneous turbine rotational speeds.

2.4.7.3 Wind Speed

The wind speed was recorded using a modified National Physical Laboratory (NPL) ellipsoidal head Pitot-static tube as shown in Section 2.2. The wind speed was validated using a battery power Testo 410-1/2 digital anemometer.

2.4.8 Data Acquisition

A laptop running a custom Catman® AP data acquisition program was used to record the readings from the torque transducer. The torque sensor is connected to a cable that feeds information to the MX440A amplifier which computes the applied torque and rotational velocity of the wind. Calibration of the sensor was carried out before and in between the tests.

2.5 Torque Measurements

The mechanical power generated by the turbine is directly proportional to the torque and angular velocity. A torque transducer is used to determine both the torque and angular velocity of the turbine. The HBM T20WN was utilised, which is primarily designed for measuring the static, dynamic torque and the rotational speed, consists of an electronic sensor as well as an MX440A amplifier module was used. The torque sensor is connected to a cable that feeds all the information to the MX440A amplifier which computes the torque and rotational velocity of the wind turbine as shown in Figure 2.6. HBM torque transducer has a nominal rotation speed of 10,000 revolutions per minute (RPM) which is well above the expected maximum rotational speed the wind turbine can reach during testing. Calibration of the sensor was carried out before and in between the tests. The HBM T20WN is capable of measuring both the torque and rotational speed simultaneously and has a maximum torque range of 5 N.m.

2.6 Measurements of Turbulence by a Cobra Probe

The cobra probe is a four-hole pressure probe used to measure the three orthogonal mean and turbulent velocity components in the wind tunnel. A schematic of the probe is shown in Figure 2.7. The probe has a relative frequency response of 0 Hz to 2000Hz. The Cobra Probes are fully calibrated by Turbulent Flow Instrumentation and ready to use. Dedicated software was used to get the real-time velocity components u, v and w from the pressure files. Local yaw and pitch angles, Reynolds stresses and frequency spectra can be calculated. The probe was traversed via a computer control interface on the data acquisition Personal Computer

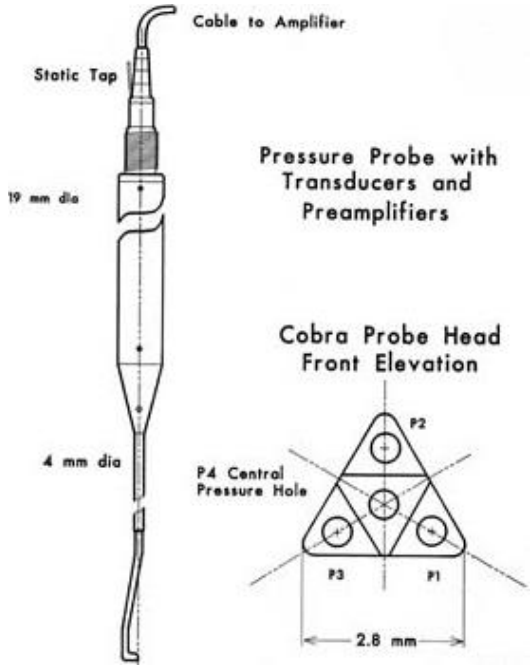

Figure 2.7: A schematic of a multi-hole pressure probe (from Hooper, 1997)

2.7 Calibration and Accuracy

It is essential to determine the degree of influence of errors associated with the experiment that may have upon the overall results acquired. The acquisition such as dynamic pressure, velocity, forces and moments in the wind tunnel are influenced by many factors such as air fluctuations. Therefore it is necessary to address these errors and apply correct measures to minimize the consequences of these errors.

2.7.1 Repeatability of Results

In order to verify the repeatability of the experimental data and increase the confidence level in the data, every single test conducted in the wind tunnel was performed three times. The data had a maximum variation of less than 1%. This was a good indication of the accuracy possessed by the measuring equipment.

2.7.2 Temperature and Pressure Errors

Running the wind tunnel for a period of time can significantly affect both the temperature and pressure in the tunnel due to temperature rise in the tunnel caused by the hub of the tunnel fan due to friction. Close observation of these two properties indicated that there was a slight fluctuation in the readings. The fluctuation in both the temperature and pressure were accounted for in the acquisition of the data and correct measures were taken to rectify the problem.

2.7.3 Wind Tunnel Speed Errors

The air speed in the wind tunnel was measured using an ellipsoidal head Pitot-static tube which is connected to a MKS Baratron reference pressure transducer. The air speed has a cubic effect on wind turbine power output. In order to verify the readings obtained from the MKS Baratron pressure transducer, the air speed was also measured with a hand held Anemometer. The variation of the wind tunnel air speed was found to be less than 1%.

CHAPTER 3

Wind Turbine Model and Prototype Design and Development

3.1 Turbine Prototypes Characterisation

The blade shape of each turbine is semi-circular with zero twisting. It is single stage turbine. The schematic of 16-blade turbine (top view) is shown in Figure 3.1. Physical dimensions of the blade are shown in Figure 3.2. The blade height, H = 160 mm, blade diameter, d = 36 mm and the blade thickness, t = 2 mm. A 3-D model of the same configuration along with the physical dimensions is illustrated in Figure 3.3. The blades are installed around the circumference of the turbine by providing equal space with a clearance ‘c’ between two subsequent blades.

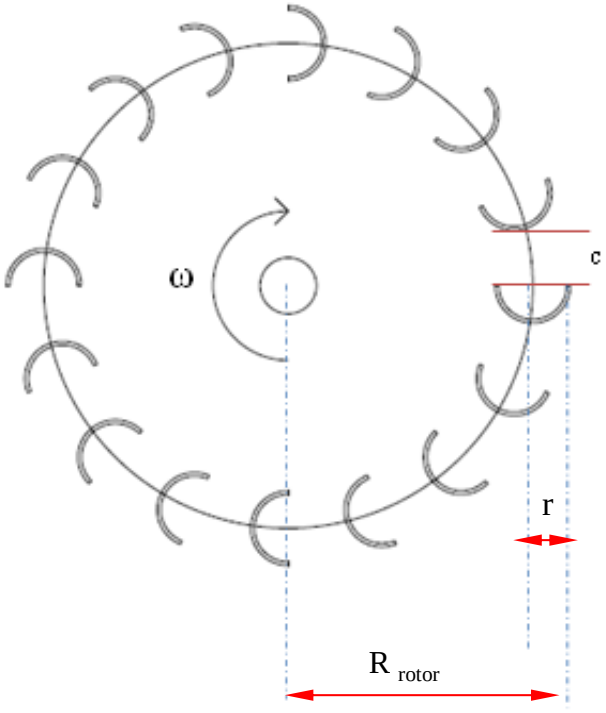

Figure 3.1: Schematic of the 16 blades turbine

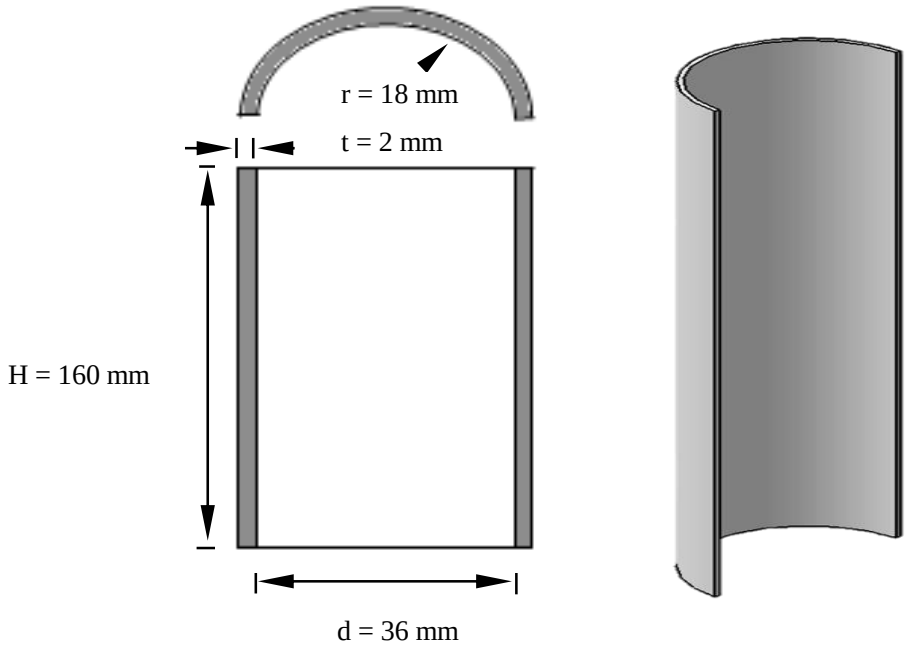

(a) Top view (b) Isometric view

Figure 3.2: Semi-circular shaped turbine blade

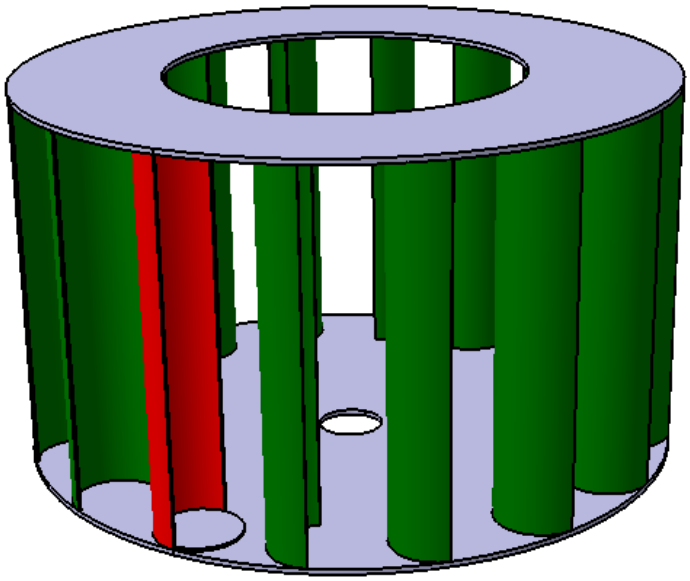

Figure 3.3: A 3D CAD model of a 16 blades turbine

3.1.1 Turbine Prototypes

Six single stage multi-blade drag-based vertical axis wind turbines of 300 mm diameter with various blade configurations have been designed. The prototype turbines' blade numbers are: 8, 16, 24, 32, 40 and 48. The blades are installed around the circumference of the turbine by providing equal space with a clearance 'c' between two subsequent blades. The blades are secured by two circular discs, made of Suntuf™ clear acrylic rigid plastics (top & bottom). The height of the turbine is 160 mm. The blades are made of PVC to provide structural rigidity. All six prototype turbines are shown in Figures 3.4 and Figure 3.5.

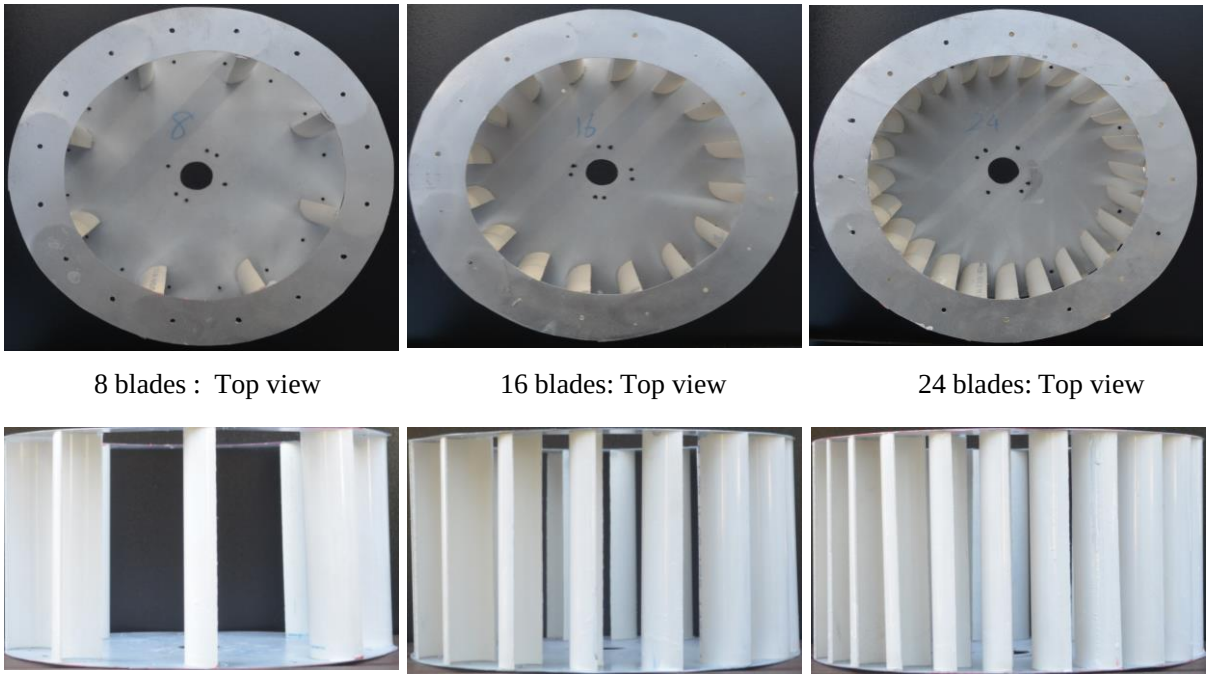

8 blades : Top view | 16 blades: Top view | 24 blades: Top view

8 blades : Side view | 16 blades : Side view | 24 blades : Side view

Figure 3.4: Prototype turbines top and side views (8, 16 and 24 blades)

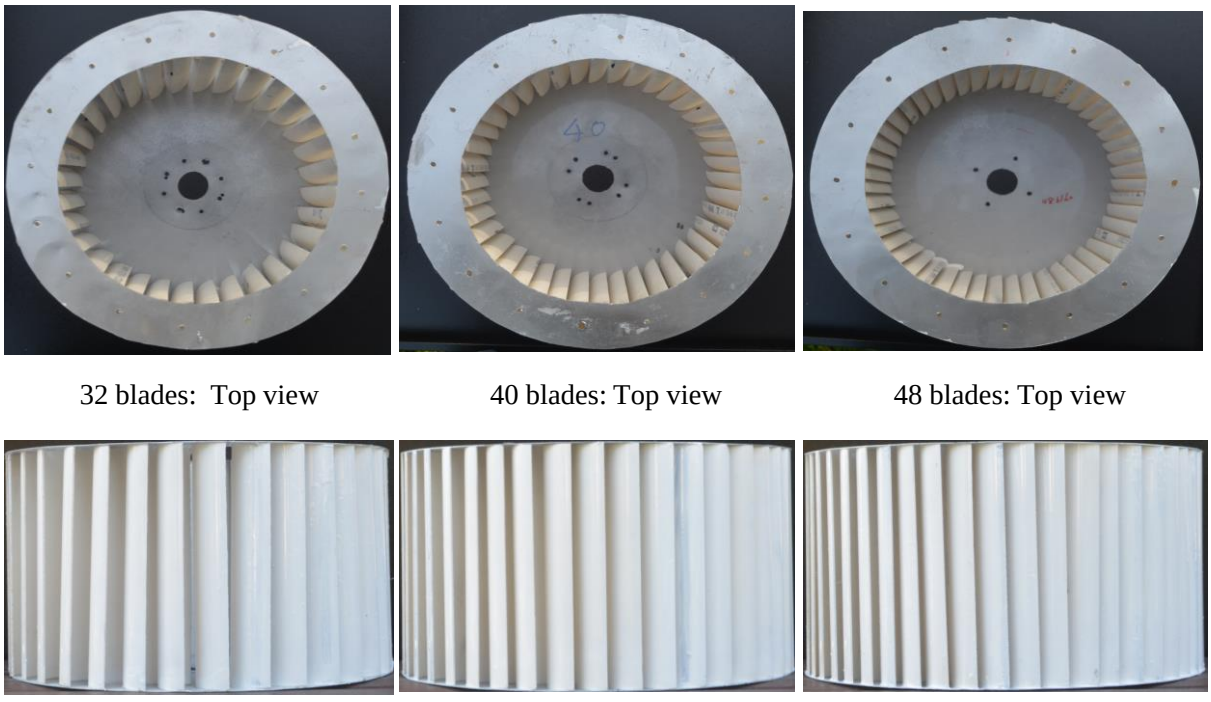

32 blades: Top view | 40 blades: Top view | 48 blades: Top view

32 blades : Side view | 40 blades : Side view | 48 blades : Side view

Figure 3.5: Prototype turbines top and side views (32, 40 and 48 blades)

3.1.2 Measurement of Clearance between Two Subsequent Blades for 300 mm Diameter Turbine

The clearance 'c' between two subsequent blades for 16, 32 and 48-blades turbine is shown in Figure 3.6. As expected, the clearance between the two subsequent blades decreases with the increase of blade number. The clearance for each set of turbine was measured and shown in Table 3.1. The clearance becomes negative (overlapped) beyond 40-blade configuration.

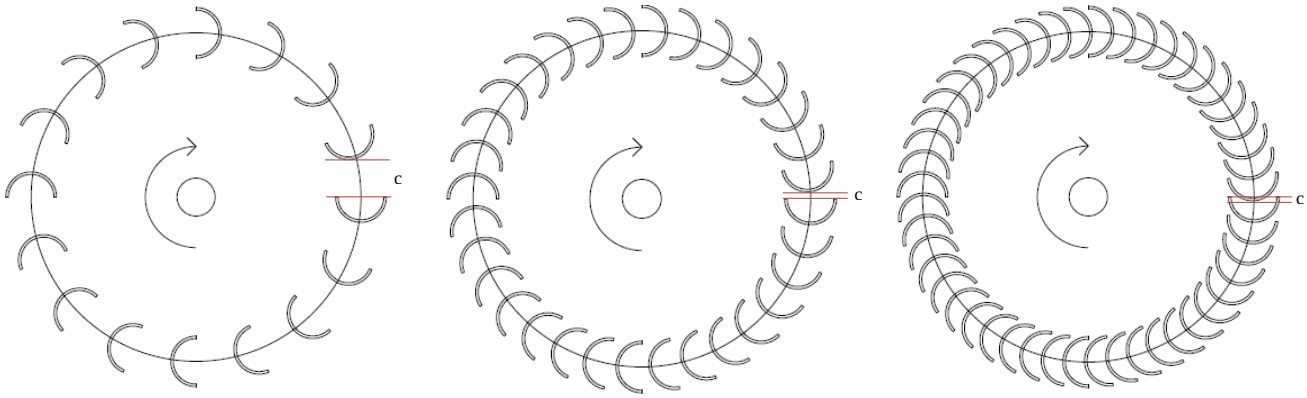

Figure 3.6: Top view of 16, 32 and 48 blades wind turbine

Table 3.1: Blade number and clearance between two subsequent blades for a 300 mm diameter turbine

Blade No. (N)	Predicted Clearance (c) by Equation (mm)	Measured Clearance (c) from Prototype (mm)	Clearance Error (%)
8	82.00	81.00	1.23
16	31.00	30.50	1.64
24	14.00	13.70	2.19
32	5.50	5.40	1.85
40	0.50	0.49	2.04
48	-3.00	- 2.95	1.69

3.2 Cowling

Cowling is used to eliminate the negative torques which prevents the turbine from accelerating to higher torque producing speeds. A cowling was designed in such a way that it can enclose the turbine with a small clearance and can guide the incoming wind through a defined inlet and push the turbine and finally channel out the wind through the confined outlet to the environment. The cowling was constructed with two hollow PVC cylinders. The outer cylindrical shell is 360 mm in diameter and half of its frontal area is kept closed to prevent the incoming wind hitting the convex side of the returning blade. The inner shell with 160 mm diameter has an opening to allow the swept wind to exit the turbine through the top instead of at the rear to eliminate the second negative torque. Figure 3.7 (a) shows the 3D model of the cowling and Figure 3.7 (b) represents the turbine fitted with the cowling.

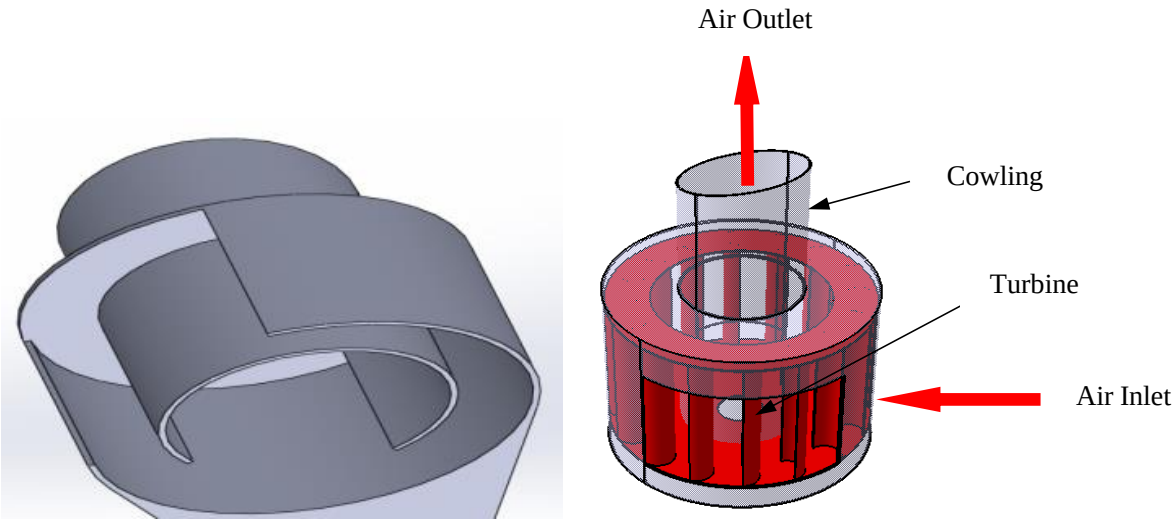

(a) 3-D model of cowling (b) Wind turbine with cowling

Figure 3.7: Cowling

3.3 Torque and RPM Measurement Methodology

Tests were undertaken at RMIT Industrial Wind Tunnel. It is a closed return circuit wind tunnel with a rectangular test section (3 m width, 2 m height and 9 m length). The maximum wind speed of the tunnel is approximately 145 km/h.

Two experimental setups were used: (a) a vertical support mounted on the tunnel floor to measure the torque and rpm of different prototypes and (b) a moveable test rig table to place the turbines at different position in the wind tunnel.

3.3.1 Development of a Wind Turbine Support Mounting

A vertical support and torque transducer setup was developed as shown in Figure 3.8. Detailed information about the torque sensor can be found in Section 2.4. A vertical support was developed to position the turbine in the test section of the wind tunnel. The setup was positioned 200 mm above the tunnel floor to avoid the tunnel boundary layer effect.

A braking device was developed to measure the correct torque generated by the wind turbine. Detailed information about the brake mechanism can be found in Section 2.4. The braking device is utilised to dampen the rotational energy of the rotating wind turbine. Initially, a bicycle brake shoe was used in the experiment. However, it did not provide sufficient grip and was deemed inefficient. Alternatively, a simple bicycle disc braking device was used to apply a resistive force which enables us to slowly dampen the rotational energy. The resistive force would be applied until the wind turbine came to a complete stop and the torque would be recorded. The mechanical power generated by the wind turbine is proportional to:

$$P_{Turbine} = T \times \omega \tag{3.1}$$

Where:

T= Torque (N.m)

ω= Rotational speed (rad/s)

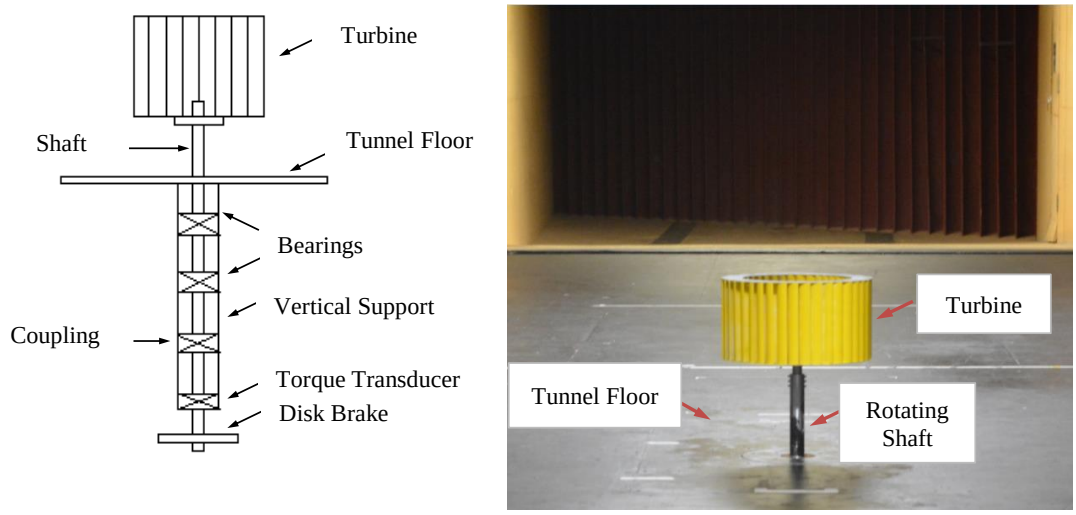

(a) Schematic of support and torque transducer setup (b) Wind tunnel setup

Figure 3.8: Experimental setup in RMIT wind tunnel

3.3.1 Development of a Moveable Test Rig

In order to measure the torque generated by the wind turbine at different turbulence intensities, a moveable test rig table was used. The setup was positioned and fixed properly on top of the movable test rig table. The test rig table was placed at different position in the wind tunnel. The experimental setup of a Moveable Test Rig is shown in Figure 3.9.

Figure 3.9: Moveable test rig experimental setup

3.3.2 Effect of Blade Number

To measure various parameters (i.e., torque, turbine speed) at different wind speeds, the experimental setup was positioned and fixed at the middle of the wind tunnel test section as shown in Figure 3.10. Six different turbines with different blade number (i.e., 8, 16, 24, 32, 40 and 48 blades) without any cowling device were tested.

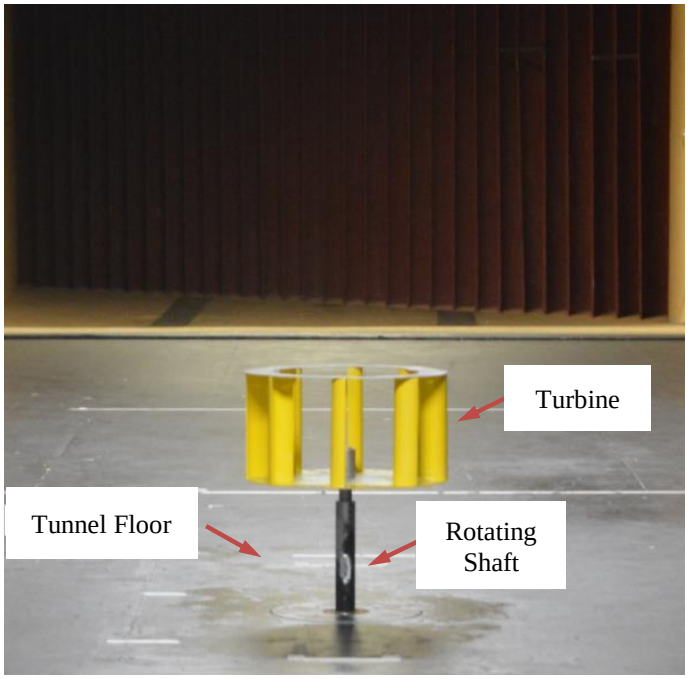

Figure 3.10: Experimental setup inside industrial wind tunnel

3.3.3 Effect of Yaw Angle Orientation (Blade Angle)

In order to investigate the effect of blade angle on the wind turbine performance, the wind turbine blade was tested in the wind tunnel at different yaw angles ranging between 0° to 30° at an increment of 10°. Figure 3.11 shows the schematic of blade angle. Positioning the blade at different yaw angles enables for the evaluation of the aerodynamic forces exerted on the blade and also on the flow separation from the blade.

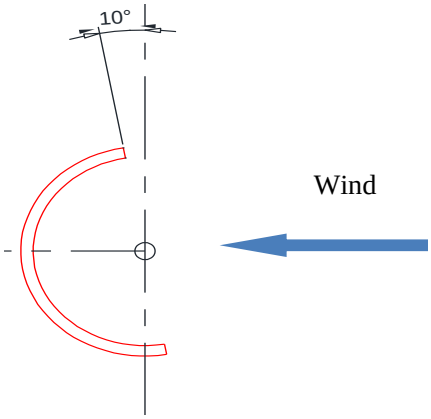

Figure 3.11: Schematic of blade angle

3.3.4 Effect of Cowling

The study on effect of cowling device on the performance of the wind turbine was undertaken. The cowling devise used in the wind tunnel testing is shown in Figure 3.12 (a).. The experimental setup with the turbine is shown in Figure 3.12 (b). The experimental setup of the turbine with the cowling in the wind tunnel test section is shown in Figure 3.12 (c).

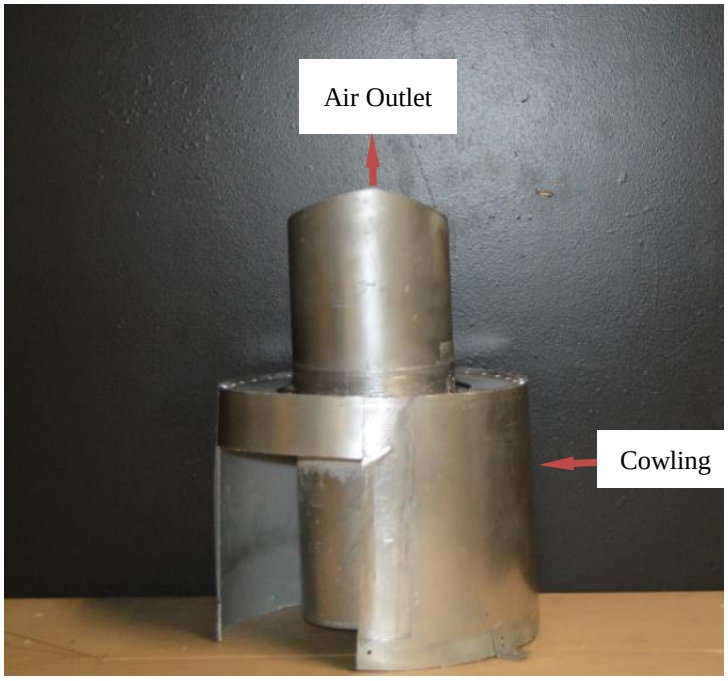

(a) Cowling

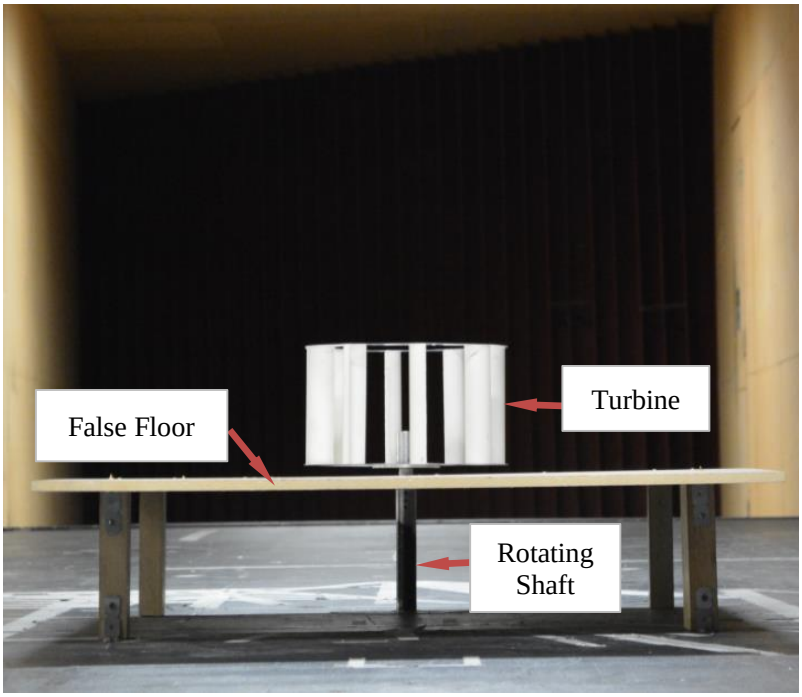

(b) Experimental setup of turbine without cowling

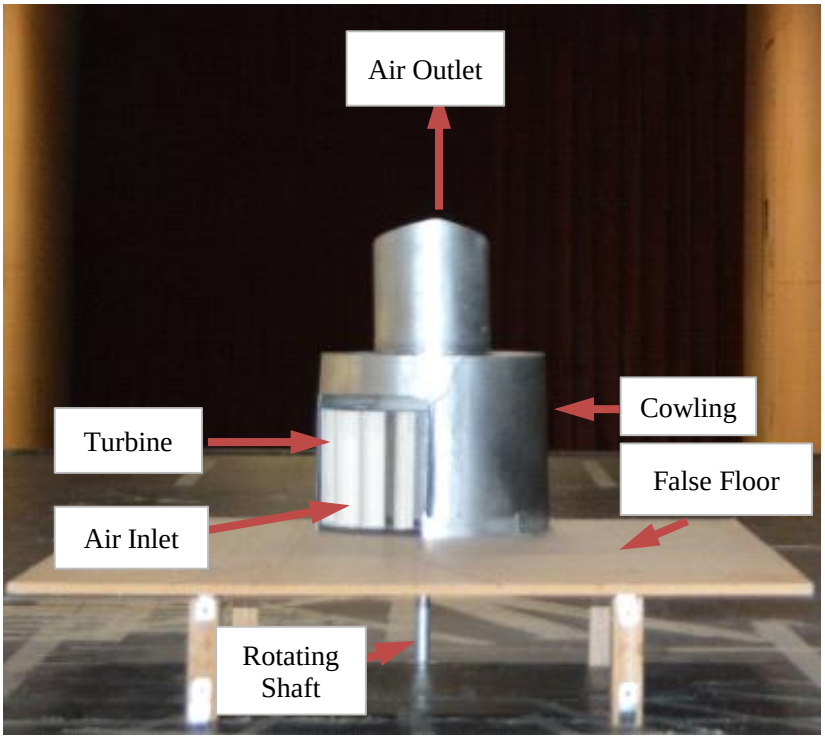

(c) Experimental setup of turbine with cowling in the wind tunnel test section

Figure 3.12: Experimental setup in the wind tunnel test section for cowling

3.3.5 Effect of Scaling

The single stage multi-blade drag-based VAWT used for this study is a semicircle shaped blade made from PVC material. Two sets of 8, 16 and 24-bladed turbines were manufactured. One set of 8, 16 and 24-bladed turbine with turbine diameter of 300 mm and blade length of 160 mm and diameter of 40 mm (base modal) was initially designed. A second set of 8, 16 and 24-bladed turbine with turbine diameter of 600 mm and blade height and diameter of 320 mm and 80 mm respectively was manufactured. Detailed dimensions of the blade are shown in Figure 3.13.

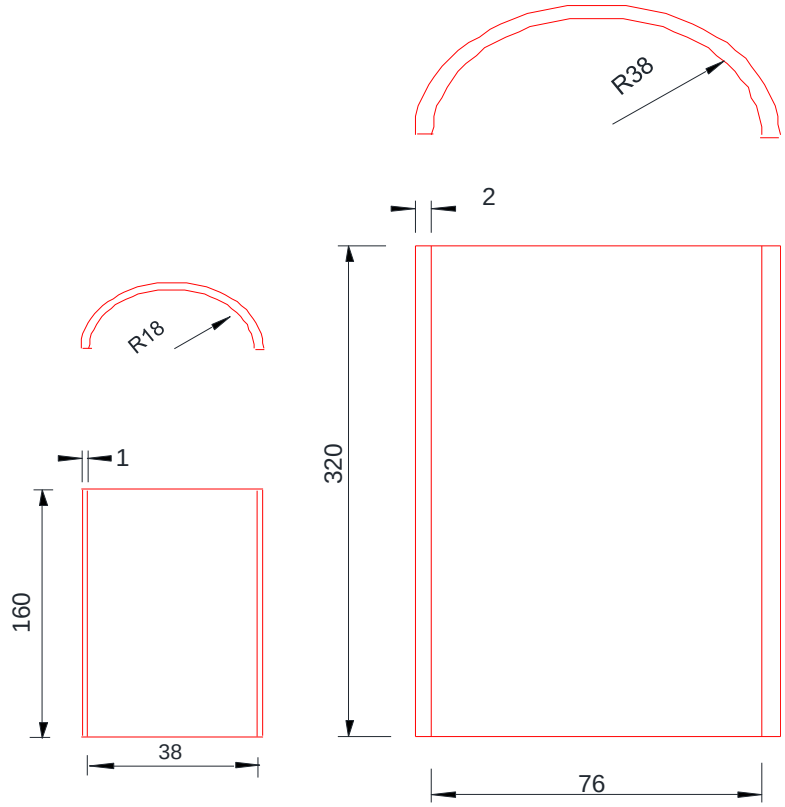

(a) Base model (b) Modified model

Figure 3.13: Dimensions (mm) of the semicircle shaped wind turbine blade

The prototype comparison between the 8 blade turbines is shown in Figure 3.14 (a). Similarly, prototype comparison between the 16 blade turbines and 24 blade turbines is shown in Figure 3.14 (b) and (c) respectively.

(a) Prototype 8-blade turbine

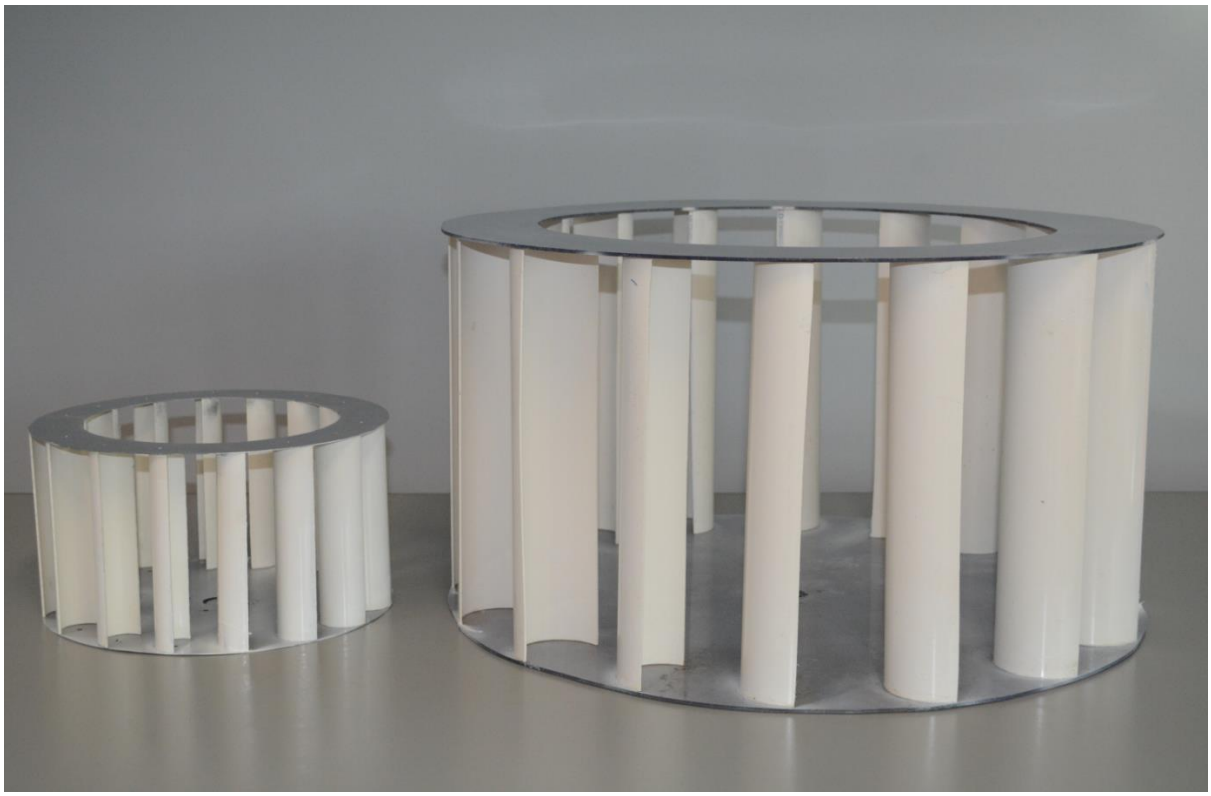

(b) Prototype 16-blade turbine

(c) Prototype 24-blade turbine

Figure 3.14: Prototypes of the 8, 16 and 24-blades Base Models and Double Size Turbine

3.3.6 Effect of Blade Radius

The effect of blade radius on the power output was studied by conducting experimental investigation. Three sets of 8 blades turbine was constructed by keeping the turbine diameter (300 mm) and blade length (160 mm) constant but varying the blade diameter (20 mm, 40 mm and 80 mm) respectively. Figure 3.15 (a) shows the detailed dimensions of three sets of 8 blades. The prototype comparison between the 8 blade turbines is shown in Figure 3.15 (b).

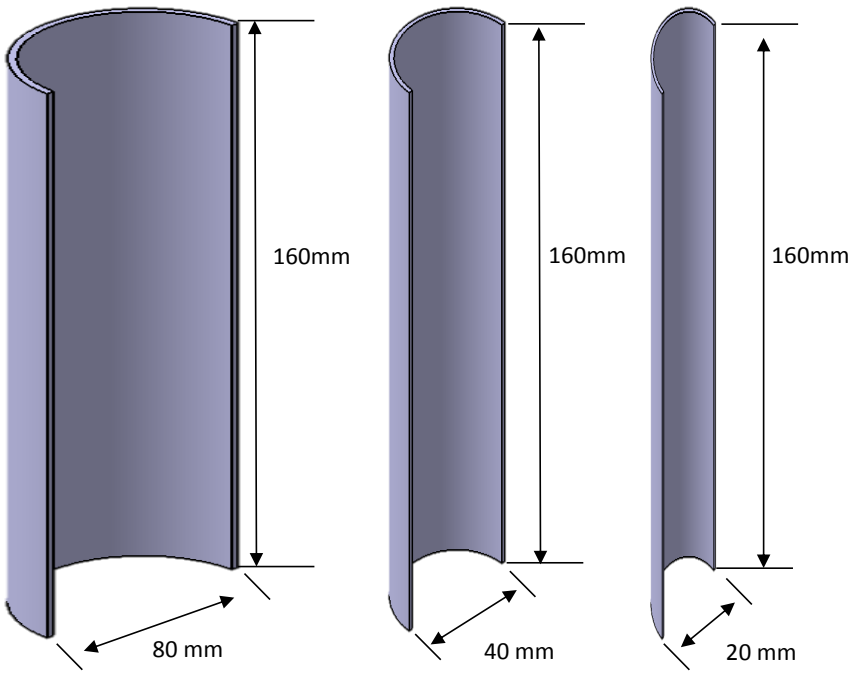

(a) Dimensions of modified blades

a) 20 mm b) 40 mm c) 80 mm

(b) Prototype of 8-bladed turbine

Figure 3.15: Prototypes of 8-bladed turbine with modified blades

3.3.7 Effect of Turbulence

Turbulence was generated in the RMIT Industrial Wind Tunnel using 3 different passive grids. In order to generate turbulence inside the wind tunnel, wooden grids were placed at the inlet of the tunnel with a cross section of 6 m^2. A 50% blockage ratio was maintained using 3 different grids (small, medium and large) as shown in Figure 3.16, Figure 3.17 and Figure 3.18. The three grids had the same total blockage area: 3m^2. Experimental setup inside the

wind tunnel from the downstream is shown in Figure 3.16 (b), Figure 3.17 (b) and Figure 3.18 (b). The turbulence intensity was measured by keeping the inlet velocity constant at 8.5 m/s. The turbulence reading at each position was obtained using the Cobra Probe. The effect of turbulence was measured by keeping the input velocity constant and varying the distance of the turbine from the grid position from 0 to 7.5 m as shown in Figure 3.19 and Figure 3.20.

Turbulence Intensity was calculated using the equation below:

$$I_{uu} = \frac{\sqrt{\overline{u'^2}}}{|\overline{V}|} = \frac{\sigma_u}{|\overline{V}|} = \frac{stddev(u)}{|V|} \tag{3.2}$$

Where,

I_{uu} = Turbulence intensity component

V=Instantaneous, time-averaged and time varying local velocity vector

u' =Time varying (non-mean) velocity component

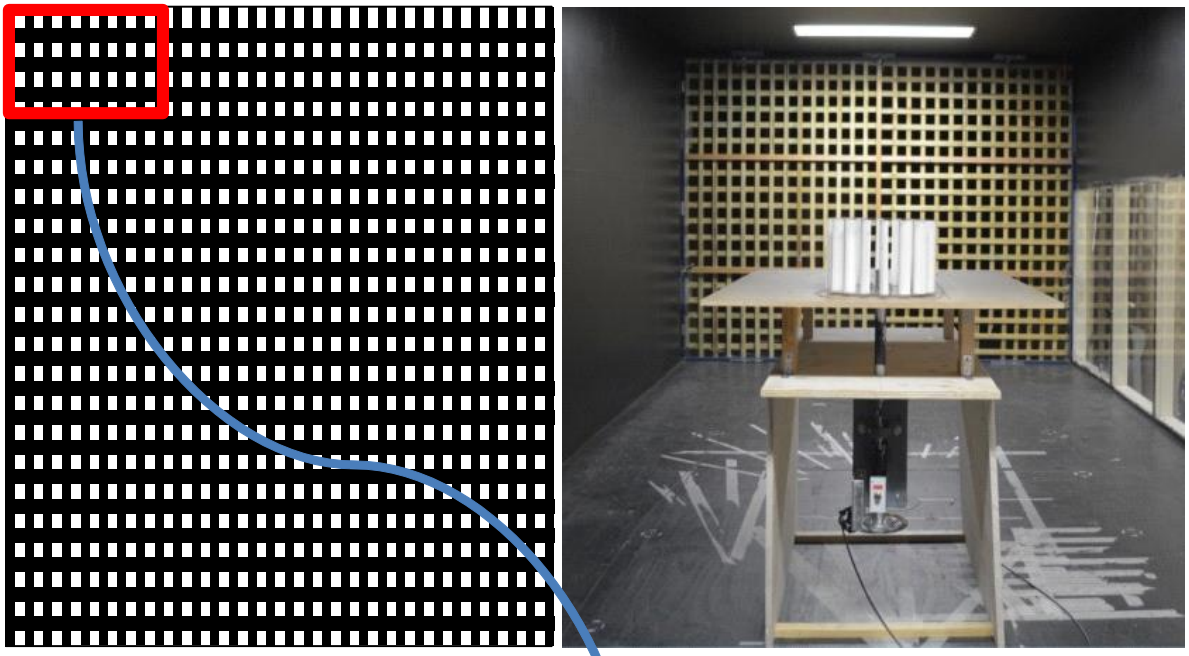

(a) Schematic of small grid

(b) Small grid in wind tunnel test section

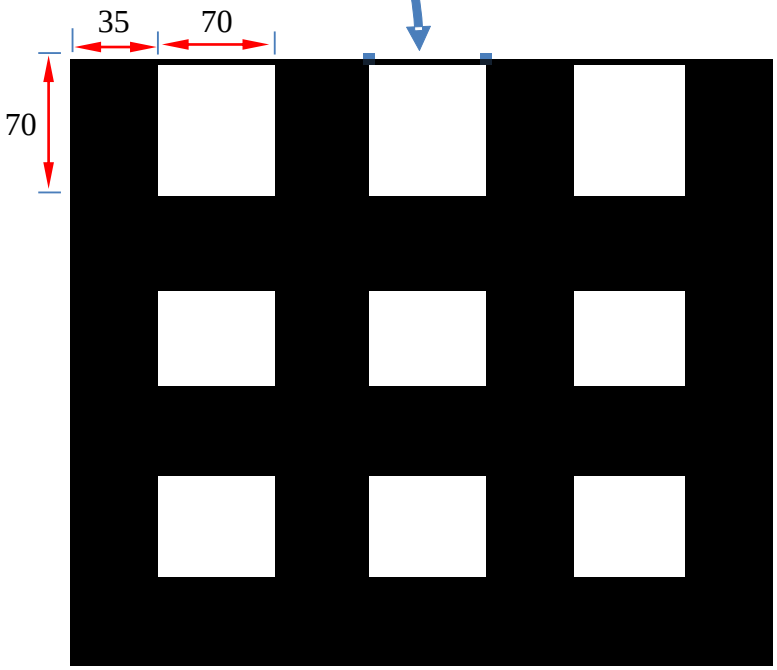

(c) Blown -up view of small grid

Figure 3.16: Turbulence generation using small grid

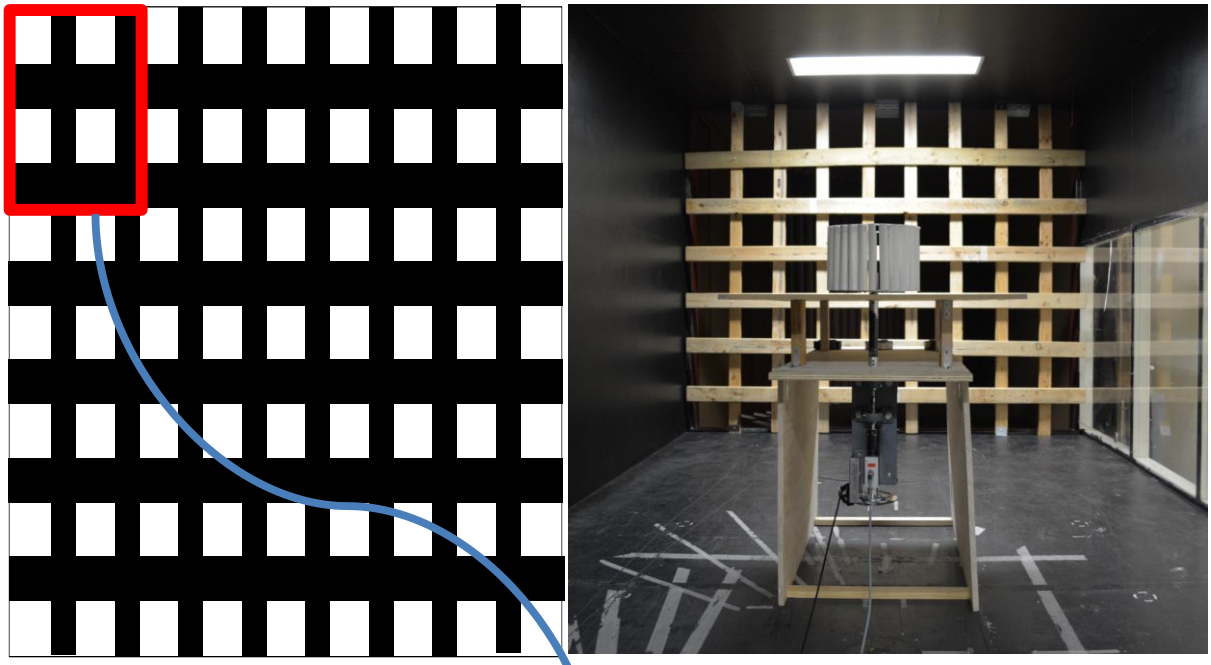

(a) Schematic of medium grid (b) Medium grid in wind tunnel test section

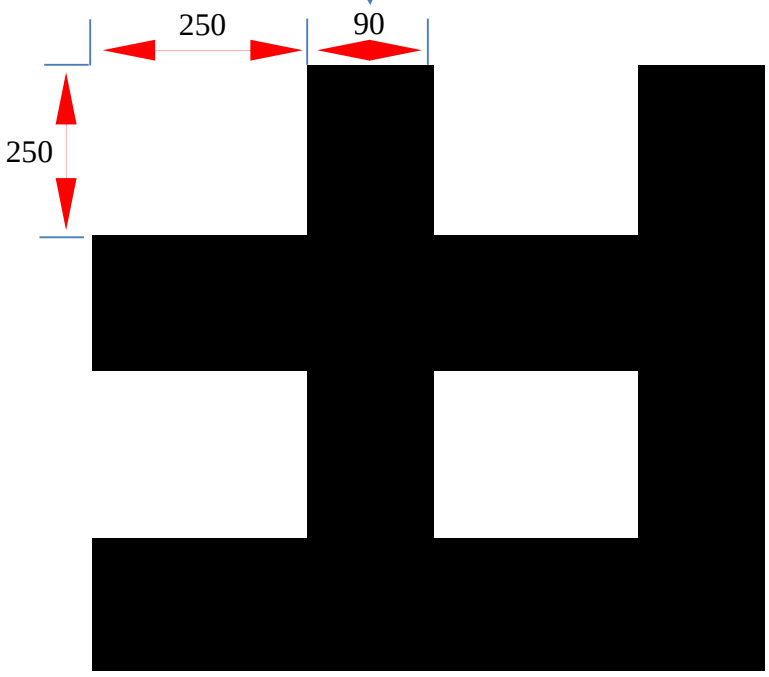

(c) Blown-up view of medium grid

Figure 3.17: Turbulence generation using medium grids

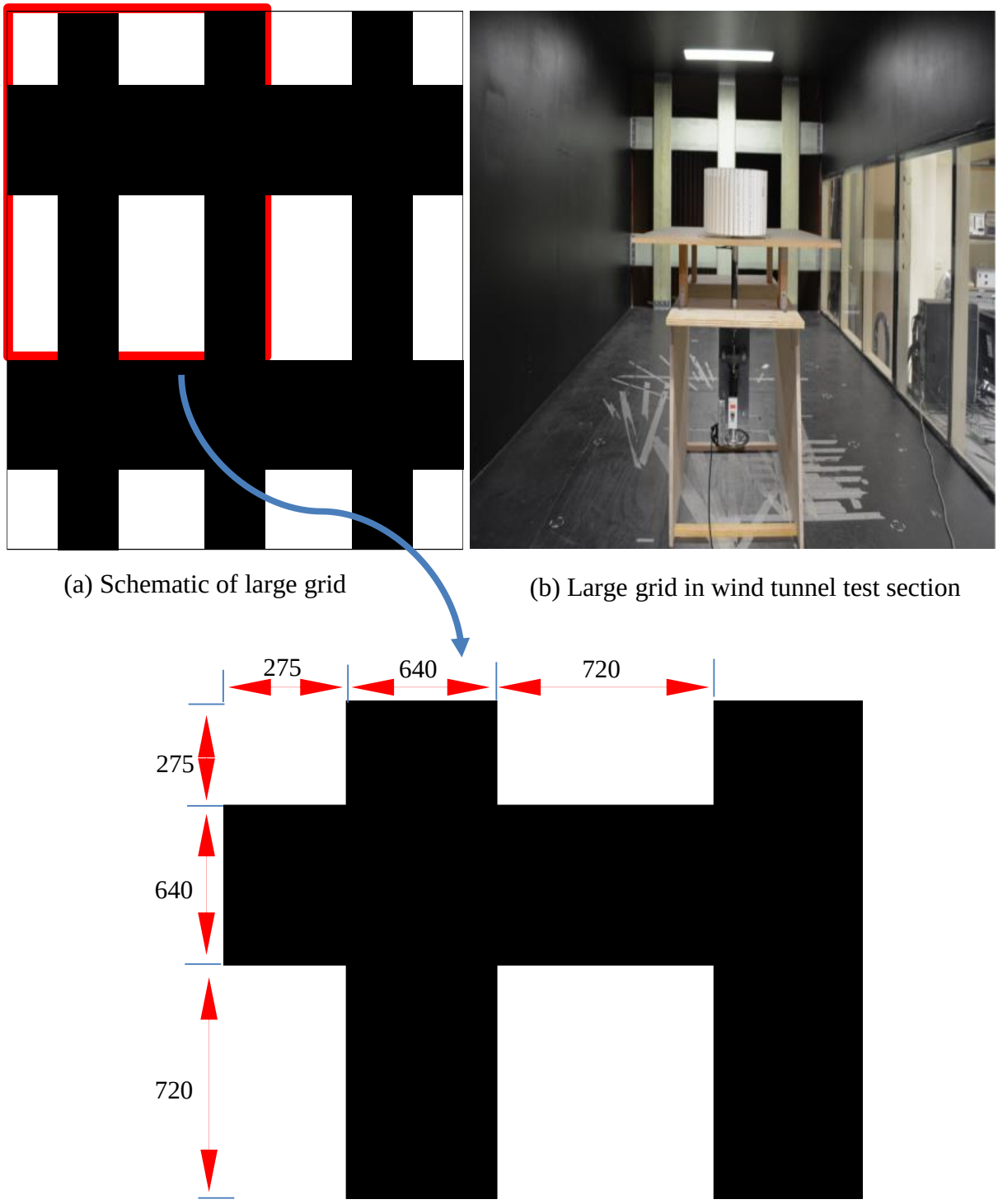

(a) Schematic of large grid

(b) Large grid in wind tunnel test section

(c) Blown-up view of large grid

Figure 3.18: Turbulence generation using large grids

Table 3.2: Turbulence Intensity for 50% Blockage Ratio

	Turbulence %		
Distance (mm)	Small grid	Medium grid	Large grid
1500	15.5	-	-
2250	11.5	-	-
3000	9	17	31
4500	7	12	28
6000	6	10	22
7500	4.5	8	17

Each position of the turbine from the grid which was placed in the contraction section of the wind tunnel is shown in Figure 3.19 and 3.20. The turbine is placed at the specific positions to study the effect of turbulence. The turbulence intensity decreases as the turbine distance increases as shown in Table 3.2 Position one is 1500 mm away from the grid, position two is 3000 mm, position three is 4500 mm, position 4 is 6000 mm and position five is 7500 mm from the grid. The plan view of setup positions in the wind tunnel is shown in Figure 3.21.

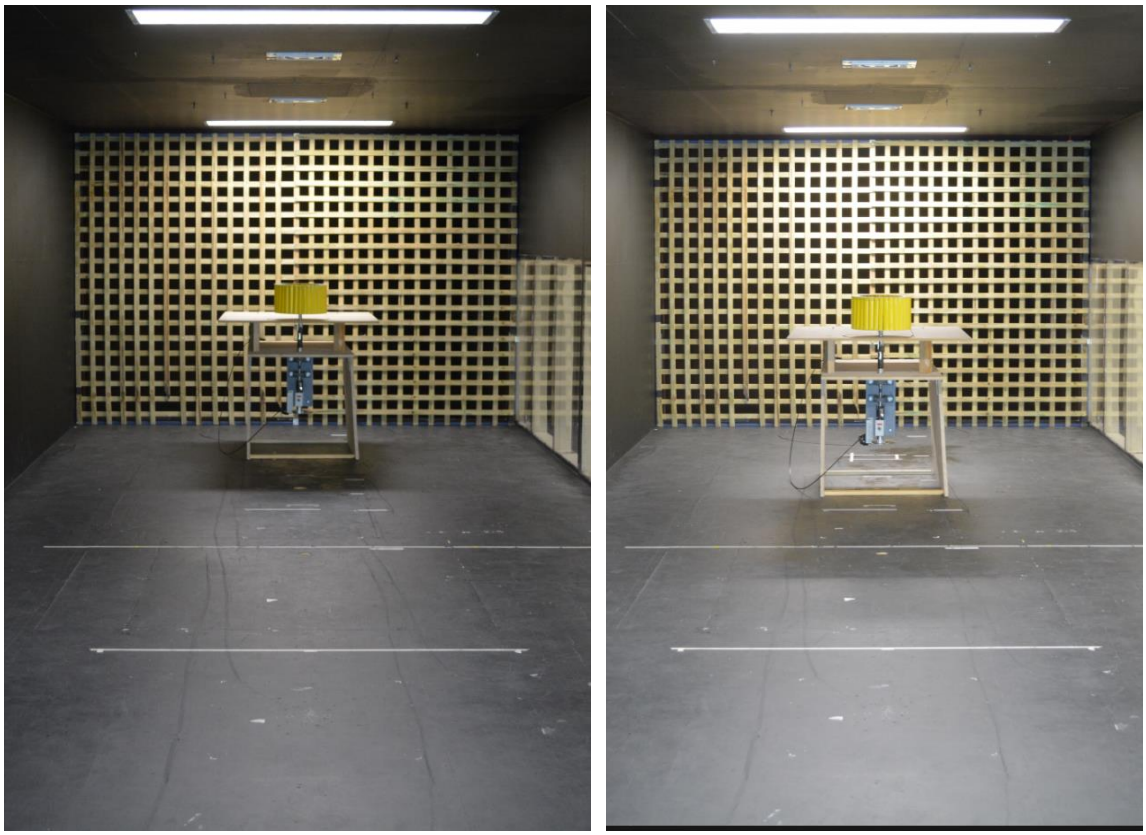

(a) Position 1 (b) Position 2

Figure 3.19: Setup positions in the wind tunnel (Position 1 & 2)

(c) Position 3

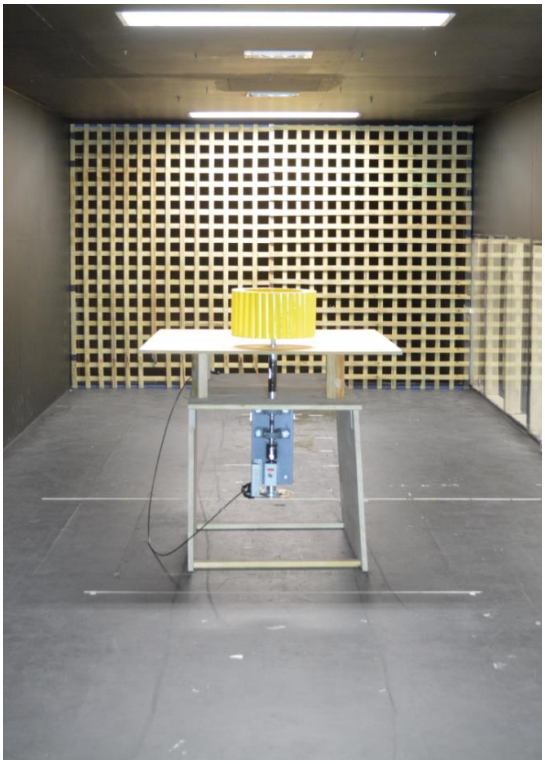

(d) Position 4

(e) Position 5

Figure 3.20: Setup positions in the wind tunnel (Positions 3, 4 & 5)

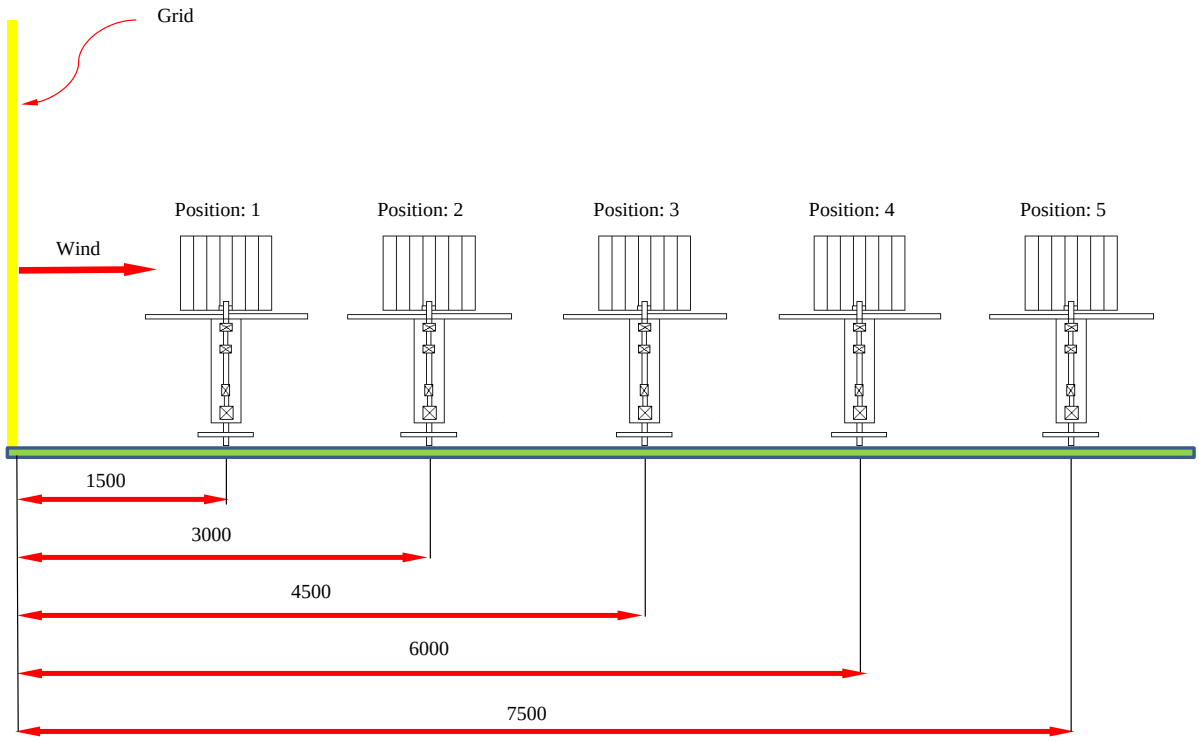

Figure 3.21: A plan view of setup positions in the wind tunnel

3.4 Development of Blade-Number Prediction Methodology

Four single stage drag-based vertical axis wind turbine prototypes with various blade configurations (18, 19, 20 and 21) have been designed and manufactured. The shape of the blade is semi-circular with zero twisting. The schematic of a 19-blade turbine (top view) is shown in Figure 3.22. The blades are installed around the circumference of the turbine by providing equal space with a clearance 'c' between two subsequent blades. Physical geometric dimensions of blade are shown in Figure 3.23. The blades are secured by two circular discs, made of Suntuf™ clear acrylic rigid plastics (top & bottom). A 3-D model of a 19 blades prototype turbine along with the physical dimensions is illustrated in Figure 3.24. The blade is made of PVC material to minimise the cost. The PVC material provided good structural rigidity.

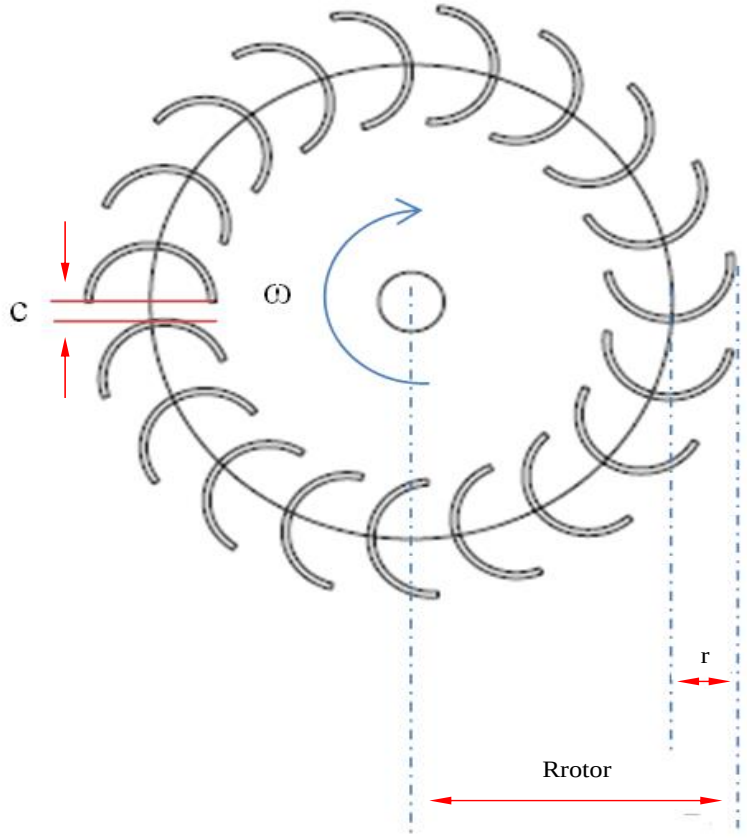

Figure 3.22: Schematic of the 19 blades turbine

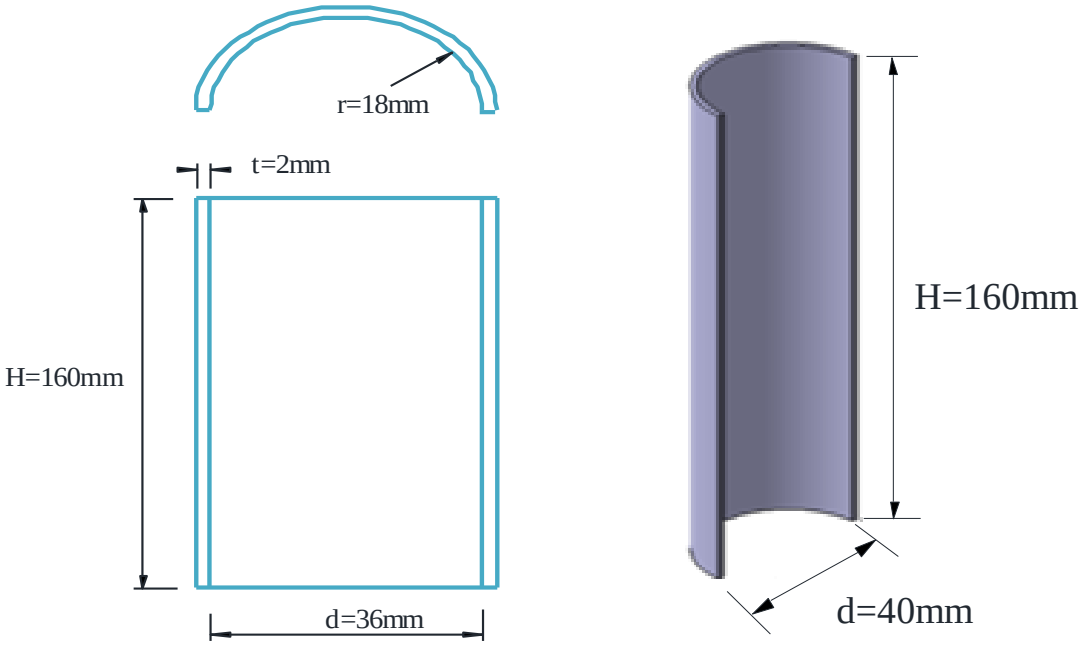

Figure 3.23: Semi-circular shaped turbine blade

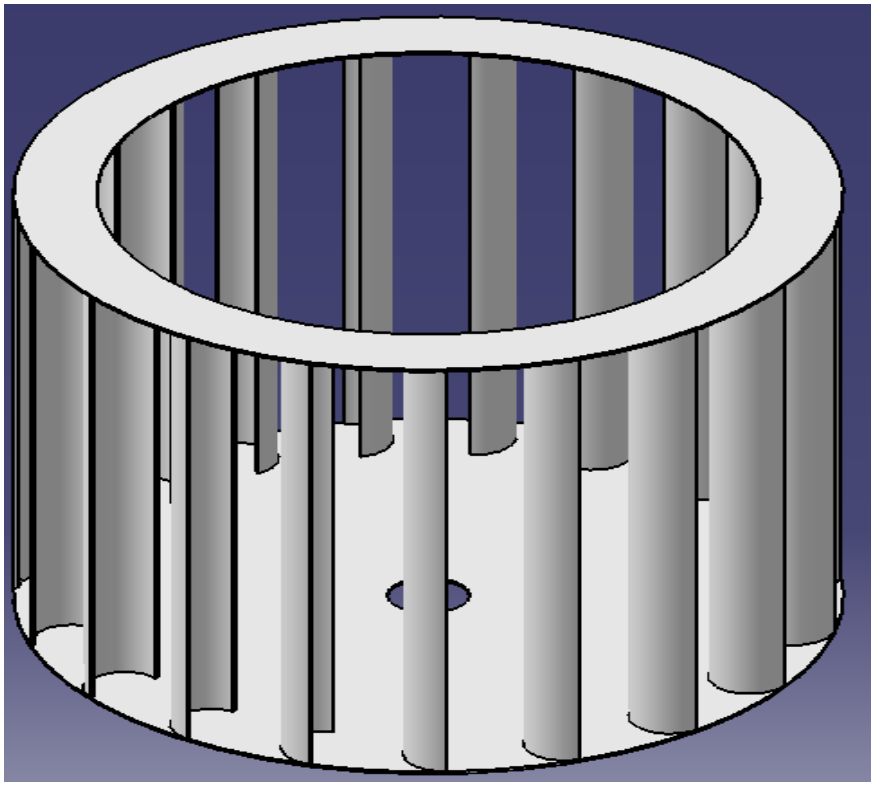

Figure 3.24: A 3D model of 19 blades turbine

All four configurations of the prototype turbine are shown in Figure 3.25 and Figure 3.26. The clearance ‘c’ between two subsequent blades for 18, 19 and 20-blades turbine is shown in Figure 3.27. As expected, the clearance between the two subsequent blades decreases with the increase of blade number. The clearance for each set of turbine was measured and shown in Table 3.3.

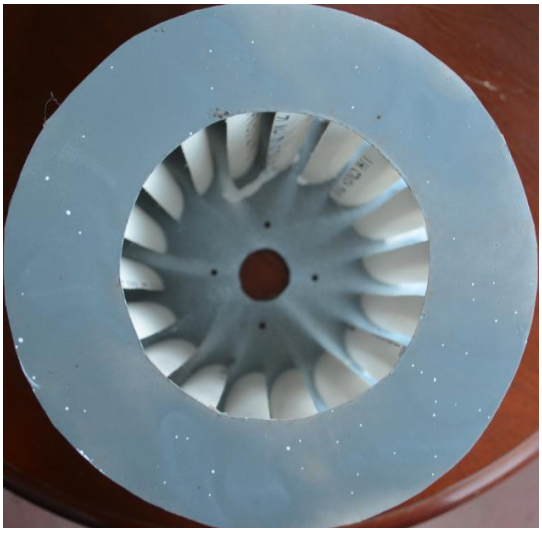

18 blades: Top view

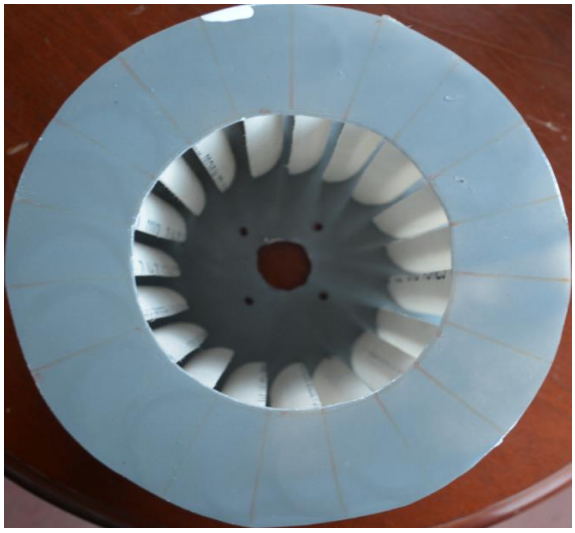

19 blades: Top view

18 blades: Side view

19 blades: Side view

Figure 3.25: 18 and 19 blade-prototype turbines

20 blades: Top view

21 blades: Top view

20 blades: Top view

21 blades: Top view

Figure 3.26: (b) 20 and 21 blade-prototype turbines

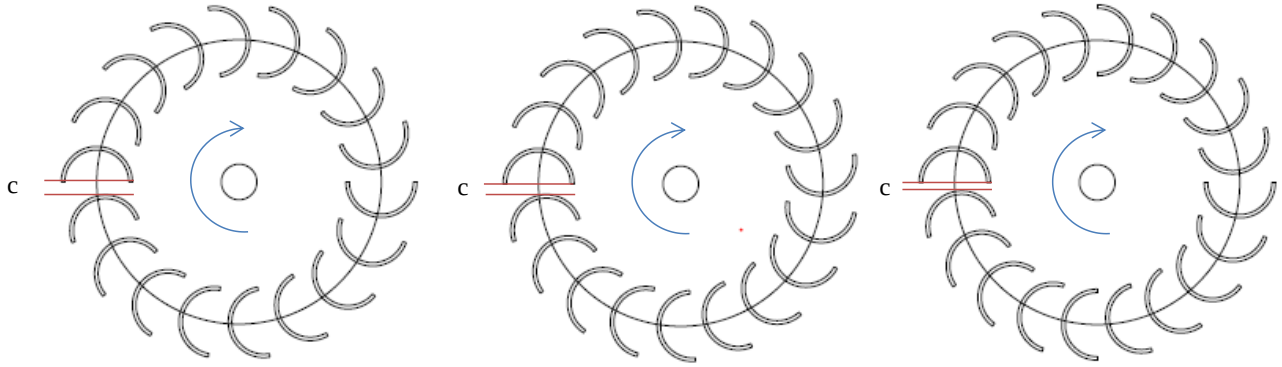

Figure 3.27: Top view of 18, 19 and 20-blades wind turbine with clearance ‘c’ between two subsequent blades

The predicted data is shown in the second column of Table 3.3. The measured clearance from the prototype is shown in the third column. The average variation of clearance between predicted and measured is less than 2%. The variation increases with the decrease of gap due to measurement inaccuracy.

Table 3.3: Blade clearance between 2 subsequent blades (measured and calculated)

Blade number (N)	Predicted Clearance (c) by Equation (mm)	Measured Clearance (c) from Prototype (mm)	Clearance Error (%)
18	7.93	7.80	1.7
19	6.46	6.34	1.9
20	5.13	5.00	2.6
21	3.94	3.87	1.8

3.5 Flow Visualization

Flow visualization was conducted in the RMIT Industrial Wind Tunnel using wool tuff and smoke flow visualisation. Six single stage drag-based vertical axis wind turbine prototypes with various blade configurations (8, 16, 24, 32, 40 and 48) were placed at the distance of 2 meters from the inlet of the tunnel. The wool tuff test on sixteen blades and thirty two blades turbine is shown in Figures 3.28 and 3.30. The flow visualization was conducted by keeping the inlet velocity constant at 4.5 m/s and using two experimental configurations. The first test was conducted by keeping the blades stationary as shown in Figures 3.28 and 3.30. Wool tuff was places at different locations around the turbine. The second test was conducted by allowing the turbine to rotate as shown in Figures 3.29 and 3.31

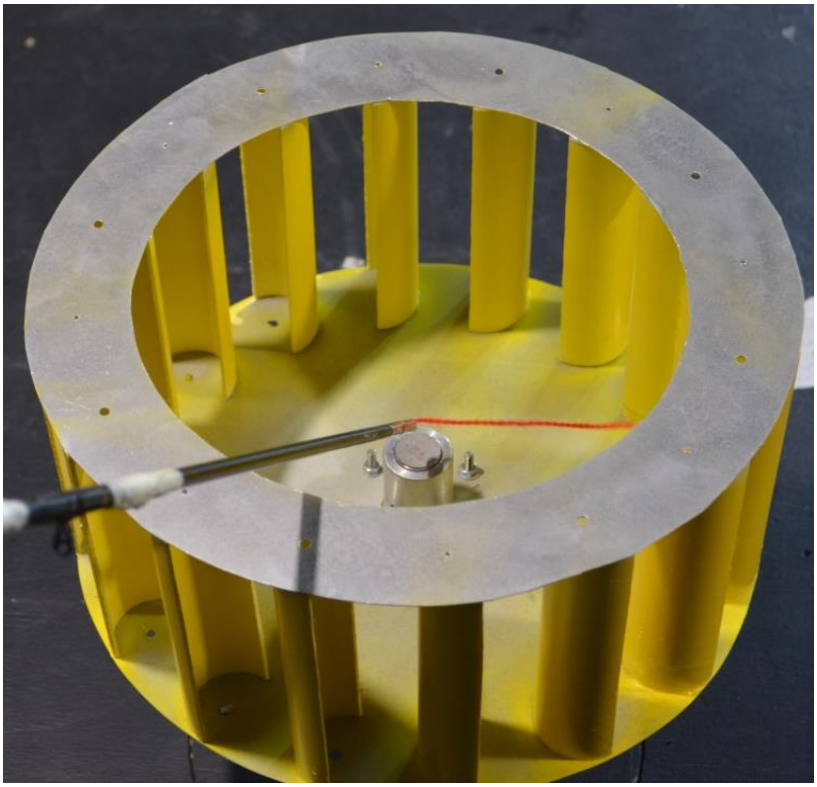

Figure 3.28: Flow visualisation around a 16 blades turbine in stationary

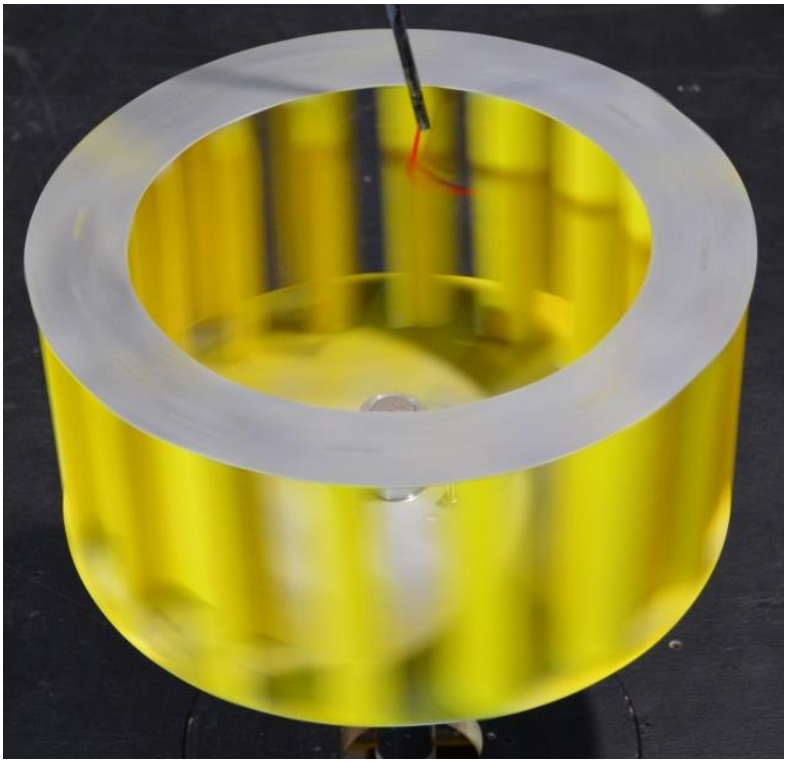

Figure 3.29: Flow visualisation around a 16 blades turbine in rotation

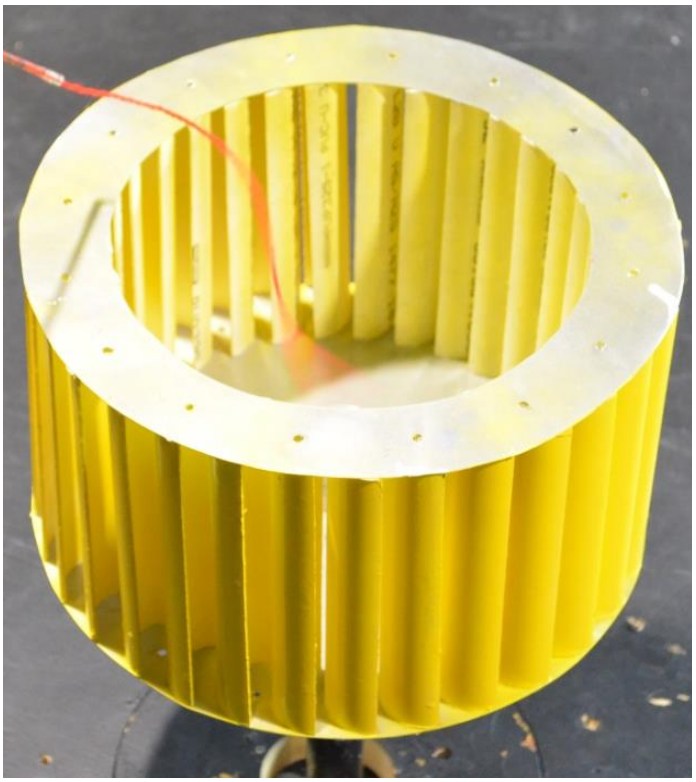

Figure 3.30: Flow visualisation around a 32 blades turbine in stationary

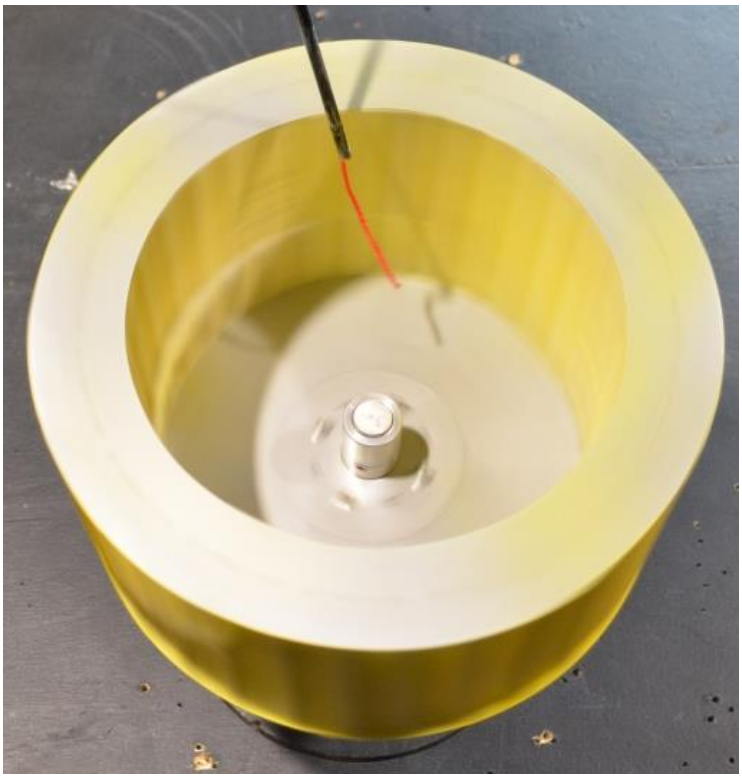

Figure 3.31: Flow visualisation around a 32 blades turbine in rotation

CHAPTER 4

Aerodynamic Behaviour of a Single Stage Multi-Blade Drag-Based VAWT

4.1 Multi-blade Vertical Axis Wind Turbine Aerodynamics

As mention in Chapter 2, vertical support mounted on the tunnel floor coupled with the torque sensor was used to evaluate the aerodynamic properties of multi-blades vertical axis wind turbine to develop an empirical relation for estimating the maximum torque output. Detailed information about the blade number and dimensions are given in Section 3.1. The principal aerodynamic parameters used in this study were torque and rpm, while the physical parameters of the turbines were turbine radius (R), blade number (N), blade radius (r), and clearance between two subsequent blades (c).

4.1.1 Effect of Blade Number on Turbine Efficiency

To study the effect of blade number on the power output of a simple multi-blade drag based vertical axis wind turbine for the application in built-up areas, six single stage multi-blade drag-based vertical axis wind turbine of 300 mm diameter with various blade configurations has been designed and tested in the wind tunnel environment using vertical support mounted on the tunnel floor methodology. Detailed information about the blade number and dimensions are given in Section 3.1.1.

4.1.1.1 Turbine Power and Rotational Speed (RPM)

The mechanical power (W) as a function of turbine rotational speed (RPM) for all wind speeds has been determined. The plot for 5.5 m/s wind speed for all prototype turbines are shown in Figure 4.1. The maximum power outputs for 8, 16, 24, 32, 40 and 48 blades turbine are 0.0261, 0.0864, 0.490, 0.6120, 0.3900 and 0.1776 watt, (W) respectively. The 32 blades turbine produces maximum power (over 23 times more) compared to 8 blades turbine. The maximum power for 8 blades turbine occurs at 30 rpm while 32 blades turbine at 120 rpm. At other speed range, the 32 blades turbine produces higher power consistently. The aerodynamic study using flow visualisation (wool tuff) in section 4.1.5.5, describes in detail the effect of blade number and power.

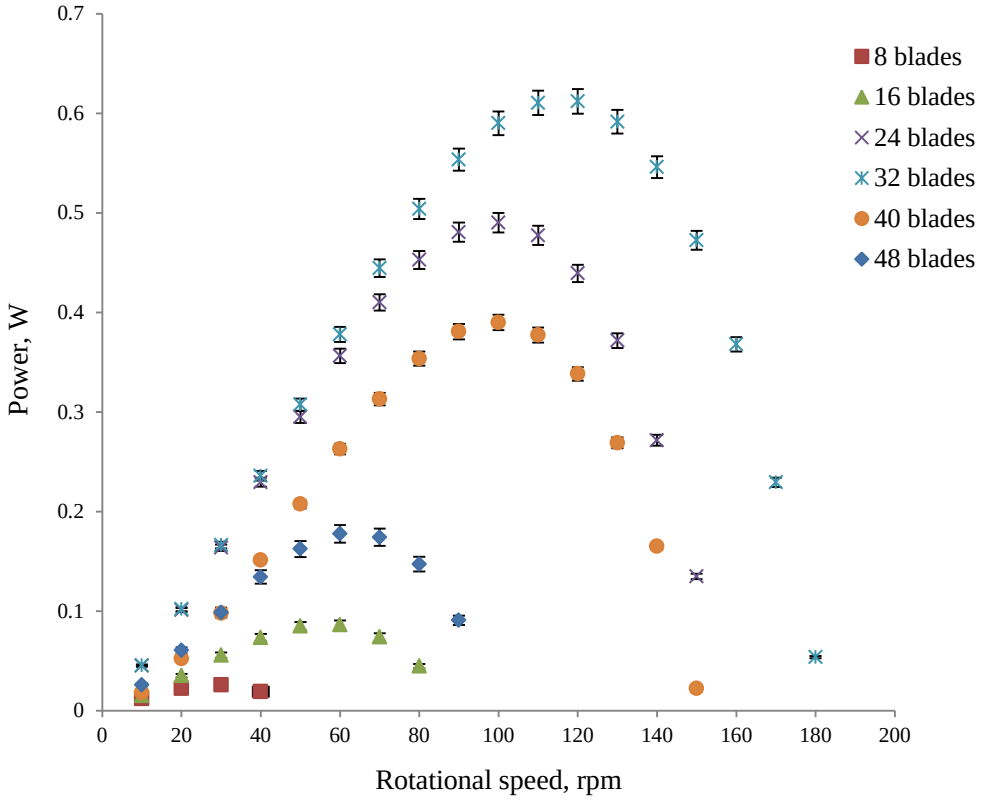

Figure 4.1: Power as a function of rotational speed at 5.5 m/s for all configurations

As shown in Section 4.1.5.5, the interaction between the captured wind flowing through the gap between the blades and the rotating flow at the rear blades affect the performance of the turbines. The interaction of these flows requires huge power for the turbine to maintain its

rotational speed. The thirty two blades turbine has the least flow interaction between the captured flow and the rotating flow at the rear blades thus whatever power extracted by the oncoming flow at the blade inlet is used to maintain its rotational speed whereas for the other blade configurations, the power extracted by oncoming flow at the blade inlet is spent by the rear blades to overcome the two flow interactions resulting in lower rotational speed.

4.1.1.2 Turbine Power and Tip Speed Ratio

The power coefficients and tip speed ratios for all turbine configurations have been determined at all wind speeds. The power coefficient versus tip speed ratio for all prototype turbines at 5.5 m/s is shown in Figure 4.2. The power coefficient increases with the increase of tip speed ratio (λ) until the peak level is obtained and then it decreases; and finally becomes zero as the turbine attains its constant maximum rotational speed. The maximum power coefficient of 0.13 is obtained by the 32 blades turbine at λ=0.34 as shown in Figure 4.4. Hau (2005) reported that a drag based single stage vertical axis wind turbine can have the maximum theoretical power coefficient of around 0.20.

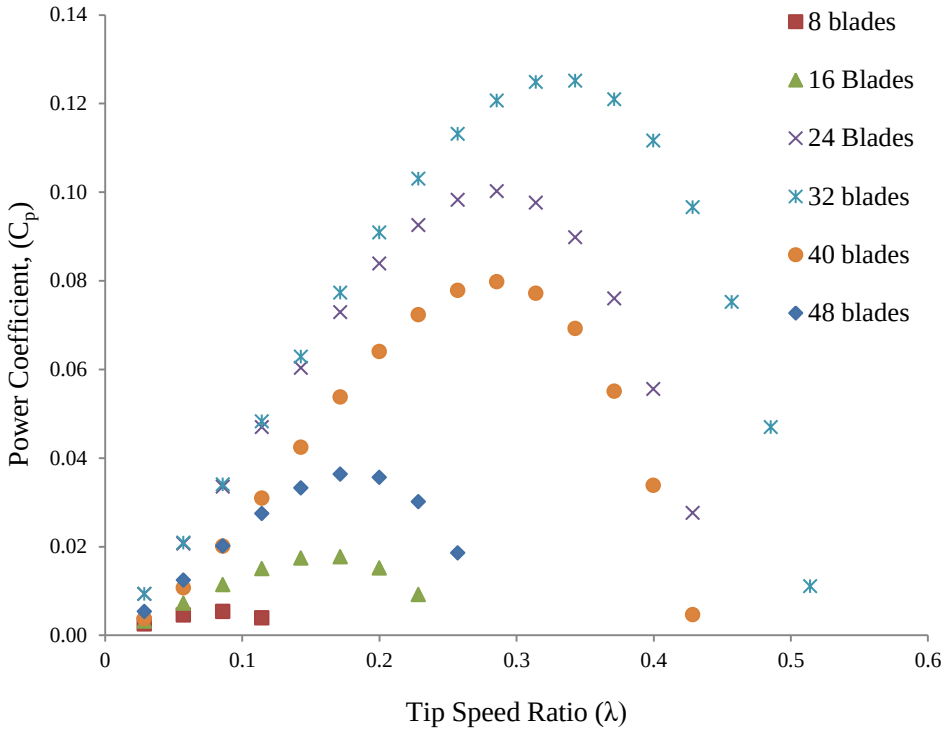

Figure 4.2: Power coefficient as a function of tip speed ratio and blade number at 5.5m/s

4.1.1.3 Turbine Torque Coefficient and Tip Speed Ratio

The torque coefficient variation with tip speed ratio for all configurations is shown in Figure 4.3. The torque coefficients achieved at 5.5 m/s wind speed are 0.100 at λ=0.029, 0.132 at λ=0.086, 0.385 at λ=0.143, 0.447 at λ=0.143, 0.58 at λ=0.143, and 0.265 at λ=0.114 for 8 blades, 16 blades, 24 blades, 32 blades, 40 blades and 48 blades configurations respectively. It is interesting to note that variable torque coefficients were obtained at approximately the same tip ratio for 24, 32 and 40 blades wind turbines. The highest torque coefficient is obtained for the 32 blades turbine. The lowest torque coefficient is obtained from the 8 blades configuration. In short, based on torque coefficient values, the ranking is: highest 32 blades turbine followed by the 24, 40, 48, 16 and 8 blades turbine. The 32 blades turbine is expected to perform well at lower wind speeds (<4.5 m/s).

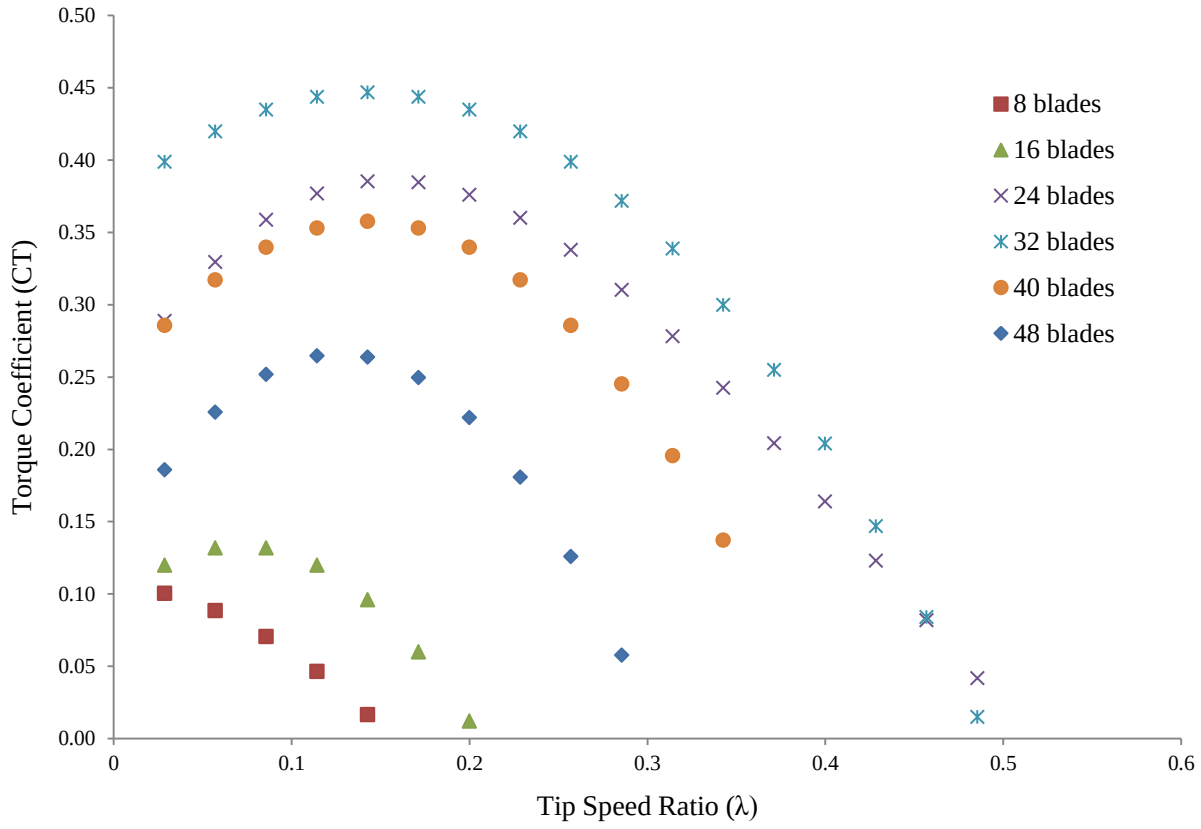

Figure 4.3: Torque coefficient versus tip speed ratio of turbines

4.1.1.4 Turbine Maximum Torque and Blade Number

The maximum torque variation as a function of blade number at 4.5 to 8.5 m/s wind speeds is shown in Figure 4.4. The maximum torque achieved at 8.5 m/s wind speed are 0.023 Nm, 0.044 Nm, 0.079 Nm, 0.096 Nm, 0.072 Nm and 0.055 Nm for 8 blades, 16 blades, 24 blades, 32 blades, 40 blades and 48 blades configurations respectively. The maximum torque for the 32 blades turbine increases by about 4 times compared to the 8 blades turbine (the least torque producing turbine) at 8.5 m/s. The 16 and 24-blade turbines increase by nearly 2 times and 3.5 times respectively when compared with the 8-blade turbine. However, the maximum torque for the 40-blade and 48-blade turbines decreases by about 1.5 times and 2 times compared to the 32-blade turbine. The aerodynamic study using flow visualisation (wool tuff) in section 4.1.5.5, describes in detail the effect of blade number and rotational speed.

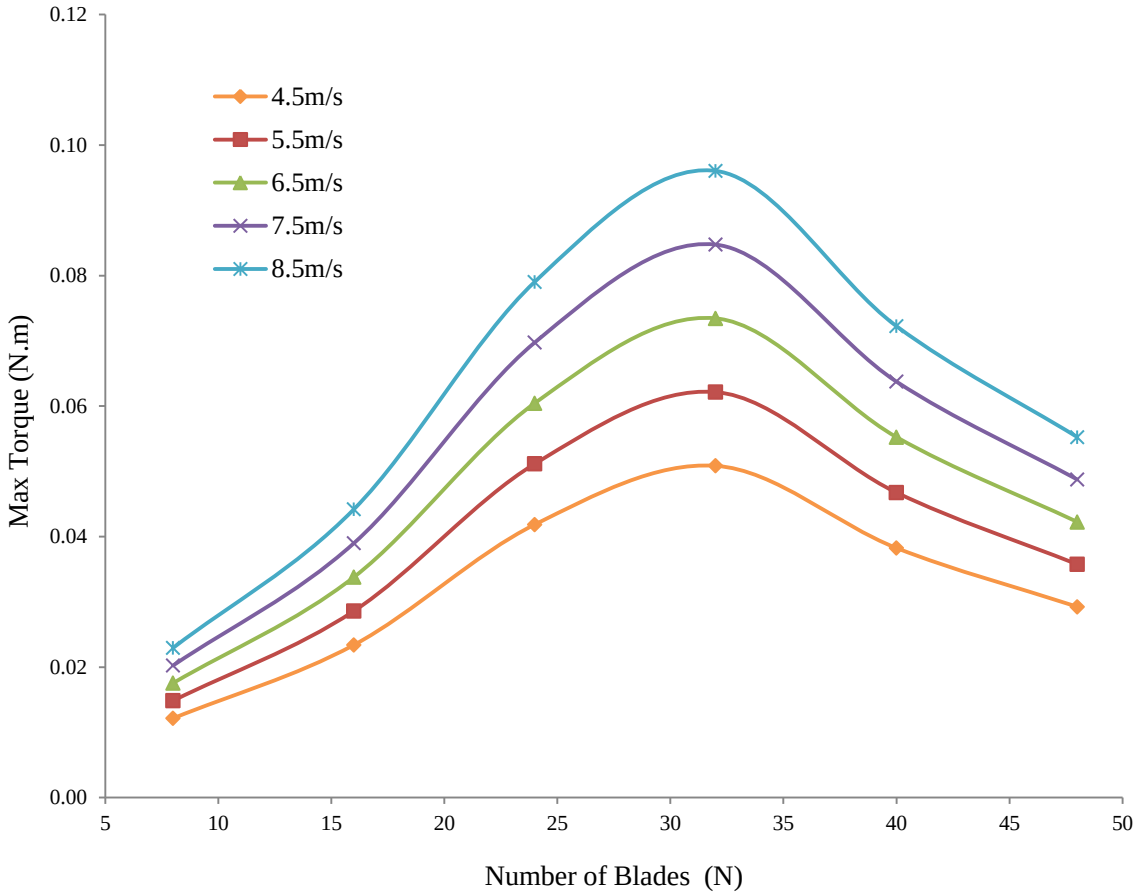

Figure 4.4: Maximum torque versus blade number

4.1.1.5 Turbine Maximum Torque and Wind Speeds

The variation of maximum torque with the respect to the wind speeds is illustrated in Figure 4.5. It is noted that the maximum torque increases with the increase of wind speeds for all configurations. The maximum torque increases linearly for all blades configurations from 4.5 m/s to 8.5 m/s. The 32 blades (most efficient) turbine maximum torque at 4.5 m/s and 8.5 m/s is 0.051 N.m and 0.096 N.m respectively. That is an increase of 90%. It should be noted that similar trend was observed for the 8, 16, 24, 40 and 48 blades turbine. The maximum torque increases by 91.3%, 92.2%, 88.2%, 90.1% and 90.5% respectively for the 8, 16, 24, 40 and 48 blades respectively. It is interesting to note that the average maximum torque for all turbine configurations at 8.5 m/s is 0.062 N.m. However, the average maximum torque for all turbine configurations at 4.5 m/s is 0.033 N.m. It is a decrease of 89%. It can be concluded that increasing the blade number, increases the maximum torque output by 90 %. The most efficient turbine is the 32 blades turbine. Increasing the blade number beyond 32 blades does not have a positive effect on the maximum torque output.

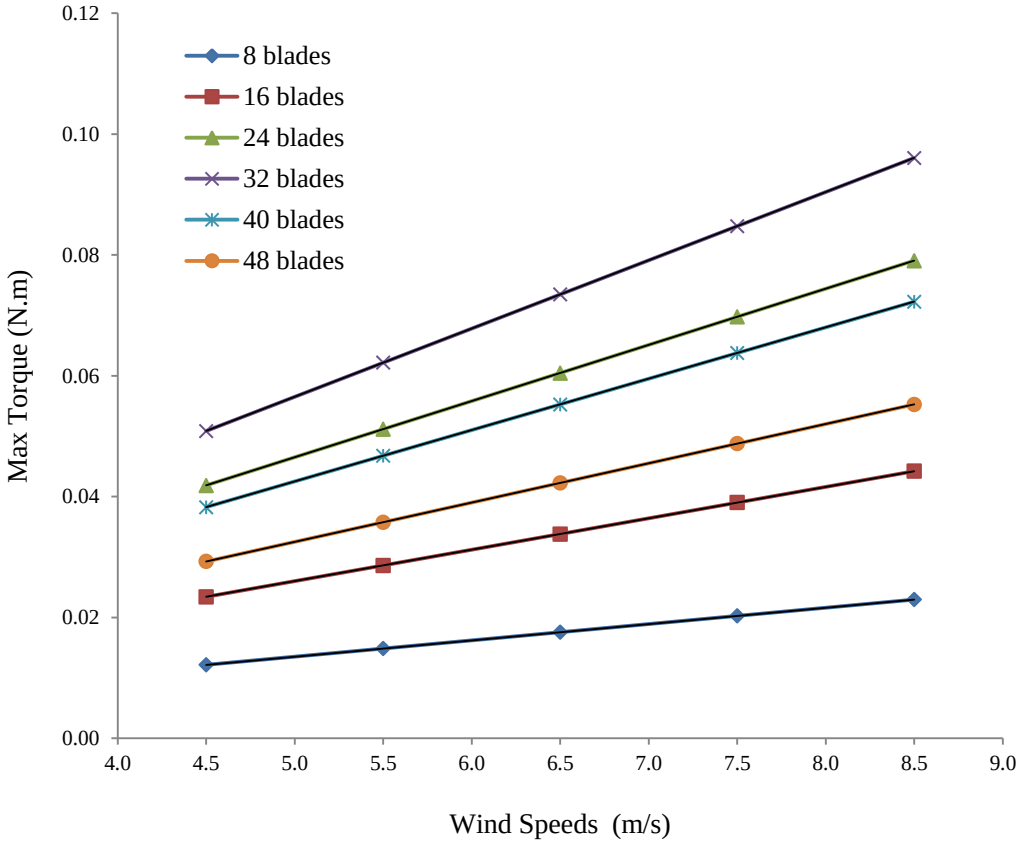

Figure 4.5: Maximum torque versus wind speeds

4.1.2 Effect of Scale on Torque

The single stage multi-blade drag-based VAWT used for this study is a semicircle shaped blade made from PVC material. Detailed dimensions of the blade are shown in Section 3.3.5.

4.1.2.1 Power and Wind Speeds

The mechanical power (W) as a function of wind speeds has been determined by experiment. The variation of power between the base size and the double sized turbines with 8, 16 and 24 blades at 4.5 to 8.5 m/s wind speeds is shown in Figure 4.6. The maximum power outputs for 8, 16, and 24 blades base turbine are 0.1959, 0.4518 and 1.3458 watt (W) respectively. The maximum power outputs for the corresponding double sized models are 1.1216, 2.3092 and 4.3418 watt (W) respectively. It can be observed that the average power increased by around 5.5 times when comparing the base model with scaled up models (double sized). The data also shows that the power increases with the increase of blade number for both the base and the double sized models. It can be said that the models are scalable. As the dimensions of the blade and the turbine are doubled, the area of the blades and the turbine also increased by double the size, however, the power output does not increase proportionally.

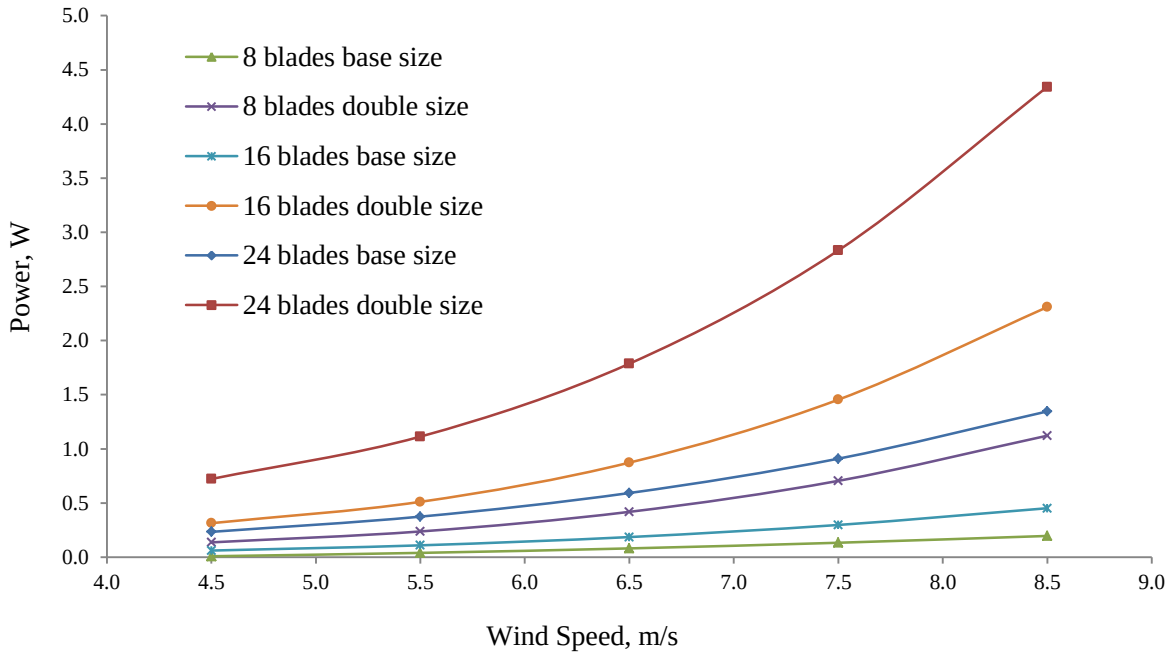

Figure 4.6: Power as a function of wind speeds

4.1.2.2 Power and RPM

The mechanical power (W) as a function of rotational speed (ω) for 5.5 m/s wind speed have been plotted. The variation of RPM between the base size and the double sized turbines with 8, 16 and 24 blades at 5.5 m/s wind speeds is shown in Figure 4.7. The maximum RPM for 8, 16, and 24 blades base turbine were obtained at 50, 60 and 120 RPM respectively. The maximum RPM for the corresponding blade number double sized models are 35, 40 and 60 RPM respectively. It is interesting to note that while the power increases with the increase of blade number for both for the base and the double sized models, the average RPM decreased by around 40% when comparing the base model with the scaled up models (double sized). As the dimensions of the blade and the turbine are doubled, the area of the blades also increased by double the size, however, the RPM does not increase proportionally.

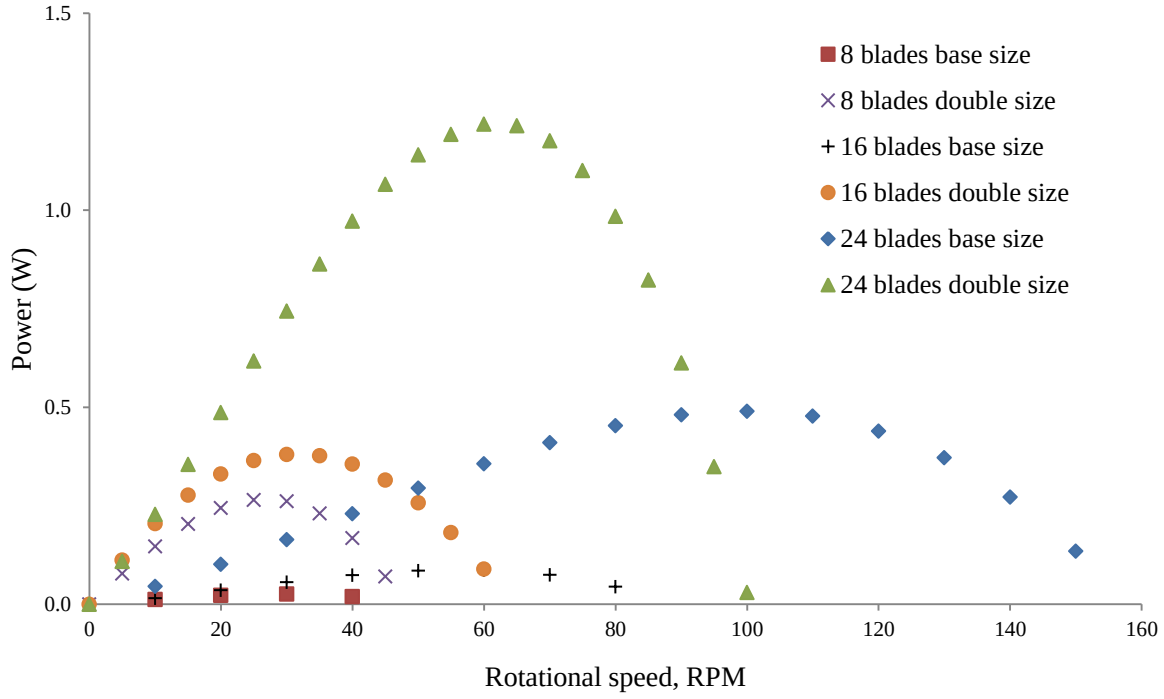

Figure 4.7: Power as a function of RPM

4.1.3 Effect of Blade Radii on Turbine Power Output

To determine the effect of blade radius on the power output, three sets of 8 blades turbine was constructed by keeping the turbine diameter (300 mm) and blade length (160 mm) constant but varying the blade diameter (20 mm, 40 mm and 80 mm) respectively. Section 3.3.6 shows the detailed dimensions of three sets of 8 blades.

4.1.3.1 Power and Wind Speeds

The variation of power with turbine speeds for 3 different blade diameters (20, 40 and 80 mm) is shown in Figure 4.8. The maximum power outputs for the 20, 40 and 80 mm blades at 8.5 m/s wind speeds are 0.3888, 0.8691 and 1.4652 watt (W) respectively. It is found that the power increased by around 2 times when the blade diameter was scaled up. It can be said that the models are scalable. Doubling the blade diameter increased the amount of wind energy that the blades were able to capture. However, it was observed that the power output does not increase proportionally. It is interesting to note that the turbine at 8.5 m/s wind speed produces an average of three times more power compared to turbine at 4.5 m/s wind speed for all three prototypes. This is expected as wind speeds have a cubic effect on the turbine power output. The power (Watt) available from the moving air is equal to half times the product of density of air, (kgm^{-3}), the turbines cross section area A (m^2) and the cube of wind speed, V (ms^{-1}):

$$P_{wind}(W) = \frac{1}{2} \cdot \rho \cdot A \cdot V^3 \qquad 4.1$$

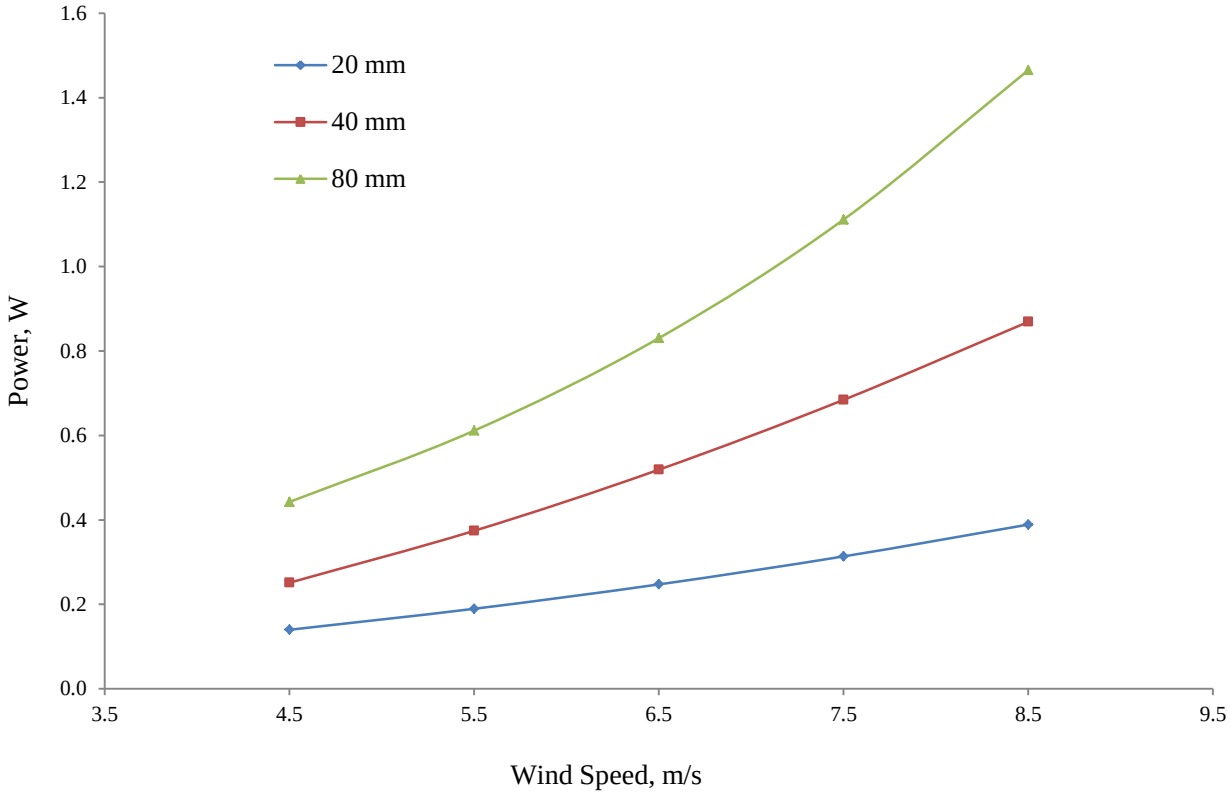

Figure 4.8: Power as a function of wind speed

4.1.3.2 Power and RPM

The variation of power as a function of RPM for 3 different blade diameters (20, 40 and 80 mm) from 4.5 to 8.5 m/s wind speeds is shown in Figure 4.9. The maximum power output for 20, 40 and 80 mm blade diameter turbines are 0.400, 0.792 and 1.763 watt (W) respectively. The 80 mm diameter blade turbine produces the highest power compared to the other two blade diameters. The power generated by the 80 mm blade diameter turbine has increased by 340% compared to the 20 mm blade diameter turbine (the minimum power producing turbine). The RPM at 5.5 m/s wind speed for the 20 mm, 40 mm and 80 mm are 30 rpm, 60 rpm and 135 rpm respectively. It is noted that the average RPM increases by an average of 110% when the models were scaled up. The data shows a linier relationship between the power and RPM for the three sets of configuration.

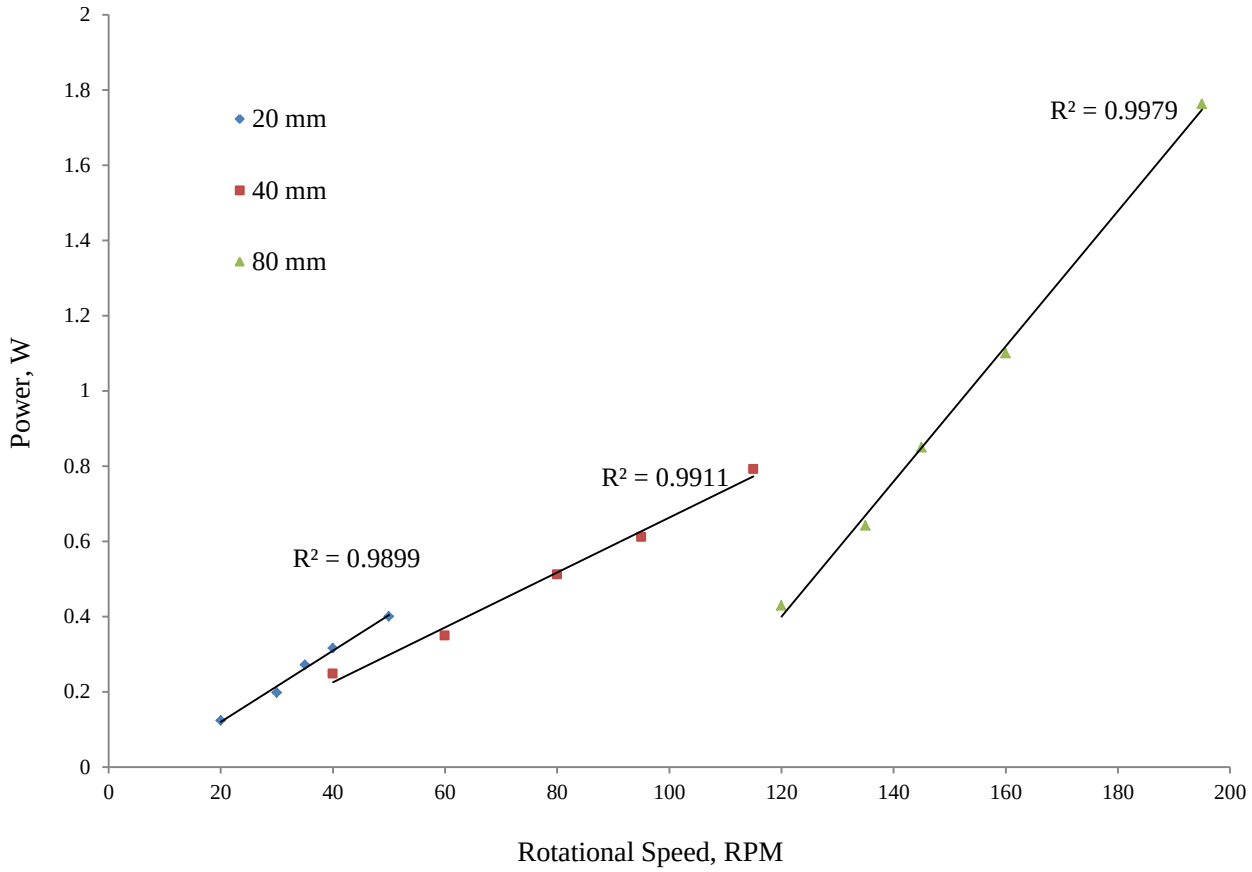

Figure 4.9: Power as a function of turbine rotational speed, RPM

4.1.3.3 Tip Speed Ratio (λ) and Coefficient of Performance (Cp)

Average Tip Speed Ratio (λ) as a function of average Coefficient of Performance (Cp) for the 20, 40 and 80 mm blade diameter is shown in Figure 4.10. The average power coefficient (Cp) are 0.031 at λ = 0.081, 0.071 at λ = 0.201 and 0.129 at λ = 0.374 for 20 mm, 40 mm and 80 mm blade diameter turbines respectively. The 80 mm blade diameter turbine possesses the highest power coefficient (0.129). The lowest power coefficient (0.031) is obtained for the 20 mm blade diameter turbine. It is noted that a positive linear correlation is found between TSR and Cp.

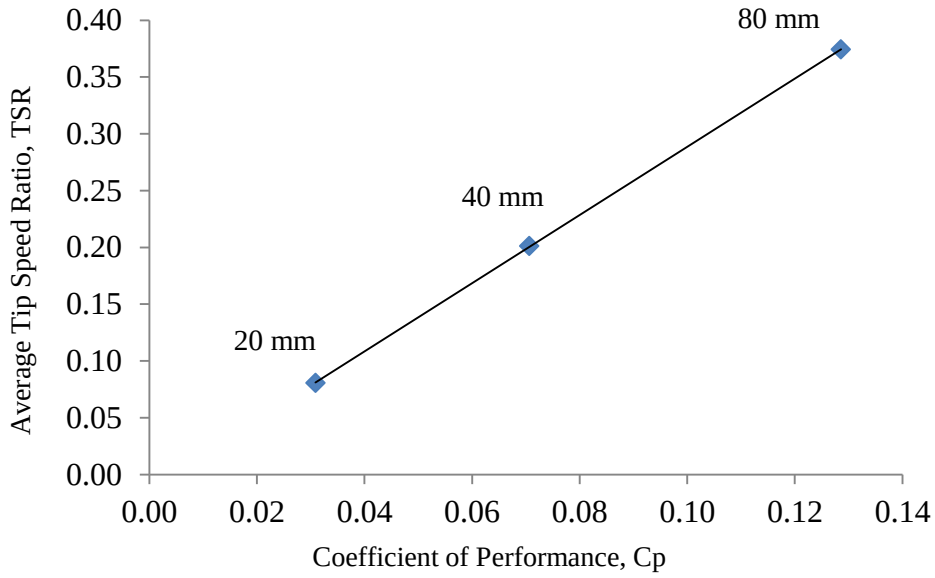

Figure 4.10: Average tip speed ratio, TSR as a function of coefficient of performance, Cp

The power coefficient, C_p is a quantity that expresses what fraction of the power in the wind is being extracted by the wind turbine. Tip speed ratio, (TSR) is the ratio between the tangential speed of the tip of the blade and the actual speed of the wind, V. The tip-speed ratio is related to the efficiency. The tip speed of the blade can be calculated by rotational speed, ω (rads$^{-1)}$ times turbine radius, R (m):

$$\lambda = \frac{\text{Tip speed of the blade}}{Wind\ speed} \tag{4.2}$$

$$\lambda = \frac{\omega R}{V} \tag{4.3}$$

It is generally assumed to be a function of both tip speed ratio and pitch angle. Ideally, most efficient turbines operate at maximum value of C_p at all wind speeds. The 80 mm blade diameter clearly is the most efficient turbine compared to the 20 mm and 40 mm blade diameters as shown in Figure 4.10.

4.1.4 Effect of Turbulence on Turbine Power Output

Three different grids were used in the wind tunnel to generate turbulence (detailed grid dimensions are given in section 3.3.7). Turbulence intensity as a function of distance from the grid position for the small, medium and large grids is shown in Figure 4.11. The generated turbulence for each grid has been measured at constant wind speed of 8.5 m/s. The percentage drop of intensity at 4500 mm from the grid (turbine position) for the small, medium and large grid was found to be 64%, 46% and 27% respectively. The turbulence intensity generated by the small grid experienced a large drop about 75% at 6000 mm from the grid position before it starts to become steady. The small and medium grids turbulence intensity becomes steady at around 7500 mm from the grid. However the large grid turbulence intensity remains turbulent. It was observed that the turbulence intensity increases with the increase of grid size. It was noted that the large grid had a higher impact on the turbulence intensity compared to the small and medium grids.

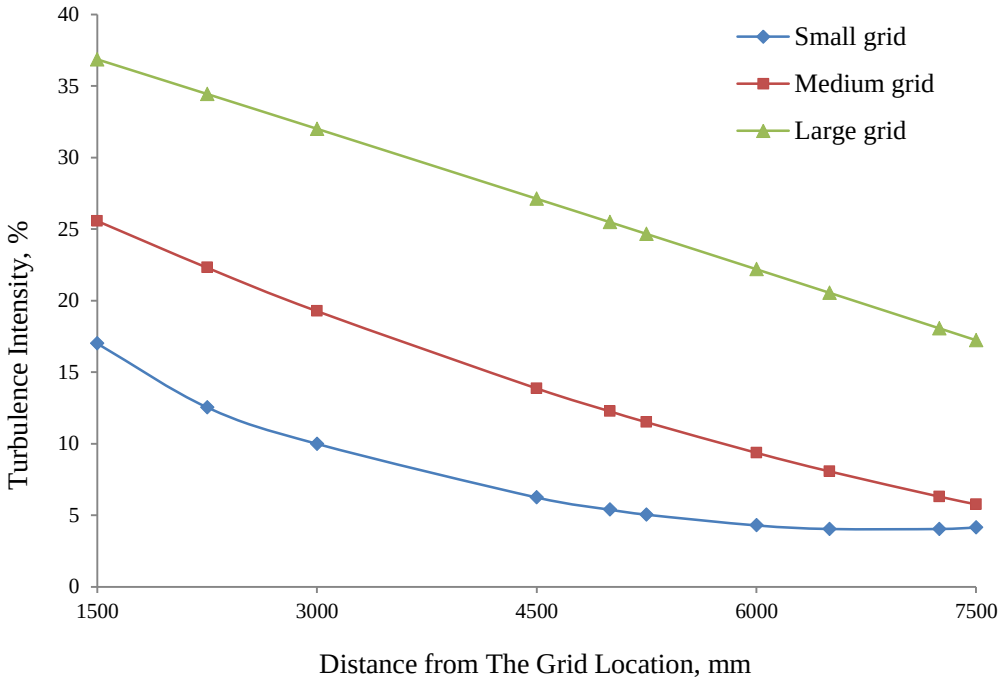

Figure 4.11: Turbulence intensity as a function of distance from the grid at a constant speed (8.5 m/s)

4.1.4.1 Effect of Grid Size on Turbulence Intensity and Power

The variation of power with intensity for 24, 32 and 48 blades turbines using small, medium and large grids is shown in Figures 4.12, 4.13 and 4.14. The velocity at the turbine inlet (4500mm in front of grid) was measured at 8.5 m/s for all 3 grids. The maximum power output for the 24, 32 and 48 blades turbines without grid (1.8% intensity) are 1.5, 1.96 and 1.4 watt (W) respectively. The power output drastically decreases as the turbulence intensity increases from 1.8% to 4.5% due to unsteady vortices interacting with each other causing decreases in the drag force.

The maximum power drop for all three turbines is observed at 7% turbulence intensity after which the turbulence intensity had no effect on the power output. The power generated at 7% turbulence intensity is 0.74, 0.81 and 0.68 watt (W) respectively. The average power decreased around 51%, 59% and 51% respectively after which the power loss was less drastic. It should be noted that the turbulence intensity had a larger impact on 32 blades turbine compared to the 24 and 40 blades turbines. The 32 blades turbine which is the most efficient turbine experienced a 40% drop in power at 4.5% turbulence intensity compared to around 33% and 34% for the 24 and 40 blades turbines respectively. However, the 32-bladed turbine still outperformed the other configurations consistently. It can be clearly seen that, turbulence has a negative impact on the turbines.

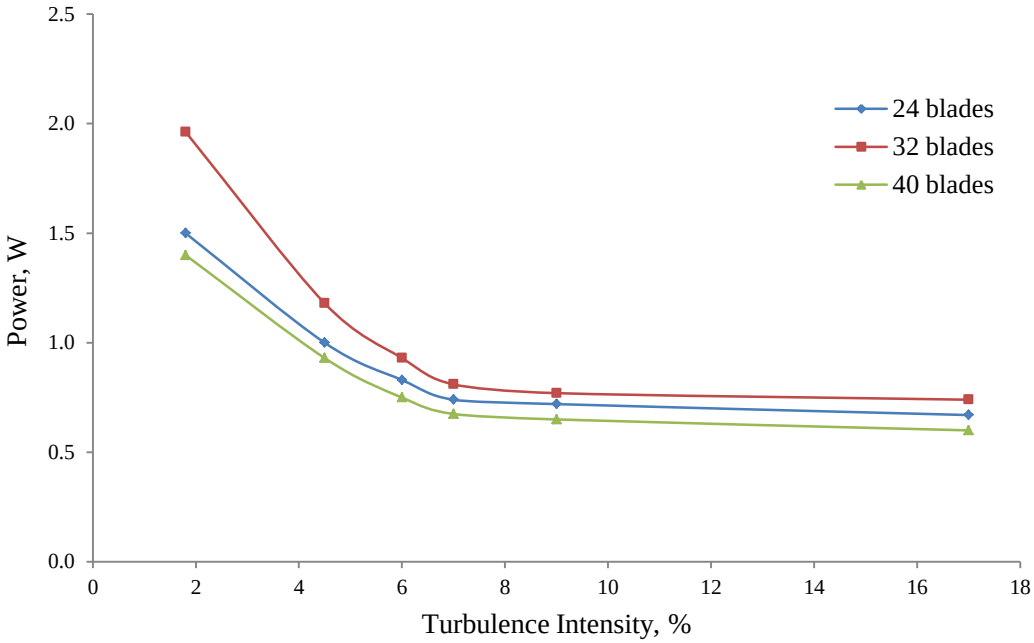

Figure 4.12: Power as a function of turbulence intensity small grid

The maximum power output as a function of turbulence intensity at 8.5 m/s wind speed for the medium grid is shown in Figure 4.13. The power output drastically decreases as the turbulence intensity increases from 1.8% to 8% due to unsteady vortices interacting with each other causing decreases in the drag force. The maximum decrease in power output for the 24, 32 and 40 blades turbine was at 12% turbulence intensity. The maximum power output is 1.28, 1.38 and 1.20 watts (W) respectively. It is a decrease of 15%, 30% and 14% respectively compared to the power output at 1.8% turbulence intensity (without grid).

It can be observed that the turbulence has a significant impact on the power output of the 32 blades turbine compared to the 24 and 48 blades turbine similar to the small grid. The medium grid had a lesser impact on the power output compared to the smaller grid.

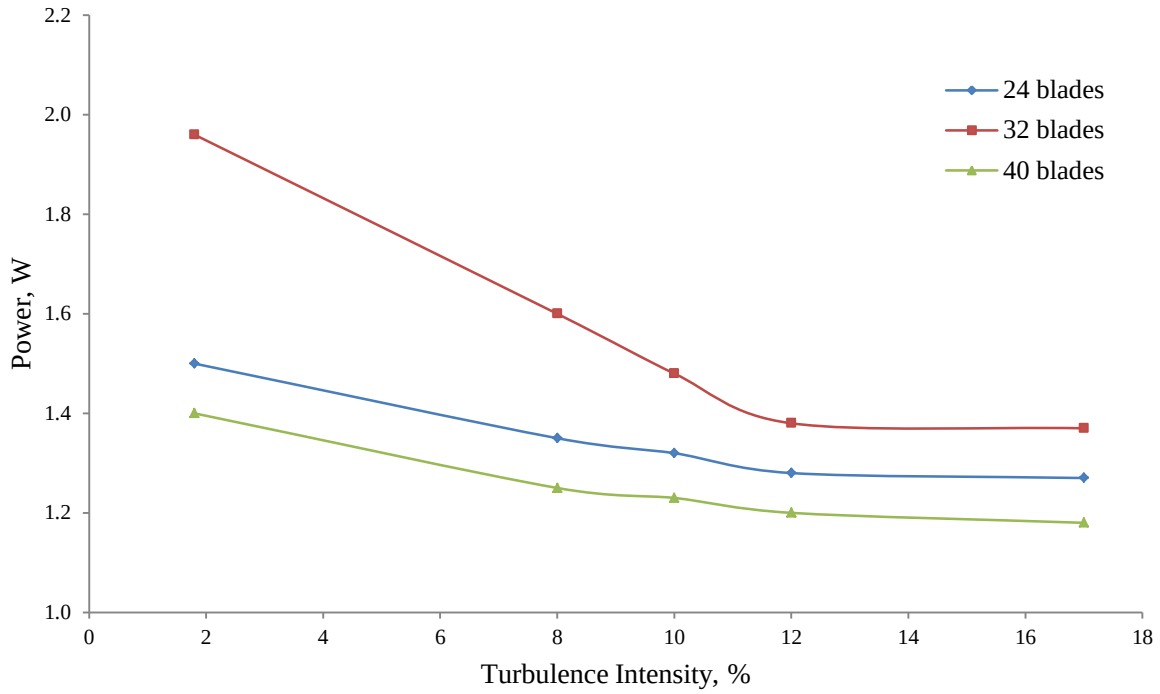

Figure 4.13: Power as a function of turbulence intensity medium grid

The maximum power output as a function of turbulence intensity at 8.5 m/s wind speed for the large grid is shown in Figure 4.14. The power at 17% turbulence intensity was found to be 1.35, 1.5 and 1.26 watt (W) respectively. The power decreased by only 15%, 23% and 10% respectively when comparing the power at 1.8% turbulence intensity (no grid). It can be noted that large grid has less impact on the power output compared to the small grid and medium grids.

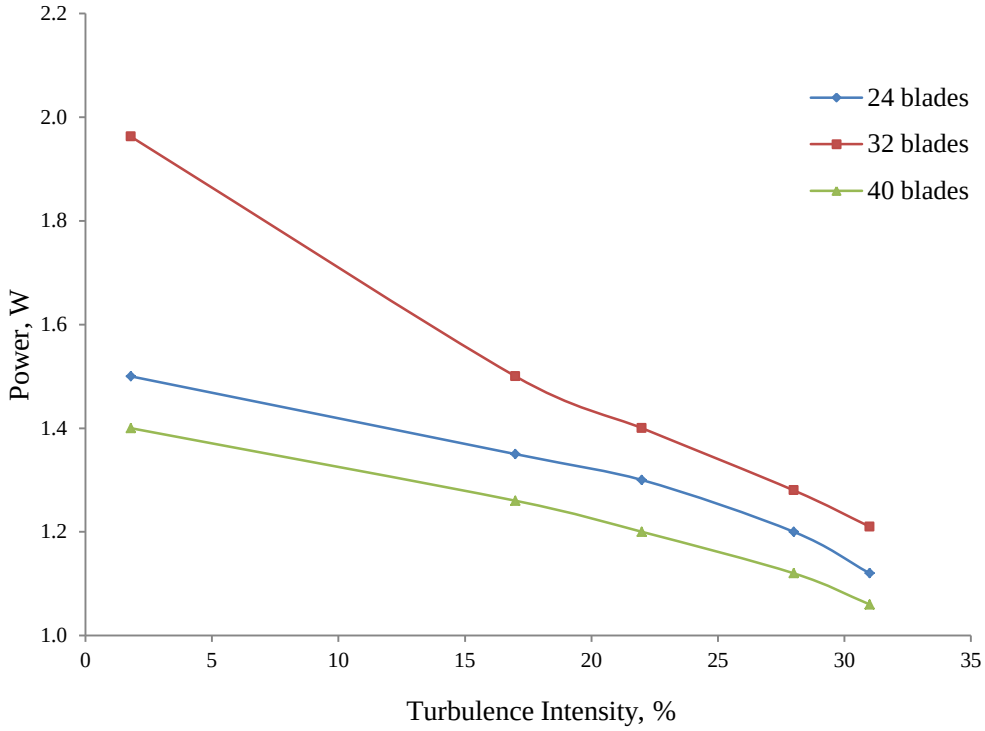

Figure 4.14: Power as a function of turbulence intensity large grid

It is evident that turbulence has a negative impact on the power output of a single stage multi-blade drag-based VAWT. The power and turbulence intensity analysis have revealed that turbulence decreases the power output by around 25% to 60%. It is also interesting to note that when comparing the small grid and the large grid, the power drop experienced by the turbine placed in front of the small grid was higher at 17% compared to the large grid at 30% turbulence intensity. It was also observed that the turbine placed (4500 mm) from the small grid experienced the largest drop in power compared to the medium and large grids at similar (17%) turbulence intensity. As illustrated in Section 3.3.7, the air passing through the grids becomes more constricted as the cross sectional area decreases. The pressure drop is higher when using the smaller grid; hence the air that is available for the turbine has less energy, resulting in lower power outputs. It can be concluded that the volume flow rate has a higher impact than turbulence intensity on the power output of a single stage multi-blade drag-based vertical axis wind turbine. High wind locations and low wake losses are critical for efficient power generation.

4.1.5 Effect of Cowling on Turbine Power Output

The main function of the cowling is to eliminate the negative torques which prevents the turbine from accelerating to higher torque producing speeds. To ditermine the effect of cowling device on the performance of the wind turbine, a cowling was designed in such a way that it can enclose the turbine turbine with a small clearance and can guide the incoming wind through a defined inlet and push the turbine and finally channel out the wind through the confined outlet to the environment (detailed dimensions of cowling are given in section 3.3.4).

4.1.5.1 Power and RPM

The mechanical power (W) as a function of rotational speed (ω) for all wind speeds have been plotted as shown in Figure 4.15. The maximum power outputs for 8, 16, 24 and 32 blades turbine are 0.176, 0.187, 0.36 and 0.30 watt, (W) respectively. The 24 blades turbine produces maximum power (around 100% more) compared to 8 blades turbine. The maximum power for 8 blades turbine occurs at 80 rpm while 24 blades turbine at 100 rpm. At other speed range, the 24 blades turbine produces higher power consistently.

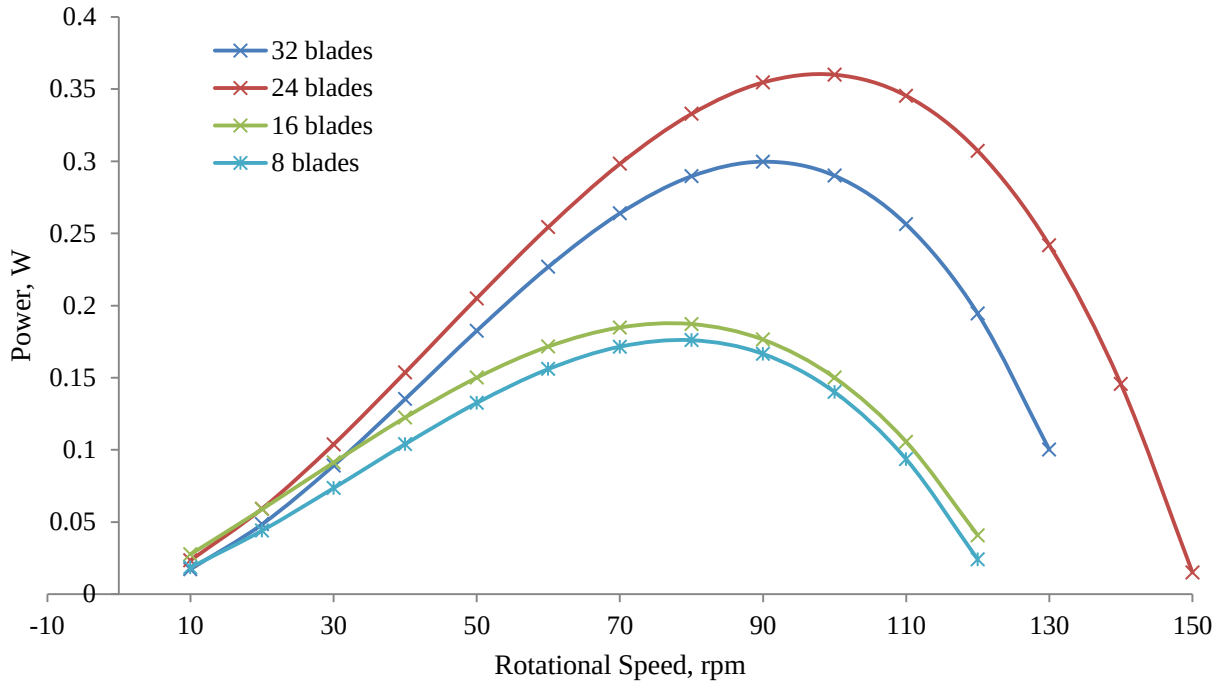

Figure 4.15: Power as a function of RPM at 5.5m/s

4.1.5.2 Power and Tip Speed Ratio

The power coefficients and tip speed ratios for all turbine configurations have been determined at all wind speeds. The power coefficient versus tip speed ratio for all prototype turbines at 5.5 m/s is shown in Figure 4.16. The power coefficient increases with the increase of tip speed ratio (λ) until the peak level is obtained and then it decreases; and finally becomes zero as the turbine attains its constant maximum rotational speed. The maximum power coefficient of 0.15 is obtained by the 24 blades turbine at λ=0.3 as shown in Figure 4.16. Hau (2005) reported that a drag based single stage vertical axis wind turbine can have the maximum theoretical power coefficient of around 0.20.

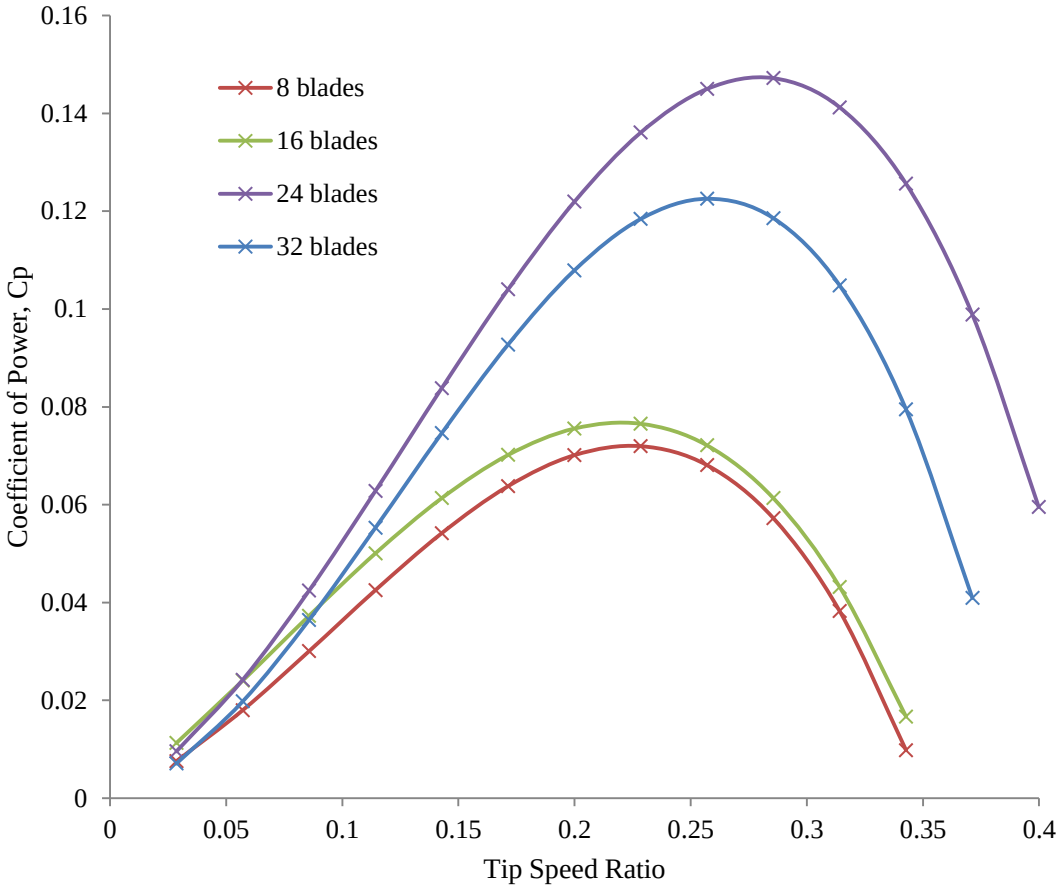

Figure 4.16: Power coefficient versus tip speed ratio for various blade numbers at 5.5m/s wind speed

4.1.5.3 Torque and Blade Number

The maximum torque variation as a function of blade number at 4.5 to 8.5 m/s wind speeds is shown in Figure 4.17. The maximum torque achieved at 8.5 m/s wind speed are 0.054 Nm, 0.060 Nm, 0.080 Nm and 0.074 Nm for 8 blades, 16 blades, 24 blades, and 32 blades configurations respectively. The maximum torque for the 24 blades turbine increases by about 1.5 times compared to the 8 blades turbine (the least torque producing turbine) at 8.5 m/s. The 16 and 24-blade turbines increase by nearly 1.1 times and 1.3 times respectively when compared with the 8-blades turbine.

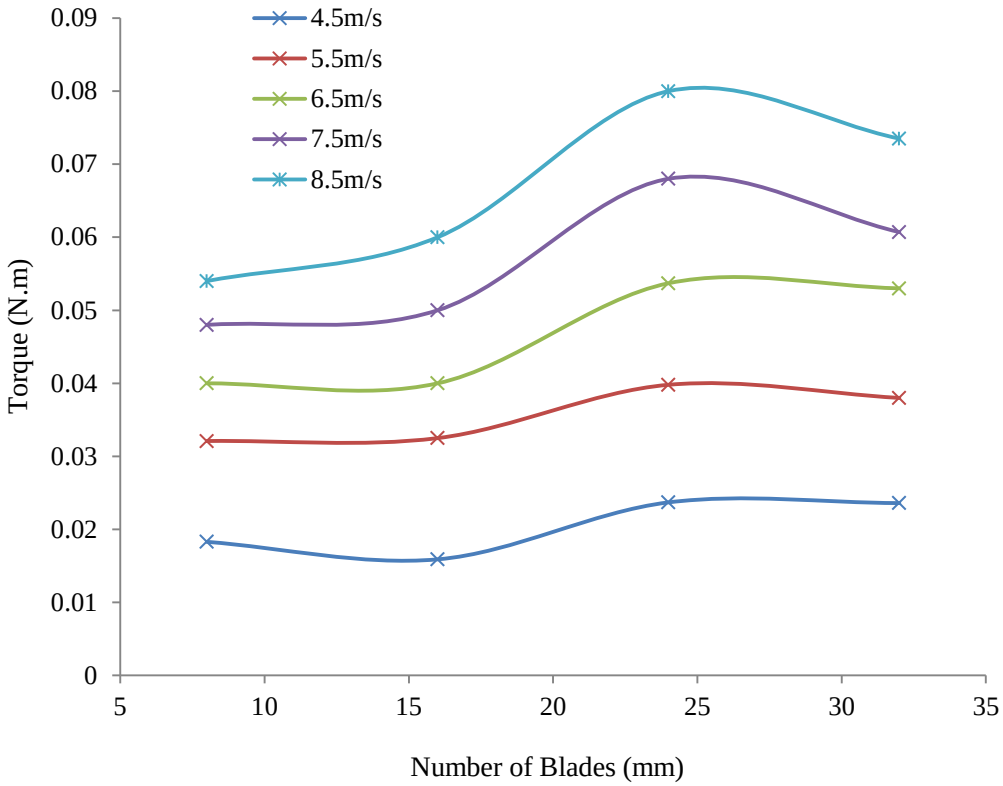

Figure 4.17: Torque as a function of blade number

4.1.5.4 Coefficient of Torque and Tip Speed Ratio

The torque coefficient variation with tip speed ratio for all configurations is shown in Figure 4.18. The torque coefficients achieved at 5.5 m/s wind speed are 0.45 at λ=0.2, 0.47 at λ=0.2, 0.585 at λ=0.2, and 0.60 at λ=0.2 for 8 blades, 16 blades, 24 blades and 32 blades configurations respectively. It is interesting to note that variable torque coefficients were obtained at approximately the same tip ratio for 8, 16, 24 and 32 blades wind turbines. The 24 and 32-bladed turbines have quiet similar torque coefficients. The lowest torque coefficient is obtained from the 8 blades configuration. Both the 24 and 32-bladed turbines are expected to perform well at lower wind speeds (<4.5 m/s).

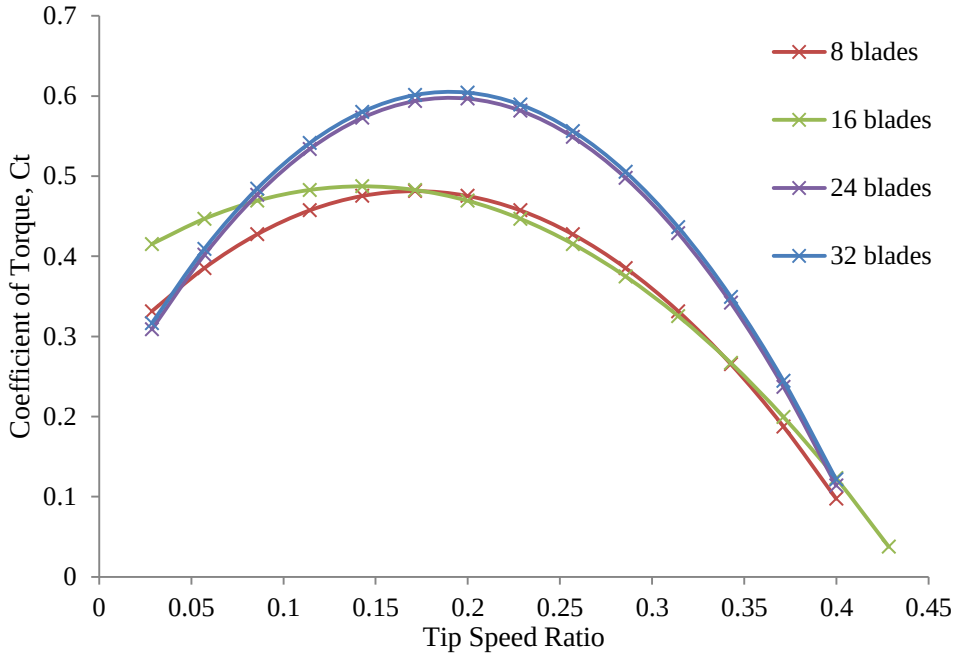

Figure 4.18: Torque coefficient versus tip speed ratio for various blade number at 5.5m/s wind speed

It is evident that the flow enhancing device (cowling) had shown a positive impact on the turbine RPM however, the overall torque and power was found to be lower compared to turbines without its employment. A comprehensive flow visualisation study in Section 4.1.5.5 using smoke was conducted to explain the interaction between the wind and blades and power produced.

4.1.5.5 Aerodynamic Study Using Flow Visualisation

It can be said that the spacing between two subsequent blades have an impact on the torque produced by single stage multi-blade drag-based vertical axis wind turbines. As the number of blades increases, the torque increases until it reaches an optimal spacing before the torque starts decreasing. The results showed that the 300 mm turbine with 32 blades configuration produces the highest power at all wind speeds (5.5 - 8.5 m/s) compared to the 8, 16, 24, 40 and 48 blades turbine. A schematic flow pattern around a 16 blades turbine and a 32 blades turbine in rotation is shown in Figure 4.19 and Figure 4.20.

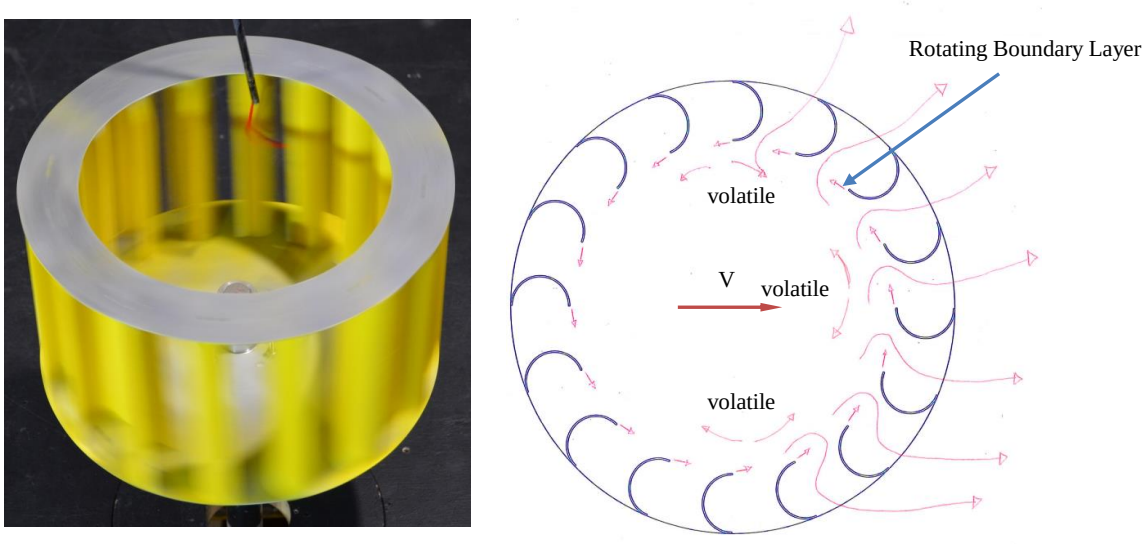

Figure 4.19: A schematic flow pattern around a 16 blades turbine in rotation

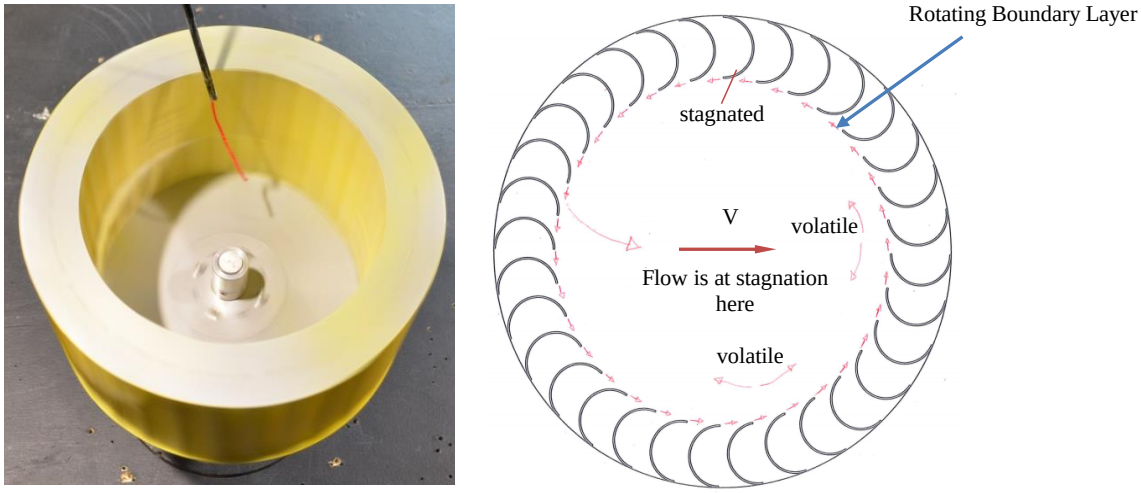

Figure 4.20: A schematic flow pattern around a 32 blades turbine in rotation

Torque is generated by the difference in net drag force between the concave and convex surface of the blades. When the free stream wind impacts the turbine effective area, the concave surface, captures the wind while the convex surface, moves against the wind. The coefficient of drag for the concave surface is two times higher than the convex surface. The difference in drag force on the concave and convex surfaces of the turbine produces a net torque which rotates the turbine clockwise. It should be noted that as the turbine is rotating in a clockwise direction, it is creating a counter-clockwise rotating boundary layer as shown in Figure 4.19 and 4.20. While observing the flow in the midpoint of the 16 blades turbine as shown in Figure 4.19, it can be seen that the flow is not stationary. This flow then interacts

with the turbine rotating boundary layer at the rear blades, creating aerodynamic resistance and subsequently slowing down the turbine rotational speed.

In contrast, while observing the 32 blades turbine as shown in Figure 4.19, it can be seen that flow is at stagnation in the middle of the turbine indicating only small amount of wind is allowed to pass through the turbine. This subsequently creates lesser flow interaction at the rear blades resulting in lower aerodynamic resistance.

It is interesting to note that the 16-bladed turbine front blades extract higher wind power compared to the 32-bladed turbine. Unfortunately, the power is spent by the rear blades to overcome the aerodynamic resistance resulting in lesser power left for torque. The 32-bladed turbine front blades on the other hand extracted lower wind energy compared to the 16-bladed turbine but lesser power is required to overcome the aerodynamic resistance at rear blades hence higher net power output compared to 16 blades.

It can be concluded that the optimal gap between the two subsequent blades allows for efficient interaction between the two flows (exiting wind and rotating boundary layer) allowing for efficient power generation.

CHAPTER 5

Validation of the Optimal Blade-Number Prediction Model

Significant challenge is associated with the determination of optimal blade number of a constant diameter single stage drag-based vertical axis wind turbine. Therefore, in this study, an empirical relation for determining the blade number of a constant diameter turbine which can generate maximum torque and power has been proposed. The predicted outcomes obtained through the developed relationship have been validated by undertaking experimental study in the wind tunnel environment. The experimental study has shown a good agreement with the predicted results.

5.1 Development of an Empirical Model for Optimal Blade Number

A prototype turbine with 300 mm diameter was initially designed and manufactured as shown in Section 3.1.1. A comprehensive aerodynamic study of behaviour of a single stage multi-blade drag-based VAWT was conducted and the results are shown in Chapter 4. A schematic of a multi-blade single stage drag-based vertical axis wind turbine includes following geometric features: turbine radius (R), blade number (N), blade radius (r), and clearance between two subsequent blades (c) is shown in Figure 5.1.

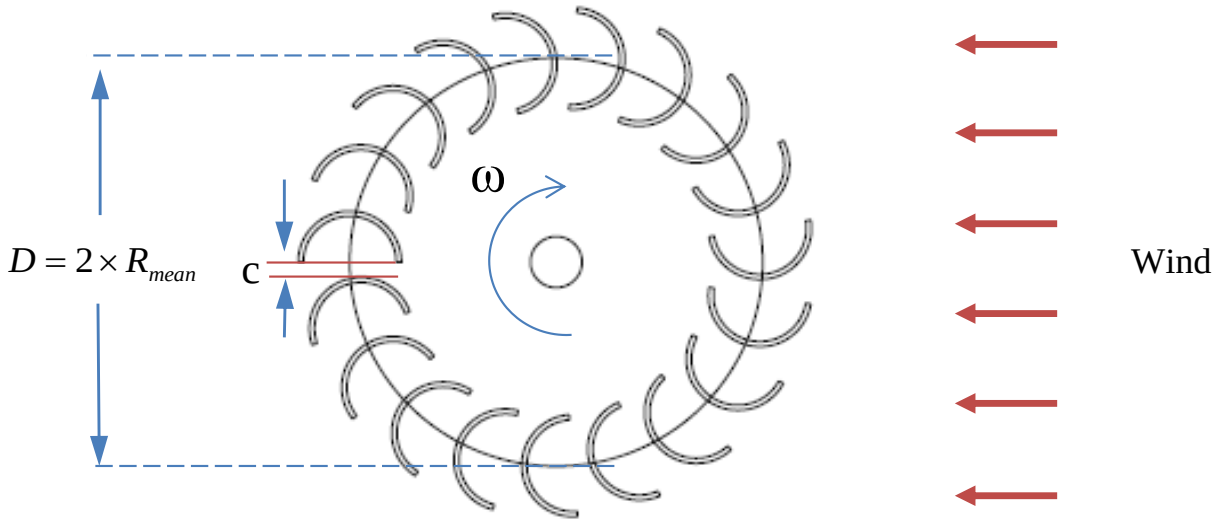

Figure 5.1: Top view of a multi-blade (19 blades) turbine

The 300 mm diameter turbine clearance ‘c’ between two subsequent blades for 8, 16, 24, 32, 40 and 48-blades turbine was initially measured as is shown in Table 5.1, third column. The experimental results showed that the 32-bladed turbine produced the maximum power at all wind speeds which corresponds to an optimal clearance (gap) of 5.4 mm

Table 5.1: Blade number and clearance between two subsequent blades for a 300 mm diameter turbine

Blade No. (N)	Predicted Clearance (c) by Equation (mm)	Measured Clearance (c) from Prototype (mm)	Clearance Error (%)
8	82.00	81.00	1.23
16	31.00	30.50	1.64
24	14.00	13.70	2.19
32	5.50	5.40	1.85
40	0.50	0.49	2.04
48	-3.00	- 2.95	1.69

Based on the experimental study on the geometric features of the 300 mm diameter turbine: turbine radius (R), blade number (N), blade radius (r), and clearance between two subsequent blades and its effect on the torque, RPM and power, an empirical relationship has been proposed as shown in Equation 5.1.

$$N = \frac{2\pi R}{r + c} \tag{5.1}$$

Where: N = Optimal blade number

R = Turbine mean (effective) radius

r = Blade radius

c = Clearance between 2 subsequent blades

The proposed equation can be utilised to determine the blade number of a constant diameter turbine which can generate maximum torque and power.

To verify this equation, a 200 mm diameter prototype turbine with 18, 19, 20 and 21 blades has been manufactured as shown in Section 3.4. The height, radius and thickness of the blade are kept the same as the 300 diameter prototype turbine. The top views of 18, 19 and 20 blades are shown in Figure 5.2. The top views of the 200 and 300 diameter prototype turbines are shown in Figures 5.3 (a) and 5.3 (b) respectively.

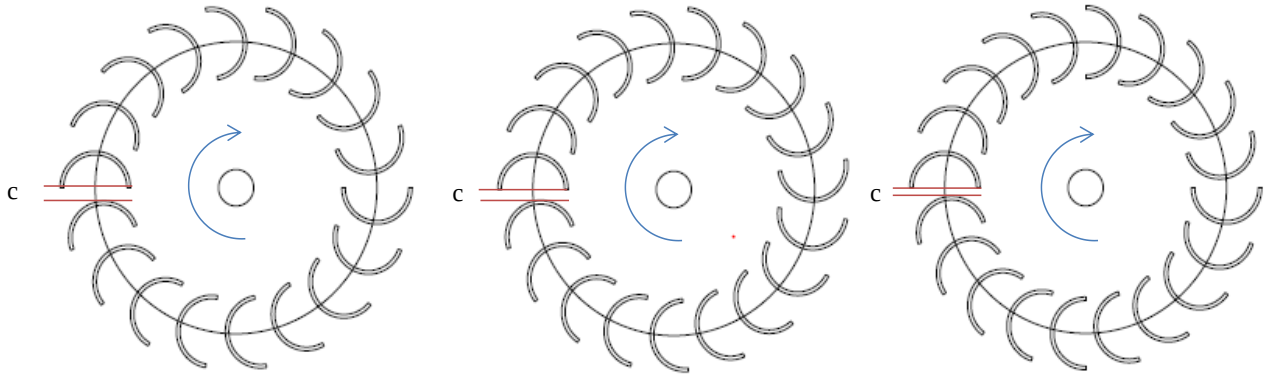

Figure 5.2: Top view of 18, 19 and 20 blades wind turbine with clearance between two subsequent blades ‘c’

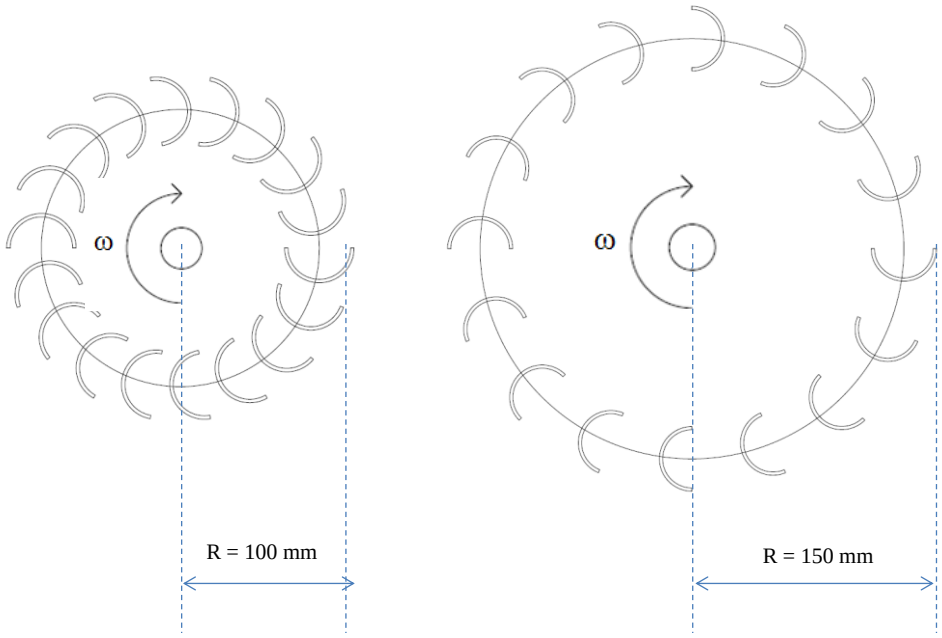

(a) 200 mm diameter (b) 300 mm diameter

Figure 5.3: Top View of a 200 mm and 300 mm diameter turbine prototype

The minimal clearance between two subsequent blades was obtained for 18, 19, 20 and 21 blades configurations using the proposed relationship (Equation 5.1). The data is shown in the second column of Table 5.2. The measured clearance from the prototype is shown in the third column. The average variation of clearance between predicted and measured is less than 2%. The variation increases with the decrease of gap due to measurement inaccuracy.

Table 5.2: Blade number and clearance between two subsequent blades for a 200 mm diameter turbine

Blade Number (N)	Predicted Clearance (c) by Equation (mm)	Measured Clearance (c) from Prototype (mm)	Clearance Error (%)
18	7.93	7.80	1.7
19	6.46	6.34	1.9
20	5.13	5.00	2.6
21	3.94	3.87	1.8

Using the developed empirical relationship (Equation 5.1), it was predicted that a 19 blades turbine configuration will provide the maximum power and torque at a given wind speed. To verify this prediction, as mentioned earlier, four prototype configurations (18, 19, 20 & 21 blades) were manufactured and investigated in the wind tunnel environment. The power as a function of rotational speed for 5.5 m/s wind speed (typically encounters in built-up areas) is shown in Figure 5.4. The maximum power outputs for 18, 19, 20 and 21 blades turbines are 0.296, 0.363, 0.265 and 0.231 watt (W) respectively.

The 19 blades turbine produces the highest power compared to other three turbines. The power generated by 19 blades turbine has increased by 57% when compared with the 21 blades turbine (the minimum power producing turbine). The results also show that the maximum power by 21 blades turbine occurs at 70 rpm while the rotational speed corresponding to maximum power output increases from 70 rpm to 90 rpm for the 19-blade turbine. The rotational speed increases by around 29%. At other wind speeds, the 19 blades turbine produces the highest power consistently.

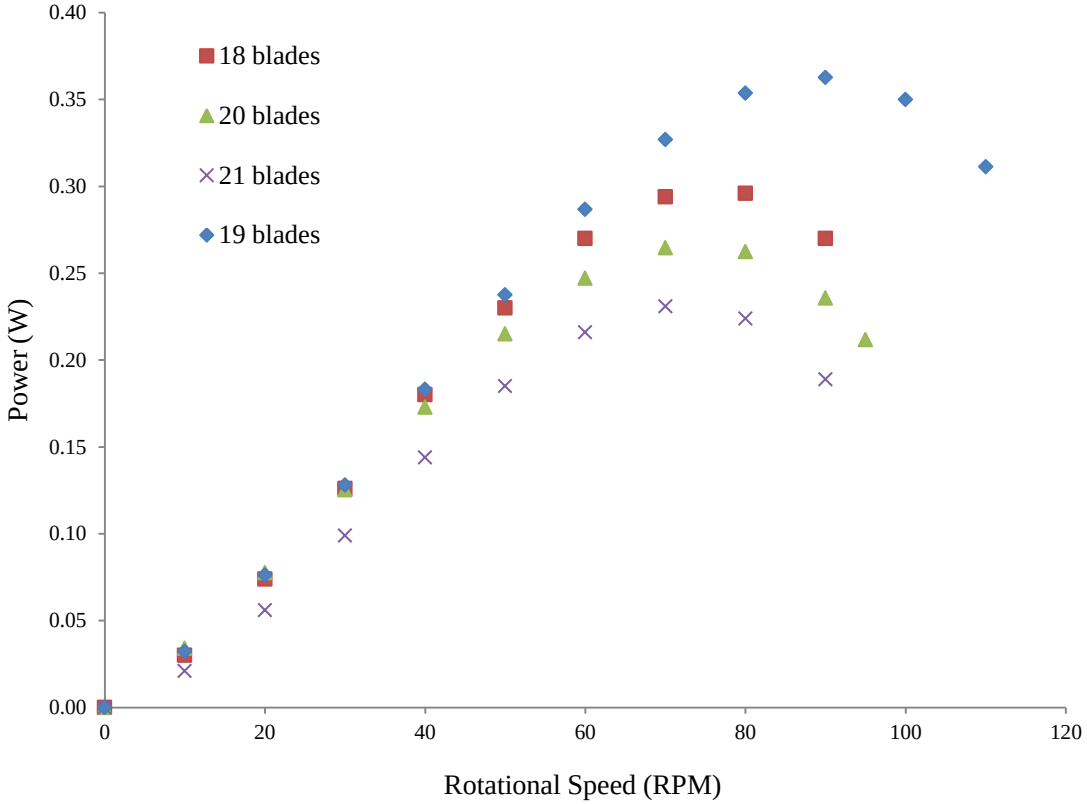

Figure 5.4: Power as a function of rotational speed for all prototype turbines

The power coefficients (C_P) and tip speed ratios (λ) for all turbine configurations have been determined at all wind speeds tested. The power coefficient versus tip speed ratio at 5.5m/s is shown in Figure 5.5. The power coefficients (C_P) achieved at 5.5 m/s wind speed are 0.091 at λ=0.152, 0.111 at λ=0.171, 0.081 at λ=0.133 and 0.071 at λ=0.133 for 18 blades, 19 blades, 20 blades and 21 blades turbines respectively. It is noted that the power coefficient increases with the increase of tip speed ratio (λ) until the peak level is obtained and then it decreases and finally becomes zero as the turbine attains its constant maximum rotational speed. Again, the 19 blades prototype turbine possesses the highest power coefficient (0.111). The lowest power coefficient (0.071) is obtained for 21 blades configuration.

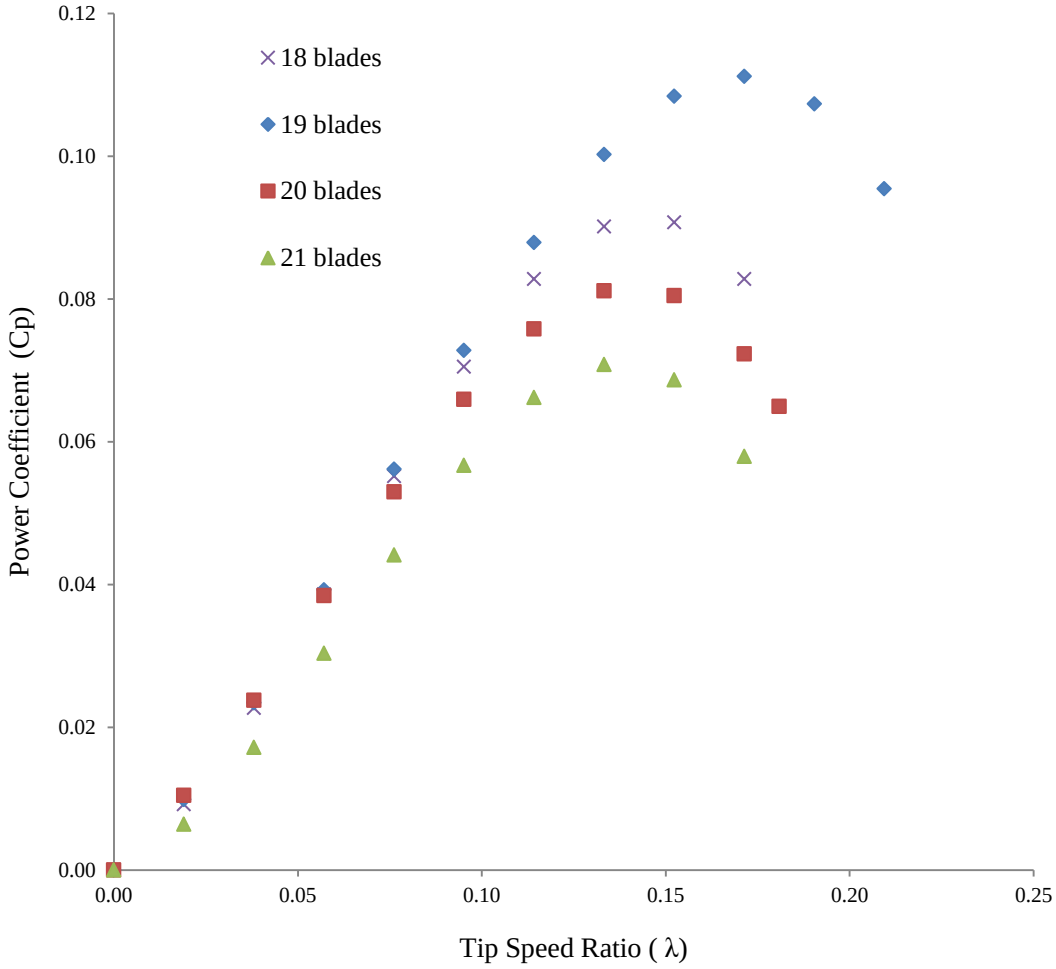

Figure 5.5: Power coefficient as a function of tip speed ratio at 5.5m/s wind speed

The torque coefficient (C_T) variation with tip speed ratio (λ) is illustrated in Figure 5.6. The torque coefficients achieved at 5.5 m/s wind speed are 0.784 at λ=0.076, 0.856 at λ=0.076, 0.752 at λ=0.076 and 0.728 at λ=0.076 for 18 blades, 19 blades, 20 blades and 21 blades configurations respectively. It is interesting to note that variable torque coefficients were obtained at approximately the same tip ratio for all wind turbine configurations. The highest torque coefficient is obtained for the 19 blades turbine. The lowest torque coefficient is obtained from the 21 blades configuration. The torque coefficient value indicates that the top ranking is 19 blades turbine followed by 18, 20 and 21 blades turbines. The 19 blades turbine performs well at other speeds tested.

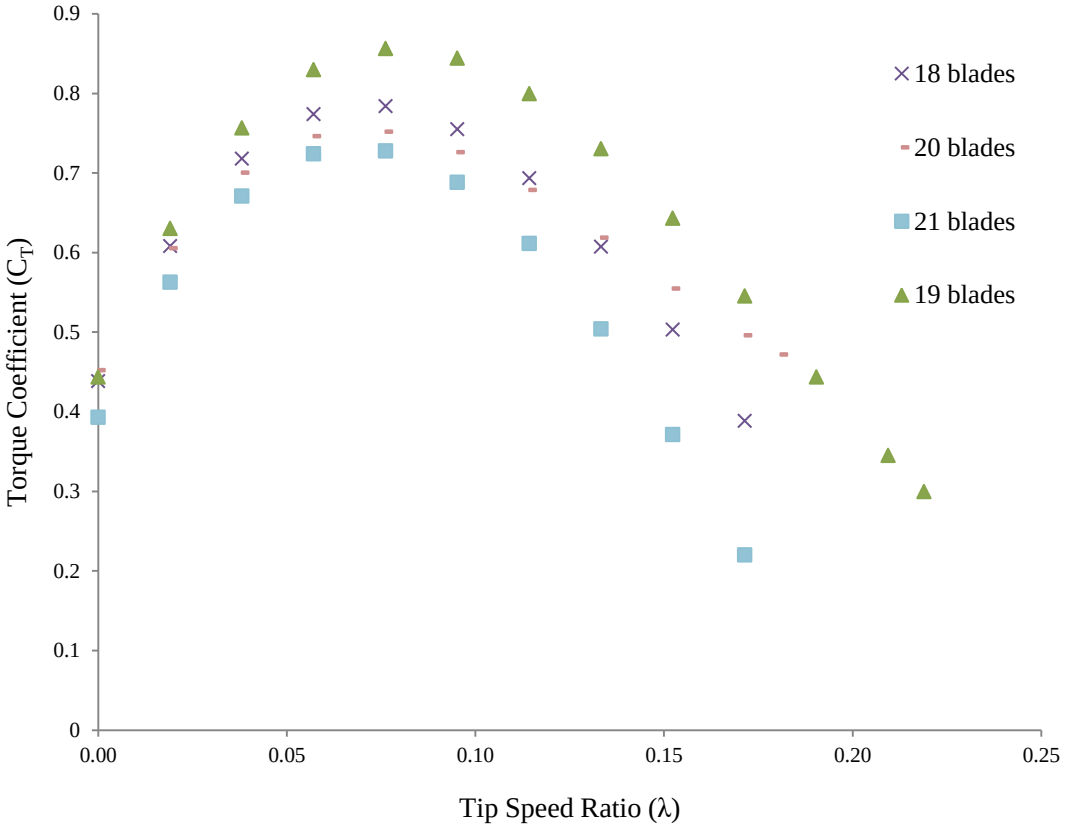

Figure 5.6: Torque coefficient versus tip speed ratio for 18, 19, 20 and 21 blade turbines

It can be concluded that an empirical relationship has been established to predict an optimal number of blades for a constant diameter multi-blade single stage drag-base vertical axis wind turbine. It should be noted that the optimal clearance was determined to be in between of 5.5 mm to 6.5 mm. The experimental data obtained for two different diameter prototype turbines have confirmed the validity of the developed empirical relationship.

5.2 Implication of Empirical Model

The power coefficient (C_P) variation with tip speed ratio (λ) for 200 mm diameter turbine with 19 blades and 300 mm diameter with 32 blades is shown in Figure 5.7. The power coefficient (C_P) achieved at 5.5 m/s wind speed are 0.111 at λ=0.171 and 0.125 at λ=0.343 for the 200 mm diameter turbine with 19 blades and 300 mm diameter turbine with 32 blades

configuration respectively. The tip speed ratio (λ) of the 300 mm diameter turbine is 2 times higher than the 200 mm diameter turbine. This indicates that the 300 mm diameter turbine with 32 blades can rotate faster at low wind speeds. In terms of power coefficient, the larger diameter turbine's C_P is 0.125 compared to 0.111 for the 200 mm diameter turbine.

A comparative analysis indicates that the power output increases with the increase of turbine diameter. The 300 diameter turbine with 32 blades generates around 13% more power compared to 200 mm diameter 19 blades turbine.

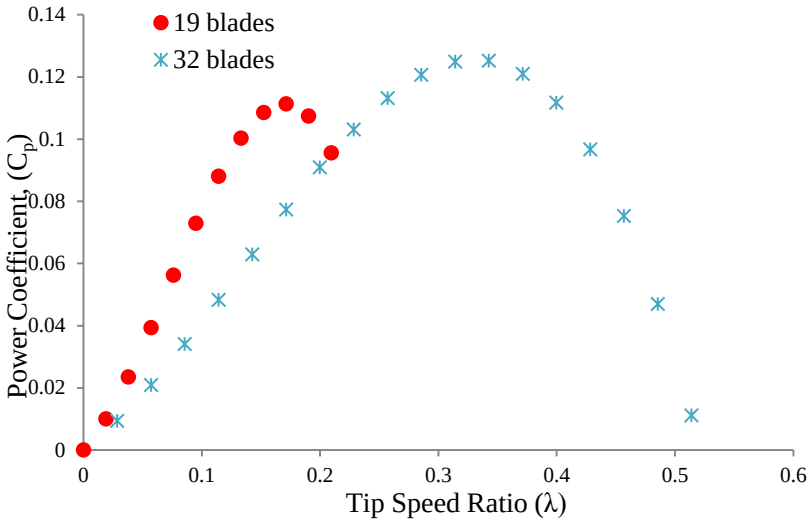

Figure 5.7: Power Coefficient versus tip speed ratio of 19 blades and 32 blades turbine

A comparative production cost analysis of 200 mm and 300 mm diameter prototype turbines has been undertaken to determine unit cost. Only four units of 200 mm and six units of 300 mm diameter turbines were produced. The various components and their retail costs are shown in Tables 5.3 and 5.4. The average cost for a 200 mm diameter turbine is approximately AUD 170 and the unit cost for a 300 mm diameter turbine is around AUD178. The cost of generator and inverter has not been included here. The average mass production cost per unit will significantly be lower than the cost estimated in this study.

Table 5.3: Production cost AUD for a 200 mm diameter turbine

Cost for 4 turbines		4 units	Single Unit
P.V.C pipes	15 m@$2.50	37.50	9.38
Acrylic sheets	1 sheet@$55 each	55.00	13.75
Glue	2 Tubes@$3.50 each	7.00	1.75
Flange	4 units@$10	40.00	10.00
Shaft	20 mm shaft, 4m@$5	20.00	5.00
Bearings	8 units@$15	120.00	30.00
Labour	8 hrs@$50	400.00	100.00
Total		679.50	169.88

Table 5.4: Production Cost AUD for a 300 mm Diameter Turbine

Cost for 6 turbines		6 units	Single Unit
P.V.C pipes	30 m@$2.50	75.00	12.50
Acrylic sheets	2 sheets@$55 each	110.00	18.33
Glue	3 Tubes@$3.50 each	10.50	1.75
Flange	6 units@$10	60.00	10.00
Shaft	20 mm shaft, 6m@$5	30.00	5.00
Bearings	12 units@$15	180.00	30.00
Labour	12 hrs@$50	600.00	100.00
Total		1065.50	177.58

CHAPTER 6

Conclusions

The main objectives of this work were to understand the effects of blade number, clearance (gap) between subsequent blades and turbulent wind condition on Vertical Axis Wind Turbine (VAWT)'s rotational speed, torque and power. The following conclusions apply within the assumptions made in the analysis and experiments, the sensitivity of the measurements and the limits of scientific and engineering inference. In particular, it is emphasised that these conclusions apply to the range of VAWT model shapes tested to within the range of test conditions investigated. It is possible that some of the conclusions have much wider applications. The following conclusions are therefore drawn:

6.1 Major Conclusions

An empirical relationship has been established to predict an optimal blade number for a constant diameter multi-blade single stage drag-base vertical axis wind turbine. The experimental data obtained for two different diameter prototype turbines have confirmed the validity of the developed empirical relationship.

Power is highly dependent on blade number and blade spacing. With the increase of blade number, the power increases till it reaches an optimal blade number thereafter it starts to decrease.

The optimal blade spacing was found to be between 5.5 mm and 6.5 mm for the prototype turbines.

A flow enhancing device (cowling) was designed and employed to explore its effectiveness on turbine rotational speed (RPM) and torque. The flow enhancing device had shown a positive impact on the turbine RPM however, the overall torque and power was found to be lower compared to turbines without its employment.

6.2 Minor Conclusions

Wind turbulence intensity has significant impact on power output. The power decreases with an increase of turbulence. However, the airflow rate or volume flow rate has much higher impact on the power output.

The power can be increased by approximately two times when the blade diameter is scaled up. Doubling the blade diameter increases the amount of wind energy the turbine blades are able extract.

Optimal power output depends on a) blade number, b) blade spacing, c) blade angle, d) turbulence intensity, and e) airflow rate.

CHAPTER 7

Suggestion for Further Work

After conducting the work presented here and reviewing the literature available in the public domain, the following conclusions are made for further study:

1. In this study, a disk brake was used to apply a mechanical braking torque. However, an eddy motor is required to provide a known resistance torque loads. The torque generated by and eddy motor is directly proportional to the current applied to control the current of the motor.
2. The scalability of small scale vertical axis wind turbine was not studied at local radii between 80 mm and 160 mm in the current work. It would be useful to study the effect of scalability at different radii to obtain a comprehensive understanding of the effect of scalability.
3. In an open environment, small scale vertical axis wind turbine blades can experience wind from any directions with varied gustiness which can have effect on aerodynamic parameters optimised in no crosswind conditions. Therefore, it would be useful to undertake further study on crosswinds and wind gustiness effects.
4. A correlation between small scale vertical axis wind turbine and full-scale tests in wind tunnel as well as field test will be useful.

REFERENCES

Abas, N., Kalair, A. and Khan, N. (2015). Review of fossil fuels and future energy technologies. *Futures*, Vol.69: 31-49.

Akwa, J.V., Vielmo, H.A. & Petry, A.P. (2012). A review on the performance of Savonius wind turbines. *Renewable and Sustainable Energy Reviews*, Vol.16: 3054-3064.

Ahmed, N. A. (2013). A novel small scale efficient wind turbine for power generation. *Renewable Energy*, Vol. 57**:** 79-85.

Akbar, M. A., & Mustafa, V. (2016). A new approach for optimization of Vertical Axis Wind Turbines. *Journal of Wind Engineering and Industrial Aerodynamics*, Vol.153: 34-45.

Alam, F. (2000). *The effects of car A-pillar and windshield geometry on local flow and noise.* PhD Thesis, Royal Melbourne Institute of Technology.

Alam, F. & Golde, S. (2013). An Aerodynamic Study of a Micro Scale Vertical Axis Wind Turbine. *Procedia Engineering*, Vol: 56**:** 568-572.

Alexander, A. J., & Holownia, B. P. (1978). Wind tunnel tests on a Savonius rotor. Journal of Wind Engineering and Industrial Aerodynamics, Vol. 3(4): 343-351.

Ali, M.H. (2013). Experimental comparison study for Savonius wind turbine of two & three blades at low wind speed. *International Journal of Modern Engineering Research (IJMER)*, Vol. 3(5): 2978-2986.

Altan, B.D. and Atılgan, M. (2008). An experimental and numerical study on the improvement of the performance of Savonius wind rotor. *Energy Conversion and Management*, Vol. 49(12): 3425-3432.

Bahaj, A. S., Myers, L., & James, P. A. B. (2007). Urban energy generation: Influence of micro-wind turbine output on electricity consumption in buildings. *Energy and Buildings*, Vol. 39(2): 154-165.

Bhutta, M. M. A., Hayat, N., Farooq, A. U., Ali, Z., Jamil, S. R., & Hussain, Z. (2012). Vertical axis wind turbine–A review of various configurations and design techniques. *Renewable and Sustainable Energy Reviews*, Vol. 16(4): 1926-1939.

Blackwell, B.F., Sheldahl, R.F. and Feltz, L.V. (1977). Wind tunnel performance data for two-and three-bucket Savonius rotors, 1-105. Springfield, VA, USA: Sandia Laboratories.

Blocken, B. & Carmeliet, J. (2004). Pedestrian wind environment around buildings: literature review and practical examples. *Journal of Thermal Envelope and Building Science*, Vol. 28: 107-159.

Blocken, B. & Persoon, J. (2009). Pedestrian wind comfort around a large football stadium in an urban environment: CFD simulation, validation and application of the new Dutch wind nuisance standard. *Journal of Wind Engineering and Industrial Aerodynamics,* Vol. 97: 255-270.

Breitsamter, C. (2011). Wake vortex characteristics of transport aircraft. *Progress in Aerospace Sciences,* Vol. 47: 89-134.

Builds Solar. (http://www.build.com.au/how-does-solar-power-work). [Accessed 5 October 2017)

Burton, T., S. D., Jenkins N., Bossanyi, E. (2001). *Wind Energy Handbook*, John Wiley & Sons, ISBN: 9780471489979

Cermak, J.E. and Isyumov, N., (1998). American Society of Civil Engineers. Task Committee on Manual of Practice for Wind Tunnel Testing of Buildings and, S.

Chehouri, A., Younes, R., Ilinca, A., & Perron, J. (2015). Review of performance optimization techniques applied to wind turbines. *Applied Energy,* Vol. 142: 361-388.

Cheng, M.Y., Chiu, K.C., Lien, L.C., Wu, Y.W. & Lin, J.J. (2016). Economic and energy consumption analysis of smart building – MEGA house. *Building and Environment,* Vol. 100**:** 215-226.

Coppin, P., Ayotte, K. A., & Steggel, N. (2003). Wind resource assessment in Australia: a planners guide (pp. 40-50). CSIRO Wind Energy Research Unit.

Council, C. E. (2015). Clean energy Australia report. Melbourne, VIC, Australia: Clean Energy Council. Available on: (https://www.cleanenergycouncil.org.au/policy-advocacy/reports/clean-energy-australia-report.html). [Accessed on 15 March 2017]

Cresswell, R., Petheram, C., Harrington, G., Buettikofer, H., Hodgen, M., Davies, P. & Li, L. (2009). Water Resources in Northern Australia. *Northern Australia Land and Water Science Review.*

Danao, L. A., Edwards, J., Eboibi, O. & Howell, R. (2014). A numerical investigation into the influence of unsteady wind on the performance and aerodynamics of a vertical axis wind turbine. *Applied Energy,* Vol.116: 111-124.

Driss, Z., Damak, A. and Abid, M.S., (2015). Evaluation of the Savonius Wind Rotor Performance for Different External Overlap Ratios. *International Journal of Fluid Mechanics & Thermal Sciences,* Vol. 1(1): 14.

El-Askary, W. A., Nasef, M. H., Abdel-Hamid, A. A., & Gad, H. E. (2015). Harvesting wind energy for improving performance of Savonius rotor. *Journal of Wind Engineering and Industrial Aerodynamics,* Vol. 139: 8-15.

Enhar. (2010). Victorian Consumer Guide to Small Wind Turbine Generation Sustainability Victoria. Melbourne, Victoria.

Eriksson, S., Bernhoff, H. & Leijon, M. (2008). Evaluation of different turbine concepts for wind power. *Renewable and Sustainable Energy Reviews*, Vol. 12: 1419-1434.

Fujisawa, N. (1992), On the torque mechanism of Savonius turbines. *Journal of Wind Engineering and Industrial Aerodynamics*, Vol. 40(3): 277-292.

Global Energy Statictical Yearbook (2016). World electricity production statictics. Available on: (https://yearbook.enerdata.net/electricity/world-electricity-production-statistics.). [Accessed on 18 December 2017)

Global Wind Energy Council. (2015). Global wind energy statistics. Available on: (http://www.gwec.net/global-figures/wind-in-numbers/). [Accessed 15 March 2017].

Golecha, K., Eldho, T.I. and Prabhu, S.V. (2011). Influence of the deflector plate on the performance of modified Savonius water turbine. *Applied Energy*, Vol. 88(9): 3207-3217.

Hau, E. (2013), Wind Turbines: Fundamentals, Technologies, Application and Economics. Springer, Berlin, p. 783, ISBN: 978-3-642-06348-0.

Hayashi, T., Li, Y. and Hara, Y. (2005). Wind tunnel tests on a different phase three-stage Savonius rotor. J*SME International Journal Series B Fluids and Thermal Engineering*, Vol. 48(1): 9-16.

Hoerner, S.F. (1965), Fluid-dynamic drag: practical information on aerodynamic drag and hydrodynamic resistance, Hoerner Fluid Dynamics, ISBN: 9991194444.

Ikegaya, N., Hirose, C., Hagishima, A. & Tanimoto, J. (2016). Effect of turbulent flow on wall pressure coefficients of block arrays within urban boundary layer. *Building and Environment*, Vol. 100: 28-39.

Institute for Energy Research (IER) (2012). Electric Generating Costs: A Primer. (https://instituteforenergyresearch.org/analysis/electric-generating-costs-a-primer/). [Accessed 30 April 2017].

IRENA (2018), Renewable Power Generation Costs in 2017, International Renewable Energy Agency, Abu Dhabi.

International Energy Agency (2017). World Energy Outlook. (http://www.iea.org/media/weowebsite/2017/Chap1_WEO2017.pdf)

International Energy Agency (2017). Key World Energy Statictics (KWES). (https://www.iea.org/publications/freepublications/publication/KeyWorld2017.pdf)

International Gas Union (IGU) (2017). World IGU Report. (https://www.igu.org/news/igu-releases-2017-world-lng-report). [Accessed 15 December 2017].

Irabu, K. and Roy, J. N. (2007). Characteristics of wind power on Savonius turbine using a guide-box tunnel, *Experimental Thermal and Fluid Sciences*, Vol. 32(2): 580-586.

Jian, C., Kumbernuss, J., Linhua, Z., Lin, L. and Hongxing, Y. (2012). Influence of phase-shift and overlap ratio on Savonius wind turbine's performance. *Journal of Solar Energy Engineering,* Vol. 134(1):011-016.

Kamoji, M., S.B. Kedare, and S. Prabhu. (2009). Experimental investigations on single stage modified Savonius rotor. Applied Energy, Vol. 86(7-8): p. 1064-1073.

Katsigiannis, Y. & Stavrakakis G. (2014). Estimation of wind energy production in various sites in Australia for different wind turbine classes: a comparative technical and economic assessment. *Renewable Energy*, Vol. 67: 230–6.

Kosasih, B., & Hudin, H. S. (2016). Influence of inflow turbulence intensity on the performance of bare and diffuser-augmented micro wind turbine model. *Renewable Energy,* Vol.87: 154-167.

Lee, S., & Lee, S. (2014). Numerical and experimental study of aerodynamic noise by a small wind turbine. *Renewable Energy,* Vol. 65: 108-112..

Li, Q. A., Maeda, T., Kamada, Y., Murata, J., Yamamoto, M., Ogasawara, T., & Kogaki, T. (2016). Study on power performance for straight-bladed vertical axis wind turbine by field and wind tunnel test. *Renewable Energy*, Vol. 90: 291-300.

Lien, F., Yee, E. & Cheng, Y. (2004). Simulation of mean flow and turbulence over a 2D building array using high-resolution CFD and a distributed drag force approach. *Journal of Wind Engineering and Industrial Aerodynamics*, Vol. 92: 117-158.

Lim, H., Thomas, T. & Castro, I. (2009). Flow around a cube in a turbulent boundary layer: LES and experiment. *Journal of Wind Engineering and Industrial Aerodynamics,* Vol. 97: 96-109.

Loganathan, B., Chowdhury, H., Mustary, I. and Alam, F. (2015). An experimental study of a cyclonic vertical axis wind turbine for domestic scale power generation. *Procedia Engineering*, Vol.105: pp.686-691.

Loganathan, B., Mustary, I., Chowdhury, H. and Alam, F. (2017). Effect of Turbulence on a Savonius Type Micro Wind Turbine, *Energy Procedia*, Vol. 110: 549-554.

Lovett, T., Lee, J., Gabe-Thomas, E., Natarajan, S., Brown, M., Padget, J. & Coley, D. (2016). Designing sensor sets for capturing energy events in buildings. *Building and Environment,* Vol. 110: 11-22.

Lubitz, W. D. (2014). Impact of ambient turbulence on performance of a small wind turbine. *Renewable Energy*, Vol. 61: 69-73.

Mahmoud, N.H., El-Haroun, A.A., Wahba, E. and Nasef, M.H. (2012). An experimental study on improvement of Savonius rotor performance. *Alexandria Engineering Journal*, Vol. 51(1): 19-25.

Mendis, P., Ngo, T.D., Haritos, N., Hira, A., Samali, B. and Cheung, J. (2007), Wind loading on tall buildings, *Electronic Journal of Structural Engineering*, Special Issue, 41-54.

Menet, J. L. (2004). A double-step Savonius rotor for local production of electricity: a design study. *Renewable Energy*, Vol. 29(11): 1843-1862.

Oke, T.R., 1976. The distinction between canopy and boundary-layer urban heat islands. *Atmosphere*, Vol.14(4): 268-277.

Pagnini, L. C., Burlando, M. & Repetto, M. P. (2015). Experimental power curve of small-size wind turbines in turbulent urban environment. *Applied Energy,* Vol. 154: 112-121.

Pitteloud, J.D. & Gsänger, S. (2017). Small Wind World Report. *World Wind Energy Associations***,** Vol. 29: 1-16.

REN21 Renewables Global Status Report (2017). REN21 Renewable Energy Policy Network for the 21st century. (http://www.ren21.net/status-of-renewables/global-status-report/). [Accessed on 2 October 2017].

Saha, U.K., Thotla, S. and Maity, D. (2008). Optimum design configuration of Savonius rotor through wind tunnel experiments. *Journal of Wind Engineering and Industrial Aerodynamics*, Vol. 96(8-9): 1359-1375.

Roy, S., & Saha, U. K. (2015). Wind tunnel experiments of a newly developed two-bladed Savonius-style wind turbine. *Applied Energy*, Vol. 137: 117-125.

Saha, U. K. & Rajkumar, M. J. (2006). On the performance analysis of Savonius rotor with twisted blades. *Renewable Energy,* Vol .31: 1776-1788.

Saeidi, D., Sedaghat, A., Alamdari, P., & Alemrajabi, A. A. (2013). Aerodynamic design and economical evaluation of site specific small vertical axis wind turbines. *Applied Energy*, Vol. 101:, 765-775.

Sharma, K. K., Biswas, A., & Gupta, R. (2013). Performance Measurement of a three-bladed combined Darrieus-Savonius rotor. *International Journal of Renewable Energy Research*, Vol .3(4): 885-891.

Shaughnessy, B.M. and Probert, S.D. (1992). Partially-blocked Savonius rotor. *Applied Energy,* Vol. 43(4): 239-249.

Singh, M. A., Biswas, A., & Misra, R. D. (2015). Investigation of self-starting and high rotor solidity on the performance of a three S1210 blade H-type Darrieus rotor. *Renewable Energy*, Vol .76: 381-387.

Statistics Norway. (2016). (https://www.ssb.no/en). [Assessed 5 May 2017]

Sun, H. & Huang, S. (2001). Simulation of Wind Flow Around a Building with ak–ε Model. *Theoretical and Computational Fluid Dynamics*, Vol. 14: 283-292.

Sunderland, K., Woolmington, T., Blackledge, J., & Conlon, M. (2013). Small wind turbines in turbulent urban environments: A consideration of normal and Weibull distributions

for power prediction. *Journal of Wind Engineering and Industrial Aerodynamics*, Vol. 121: 70-81.

Tu, J., Yeoh, H. G., Liu, C. (2008). *Computational Fluid Dynamics: A Pratical Approach,* UK, Butterworth-Heinemann, ISBN: 9780080982434

Tummala, A., Velamati, R. K., Sinha, D. K., Indraja, V., & Krishna, V. H. (2016). A review on small scale wind turbines. *Renewable and Sustainable Energy Reviews*, Vol. 56: 1351-1371.

US. Energy Information Administration (2017). International Energy Outlook 2017. (https://www.eia.gov/outlooks/aeo/). [Accessed 15 December 2017]

US Energy Information Administration (EIA), Updated capital cost estimates for utility scale electricity generating plants, November 2016. (https://www.eia.gov/analysis/studies/powerplants/capitalcost/pdf/capcostassumption) [Accessed 15 December 2017]

US. Geological Survey. (2015). (http://water.usgs.gov/edu/hyhowworks.html). [Accessed 5 July 2016]

Webb, A. (2007). The viability of domestic wind turbines for urban Melbourne, *Sustainability Victoria*, 1-53, June.

Wekesa, D. W., Wang, C., Wei, Y., & Zhu, W. (2016). Experimental and numerical study of turbulence effect on aerodynamic performance of a small-scale vertical axis wind turbine. *Journal of Wind Engineering and Industrial Aerodynamics*, Vol. 157: 1-14.

Wenehenubun, F., Saputra, A., & Sutanto, H. (2015). An experimental study on the performance of Savonius wind turbines related with the number of blades. *Energy Procedia*, Vol. 68: 297-304.

World Energy Council (2016). World Energy Resources, 1-1028, London, UK. (www.worldenergy.org). [Assesssed on October 2017]

World Energy Council (2017). World Energy Issues Monitor. https://www.worldenergy.org/data/issues-monitor/). [Accessed 30 December 2017]

World Nuclear Association (2018). Economics of Nuclear Power. (http://www.world-nuclear.org/information-library/economic-aspects/economics-of-nuclear-power.aspx). [Accessed 31 May 2018]

Yang, A. S., Su, Y. M., Wen, C. Y., Juan, Y. H., Wang, W. S., & Cheng, C. H. (2016). Estimation of wind power generation in dense urban area. *Applied Energy*, Vol. 171: 213-230.

Yoon, S.H., Lim, H.C. & Kim, D.K. (2013). Study of several design parameters on multi-blade vertical axis wind turbine. *International Journal of Precision Engineering and Manufacturing*, Vol. 14: 831-837.

BIBLIOGRAPHY

Akwa, J. , Vielmo, H. , & Petry, A. (2012). A review on the performance of Savonius wind turbines. *Renewable and Sustainable Energy Reviews,* Vol. 16(5): 3054-3064.

Bavanish, B., & Thyagarajan, K. (2013). Optimization of power coefficient on a horizontal axis wind turbine using bem theory. *Renewable and Sustainable Energy Reviews,* Vol. 26: 169-182.

Biadgo, M. A., Simonović, A., Komarov, D., & Stupar, S. (2013). Numerical and analytical investigation of vertical axis wind turbine. *FME Transactions*, Vol. 41(1): 49-58.

Butterfield, P., Scott, G., & Musial, W., (1992). Comparison of wind tunnel airfoil performance data with wind turbine blade data. *Journal of Solar Energy Engineering,* Vol. 114(2): 119-124.

Castelli, M. R., Englaro, A., & Benini, E. (2011). The Darrieus wind turbine: Proposal for a new performance prediction model based on CFD. *Energy*, Vol. 36(8): 4919-4934.

Choi, N., Hyun S., Hyun, J., & Chun, K. (2013). Numerical study on the horizontal axis turbines arrangement in a wind farm: Effect of separation distance on the turbine aerodynamic power output. *Journal of Wind Engineering and Industrial Aerodynamics*, Vol. 117: 11-17.

Chong, W. T., Fazlizan, A., Poh, S. C., Pan, K. C., Hew, W. P., & Hsiao, F. B. (2013). The design, simulation and testing of an urban vertical axis wind turbine with the omni-direction-guide-vane. *Applied Energy*, Vol. 112: 601-609.

Elkhoury, M., Kiwata, T., & Aoun, E. (2015). Experimental and numerical investigation of a three-dimensional vertical-axis wind turbine with variable-pitch. *Journal of Wind Engineering and Industrial Aerodynamics*, Vol. 139: 111-123.

Du, Z., & Selig, M.S. (2000). The effect of rotation on the boundary layer of a wind turbine blade. *Renewable Energy*, Vol. 20(2): 167-181.

Eriksson, S., Bernhoff, H., & Leijon, M. (2008). Evaluation of different turbine concepts for wind power. *Renewable and Sustainable Energy Reviews*, Vol. 12(5): 1419-1434.

Fuglsang, P, & Madsen, HA. (1999). Optimization method for wind turbine rotors. *Journal of Wind Engineering and Industrial Aerodynamics,* Vol. 80(1): 191-206.

Guerri, O., Sakout, A., & Bouhadef, K. (2007). Simulations of the fluid flow around a rotating vertical axis wind turbine. *Wind Engineering*, Vol. 31(3): 149-163.

Hansen, A.C, & Butterfield, CP. (1993). Aerodynamics of horizontal-axis wind turbines. *Annual Review of Fluid Mechanics,* Vol. 25(1): 115-149.

Hirahara, H., Hossain, M. Z., Kawahashi, M., & Nonomura, Y. (2005). Testing basic performance of a very small wind turbine designed for multi-purposes. *Renewable Energy*, Vol. 30(8): 1279-1297.

Hu, D., Hua, O., & Du, Zhaohui. (2006). A study on stall-delay for horizontal axis wind turbine. *Renewable Energy*, Vol. 31(6): 821-836.

Joselin G.M., Iniyan, S., Sreevalsan, E., & Rajapandian, S. (2007). A review of wind energy technologies. *Renewable and Sustainable Energy Reviews*, Vol .11(6): 1117-1145.

Jung, Nam., No, S., & Ryu, K. (2005). Aerodynamic performance prediction of a 30kW counter-rotating wind turbine system. *Renewable Energy*, Vol. 30(5): 631-644.

Kishinami, K., Taniguchi, H., Suzuki, J., Ibano, H., Kazunou, T., & Turuhami, M. (2005). Theoretical and experimental study on the aerodynamic characteristics of a horizontal axis wind turbine. *Energy*, Vol. 30(11): 2089-2100.

Lanzafame, R, & Messina, M. (2010). Power curve control in micro wind turbine design. *Energy*, Vol. 35(2): 556-561.

Li, Q. A., Maeda, T., Kamada, Y., Shimizu, K., Ogasawara, T., Nakai, A., & Kasuya, T. (2017). Effect of rotor aspect ratio and solidity on a straight-bladed vertical axis wind turbine in three-dimensional analysis by the panel method. *Energy*, Vol. 121: 1-9.

Li, Q. S., Shu, Z. R., & Chen, F. B. (2016). Performance assessment of tall building-integrated wind turbines for power generation. *Applied Energy*, Vol. 165: 777-788.

Manwell, J. F., McGowan, J. G., & Rogers, A. L. (2010). Wind energy explained: theory, design and application. John Wiley & Sons, ISBN: 978-0-470-01500-1

Mirecki, A., Roboam, X., & Richardeau, F. (2007). Architecture complexity and energy efficiency of small wind turbines. *Industrial Electronics, IEEE Transactions on Industrial Electronics*, Vol. 54(1): 660-670.

Muller, G., Jentsch, M. F., & Stoddart, E. (2009). Vertical axis resistance type wind turbines for use in buildings. *Renewable Energy*, Vol. 34(5): 1407-1412.

Rezaeiha, A., Kalkman, I., & Blocken, B. (2017). Effect of pitch angle on power performance and aerodynamics of a vertical axis wind turbine. *Applied Energy*, Vol. 197: 132-150.

Sedaghat, A., & Mirhosseini, M. (2012). Aerodynamic design of a 300kW horizontal axis wind turbine for province of Semnan. *Energy Conversion and Management*, Vol. 63: 87-94.

Shen, Zhong., Mikkelsen, R., Sørensen, N., & Bak, C. (2005). Tip loss corrections for wind turbine computations. *Wind Energy*, Vol. 8(4): 457-475.

Singh, R.K., & Ahmed, M.R. (2013). Blade design and performance testing of a small wind turbine rotor for low wind speed applications. *Renewable Energy*, Vol. 50: 812-819.

Spera, D.A. (1994). Introduction to modern wind turbines. *Wind turbine technology: fundamental concepts of wind Turbine engineering. ASME Press, New York*, DOI:10.1115/1.802601.

Sumner, J., Watters, C.S. & Masson, C. (2010). CFD in Wind Energy: The Virtual, Multiscale Wind Tunnel. *Energies*, Vol. 3(5): 989-1013.

Tadamasa, A. & Zangeneh, M. (2011). Numerical prediction of wind turbine noise. *Renewable Energy*, Vol. 36(7): 1902-1912.

Thumthae, C. & Chitsomboon, T. (2009). Optimal angle of attack for untwisted blade wind turbine. *Renewable Energy*, Vol. 34(5): 1279-1284.

Toja-Silva, F., Colmenar-Santos, A. & Castro-Gil, M. (2013). Urban wind energy exploitation systems: Behaviour under multidirectional flow conditions-Opportunities and challenges. *Renewable and Sustainable Energy Reviews*, Vol. 24: 364-378.

Xu, G., & Sankar, L. (2000). Computational study of horizontal axis wind turbines. *Journal of Solar Energy Engineering*, Vol. 122(1): 35-39.

Yusaf, T., Goh, S. & Borserio, J.A. (2011). Potential of renewable energy alternatives in Australia. *Renewable and Sustainable Energy Reviews,* Vol. 15(5): 2214-2221.

APPENDIX A:

Technical Drawings of Wind Turbine

A.1: Full Scale Vertical Axis Wind Turbine Assembly

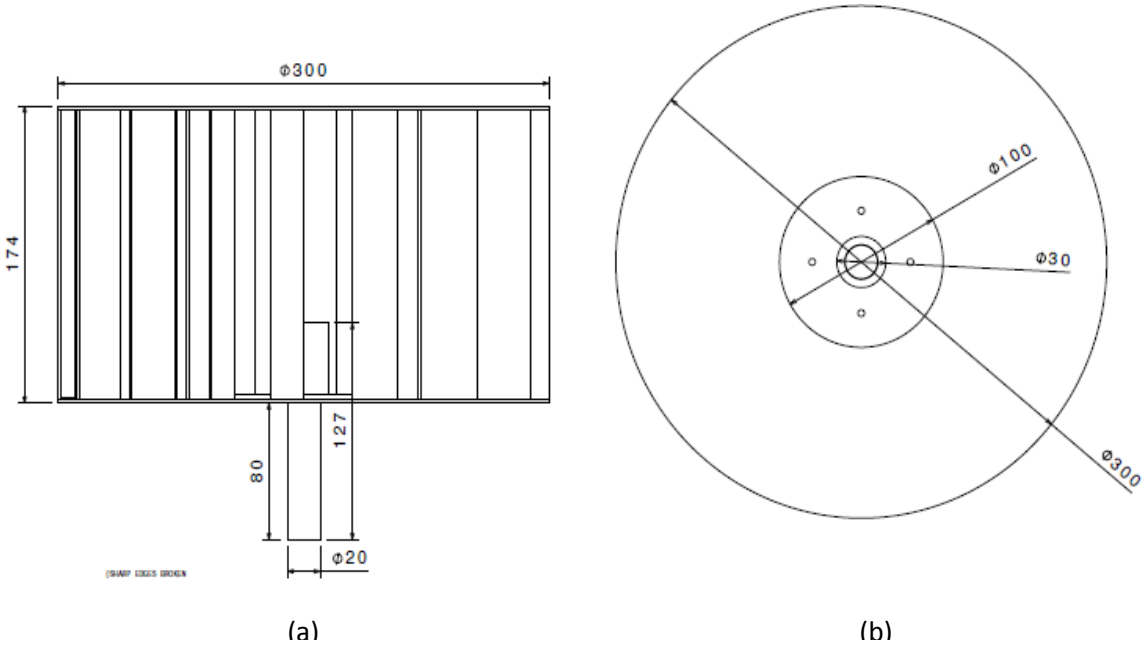

Figure A. 1: Wind turbine assembly (a) side view (b) top view

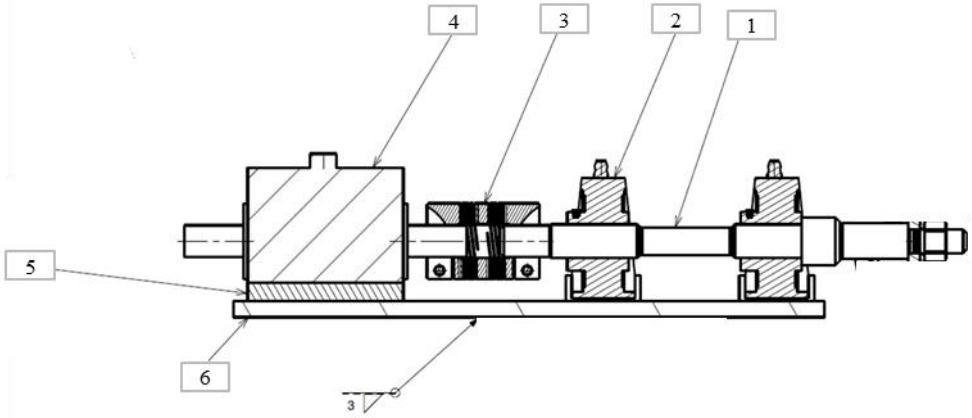

Figure A.2: Side section view B-B

Table A. 1: Wind turbine components

Component	Description
1	Shaft
2	Bearing housing unit
3	Flexible coupling
4	HBM torque transducer
5	Wedge plate
6	Top plate Stand

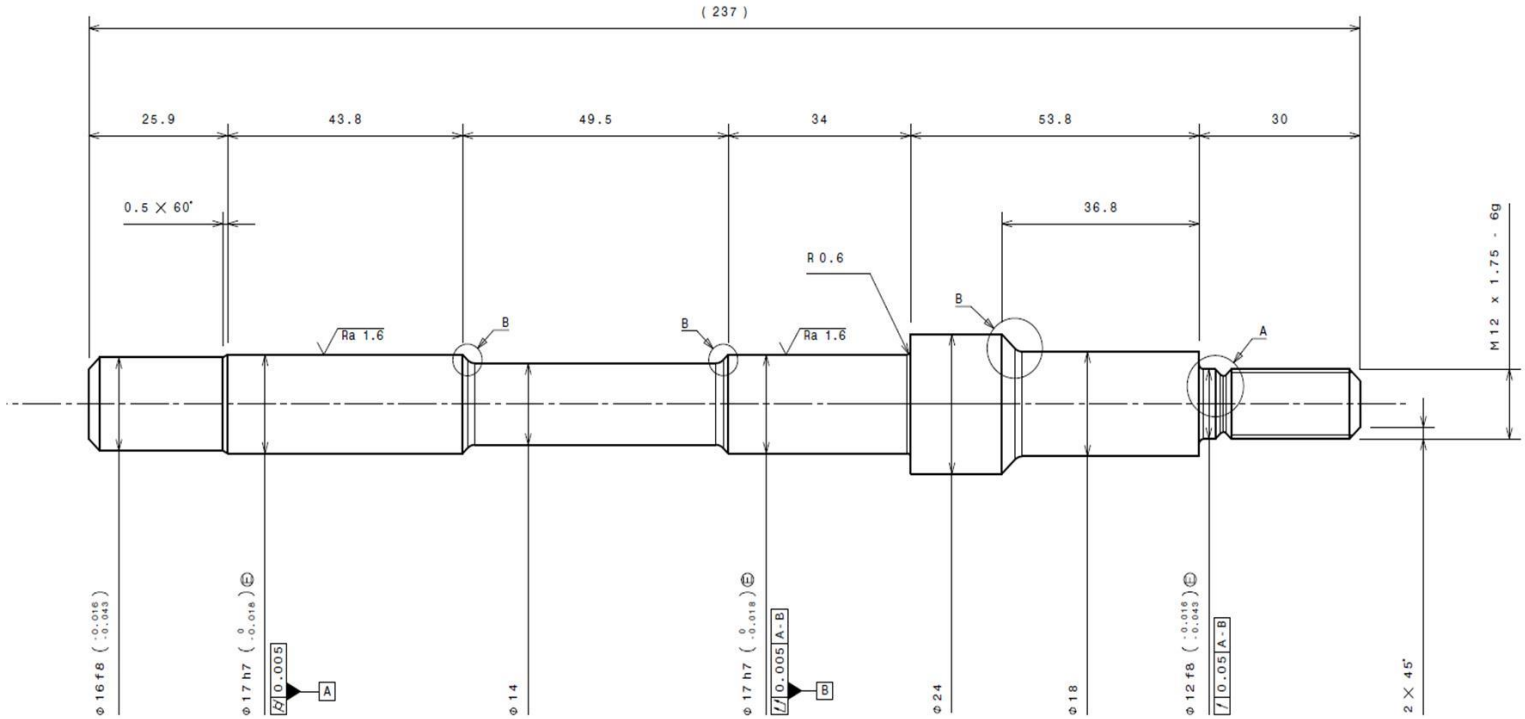

Figure A.3: Shaft dimensions

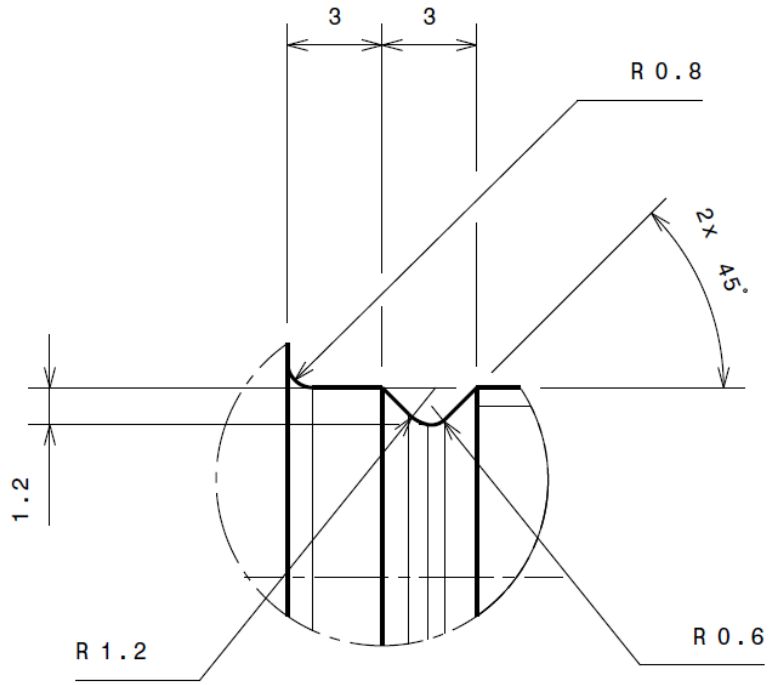

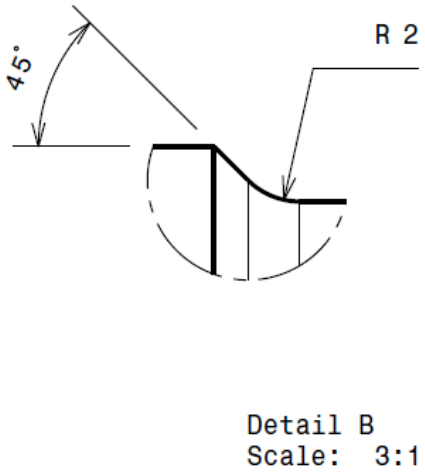

Figure A.4: Wind turbine main shaft dimension

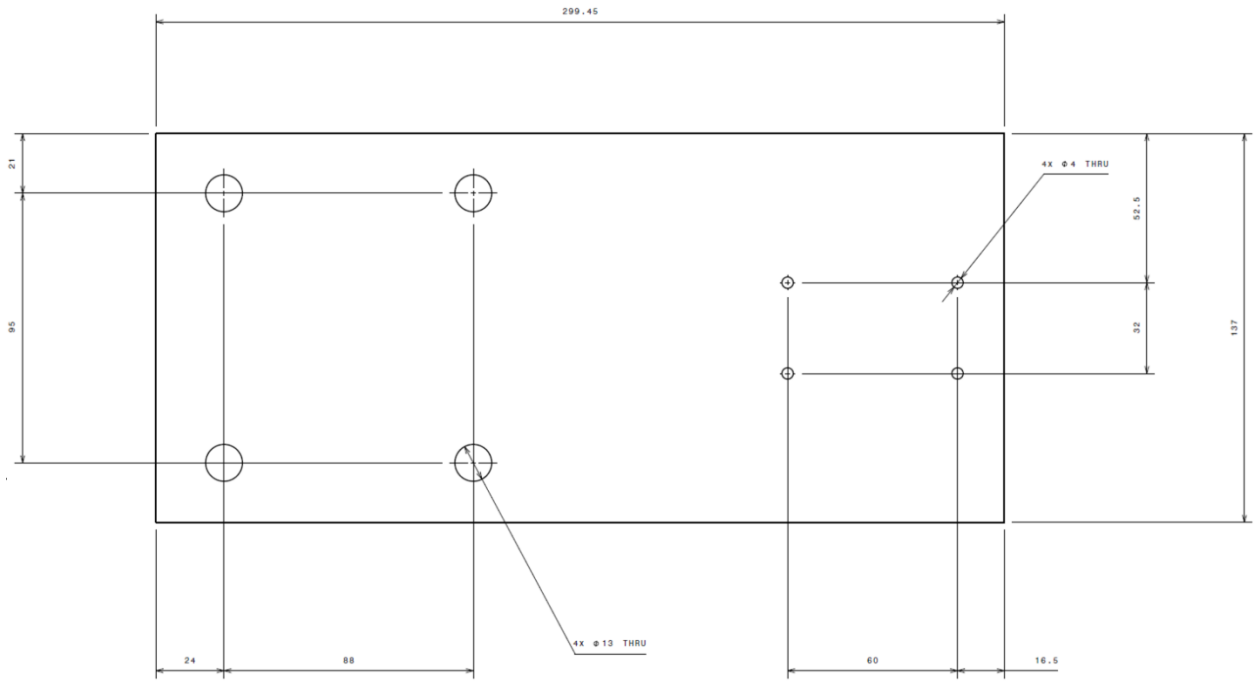

(a)

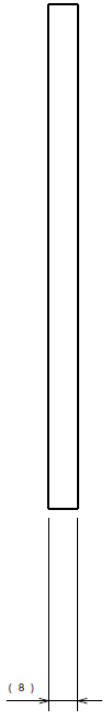

(b)

Figure A.5: Top plate dimensions

A.2: Flexible Coupling

A flexible beam coupling is used for the experiment of the wind turbine due to its robustness and light weight. Detailed specification of the coupling is given Table A.7.

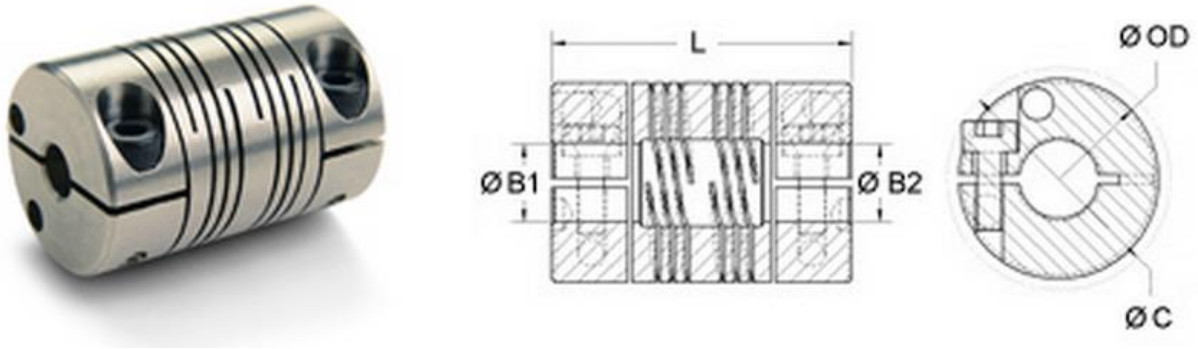

Figure A. 1: Aluminium flexible beam coupling

Table A. 2: Specification of flexible beam coupling

Product Number	FCMR38-16-16-A
Product Type	Beam Coupling
Style	Clamp
Material	7075 Aluminium
Finish	Bright
Dimensions	
Bore B1	16mm
Bore B2	16 mm
Outer Diameter OD	38.1 mm
Length L	57.2 mm
Shaft Penetration	26.47 mm
Clearance Diameter C MAX	41.71 mm
Fastening Hardware	
Cap Screw	M5
Screw Material	Alloy Steel with Nypatch

Screw Finish	Black Oxide
Seating Torque	9.5 Nm
Hex Wrench	4.0 mm
Torque Specifications	
Static Torque	10.73 Nm
Dynamic Torque Non-Reversing	5.37 Nm
Dynamic Torque Reversing	2.68 Nm
Misalignment	
Angular Misalignment	3°
Partial Misalignment	0.76 mm
Axial Motion	0.38 mm
Additional Information	
Torsional Stiffness	0.39 Deg/Nm
Moment of Inertia	30.032 $x10^{-6}$ kg-m^2
Maximum Speed	6000RPM
Bore Tolerance	+.025mm / -.000mm
Temperature Range	-40°F to 225°F
	-40°C to 107°C

A.3: Self-Aligning Ball Bearing

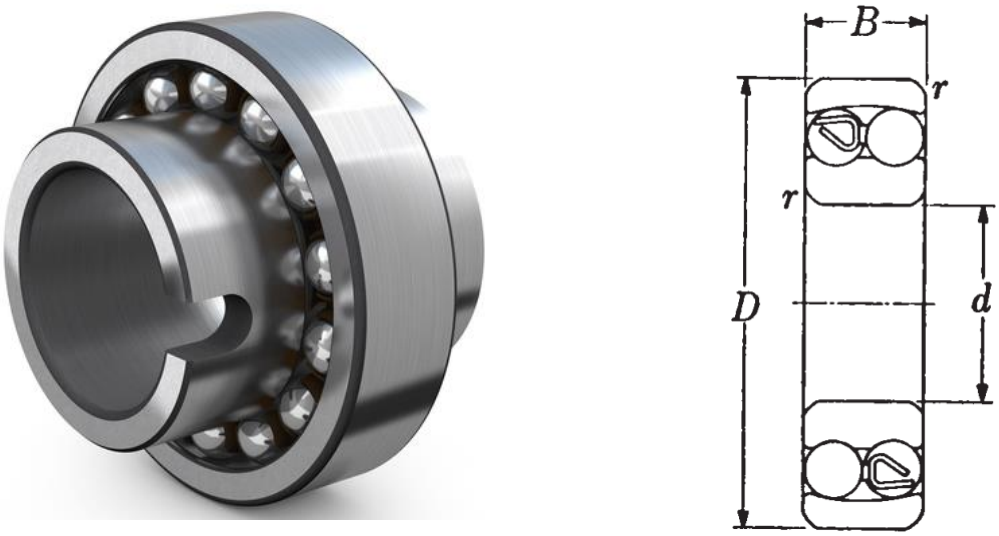

Figure A. 2: Self-aligning ball bearing

Table A. 3: Self-aligning ball bearing specification

Bore d	17 mm
Outer Diameter O.D	47 mm
Width B	14 mm
Fillet Radius r	1.5 mm
Load Ratings	3180N (Static) 12543N (Dynamic)
Weight	130 grams

APPENDIX B:

Flow Visualisation Supplementary Results

B.1: Flow Visualisation around Stationary Turbine

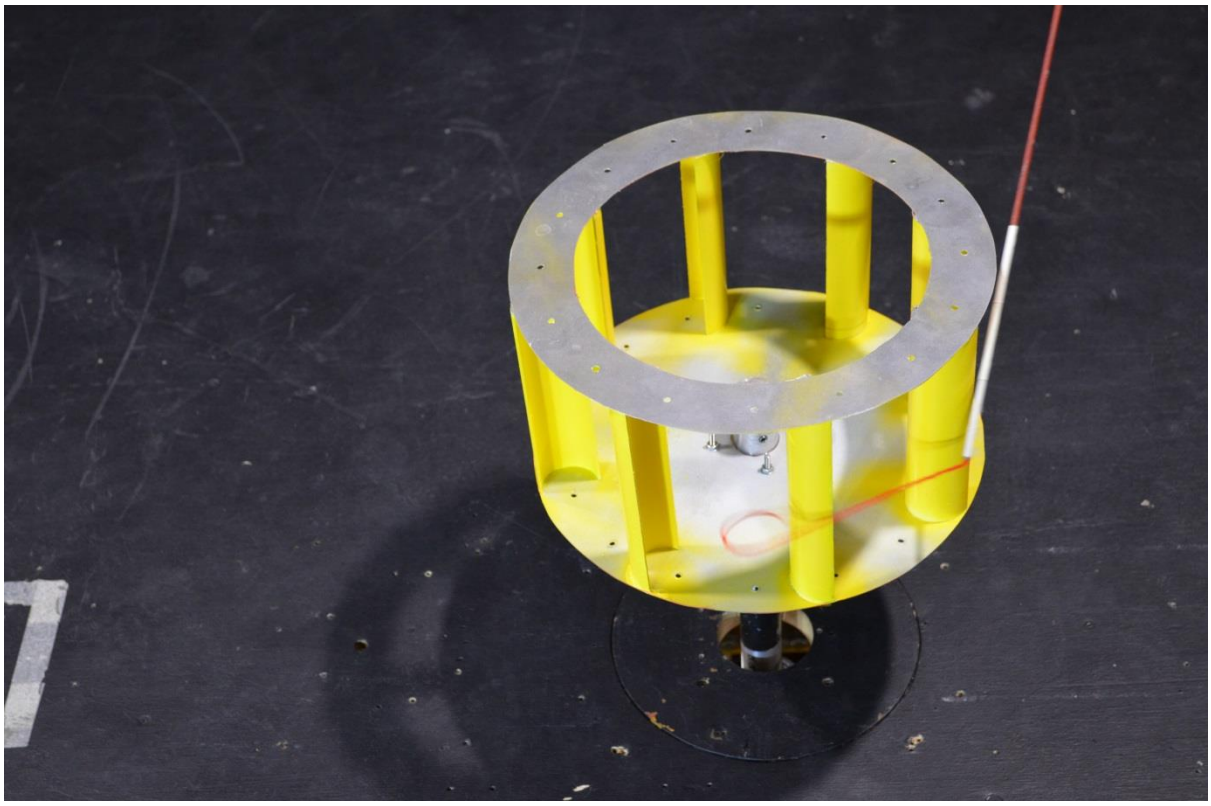

Figure B.1: Side view, eight blade stationary model, 4 m/s

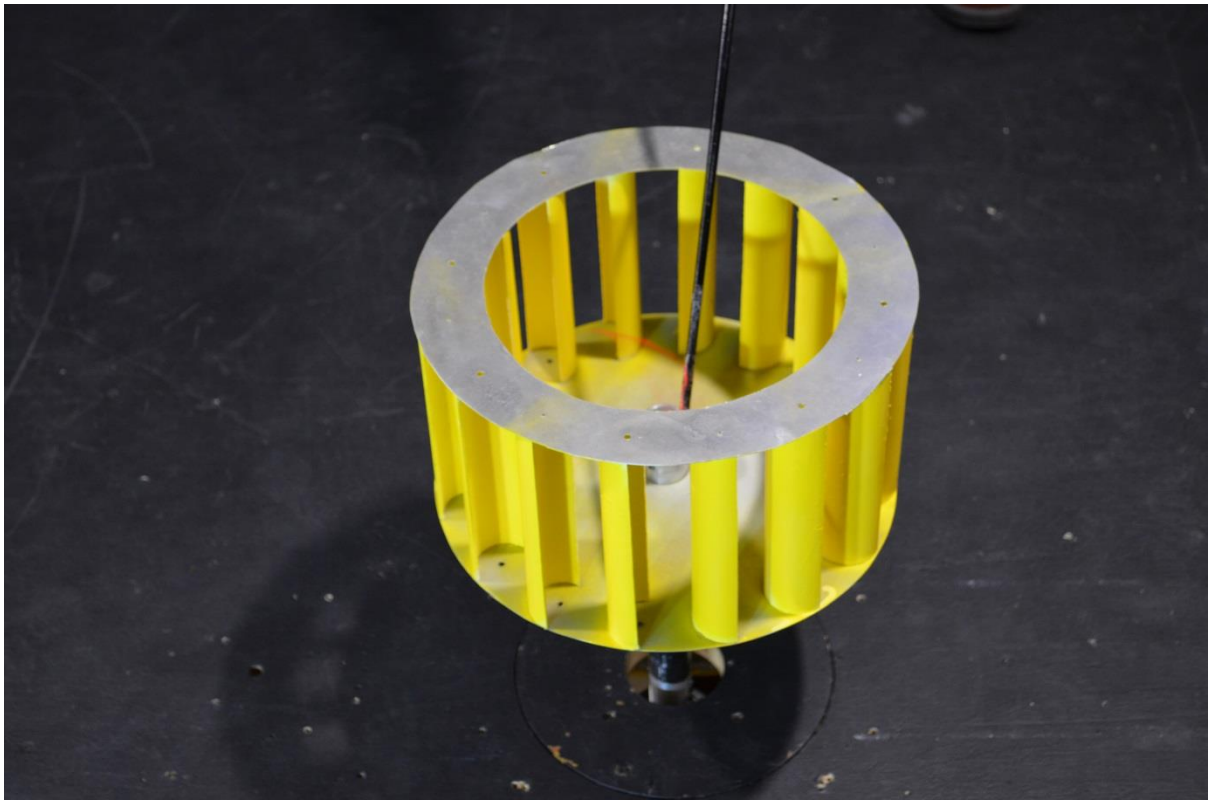

Figure B.2: Side view, sixteen blade stationary model, 4 m/s

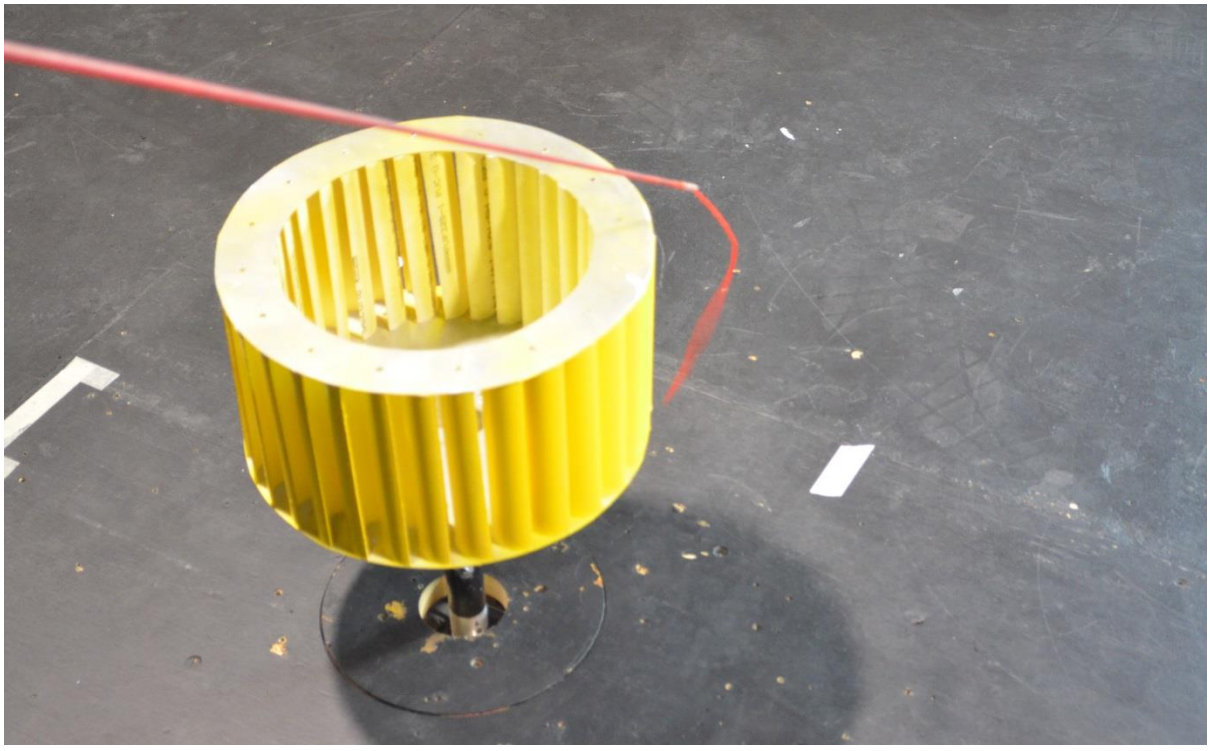

Figure B.3: Side view, thirty two blade stationary model, 4 m/s

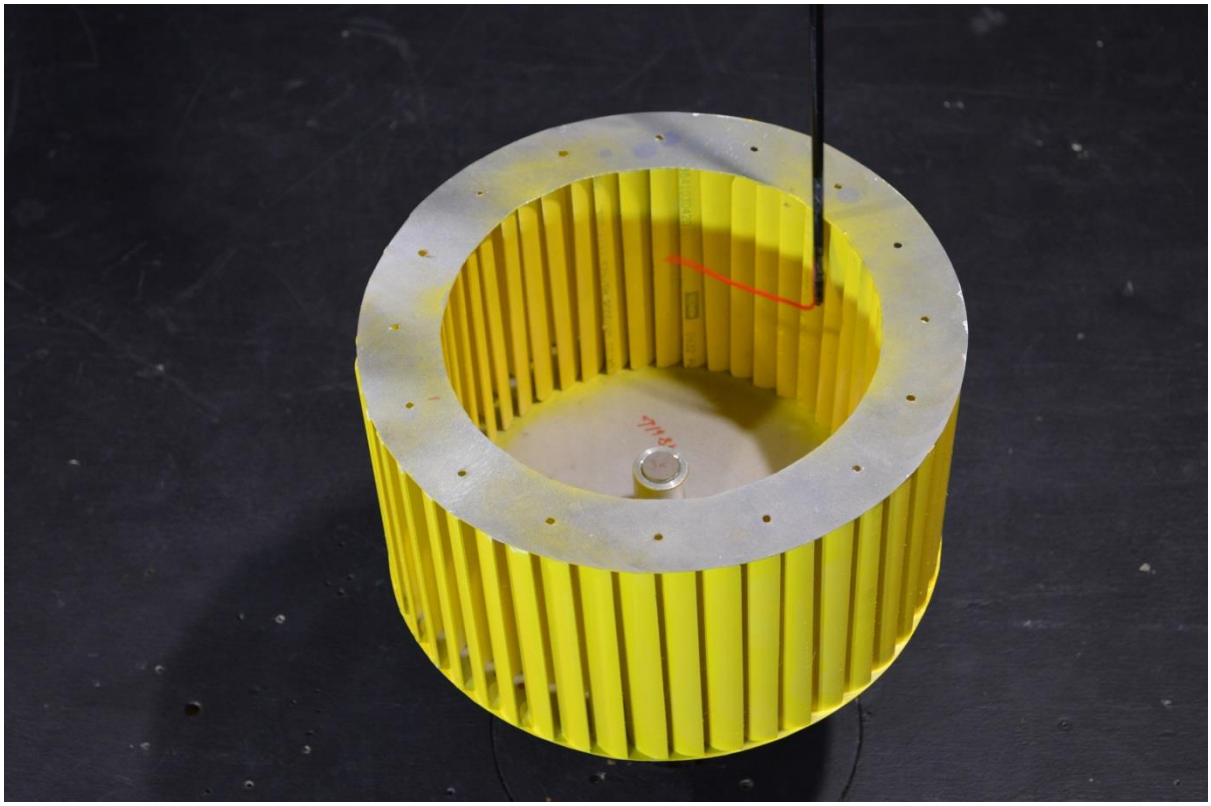

Figure B.4: Side view, forty eight blade stationary model, 4 m/s

B.2: Flow Visualisation around Rotating Turbine

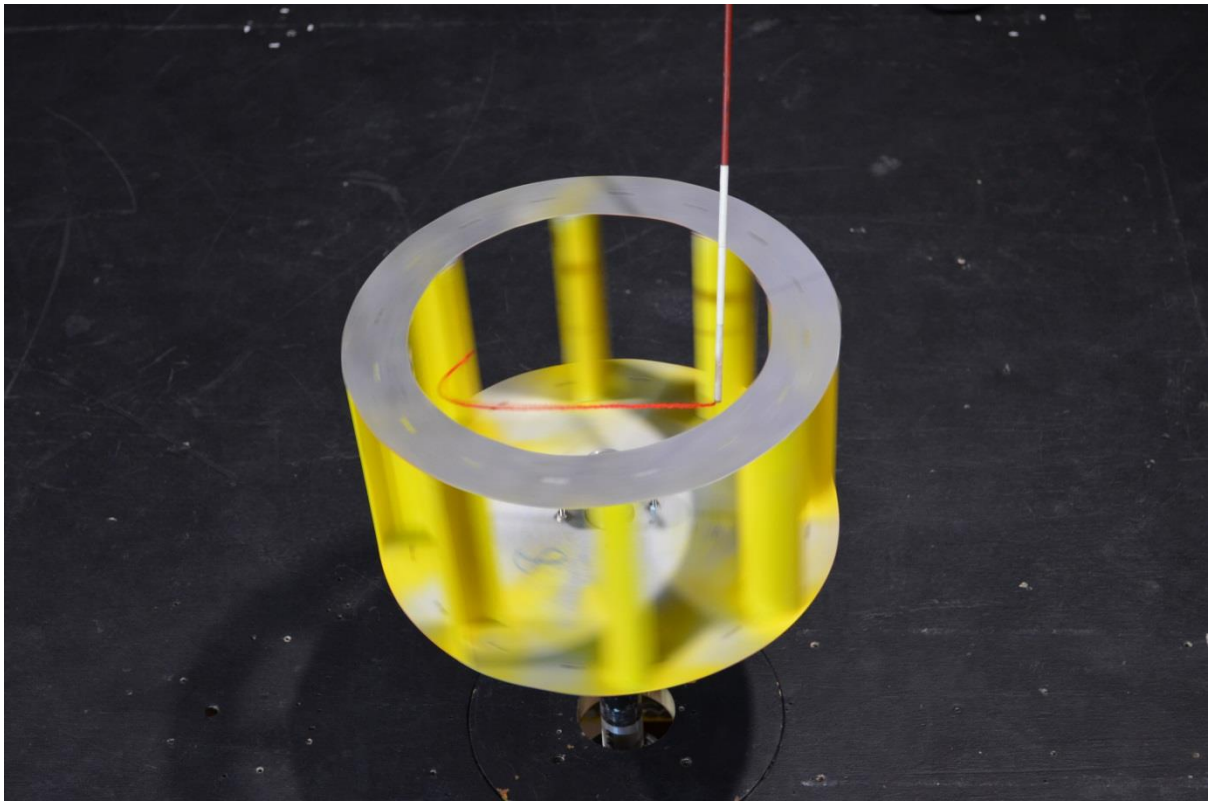

Figure B.5: Side view, eight blade rotating model, 4 m/s

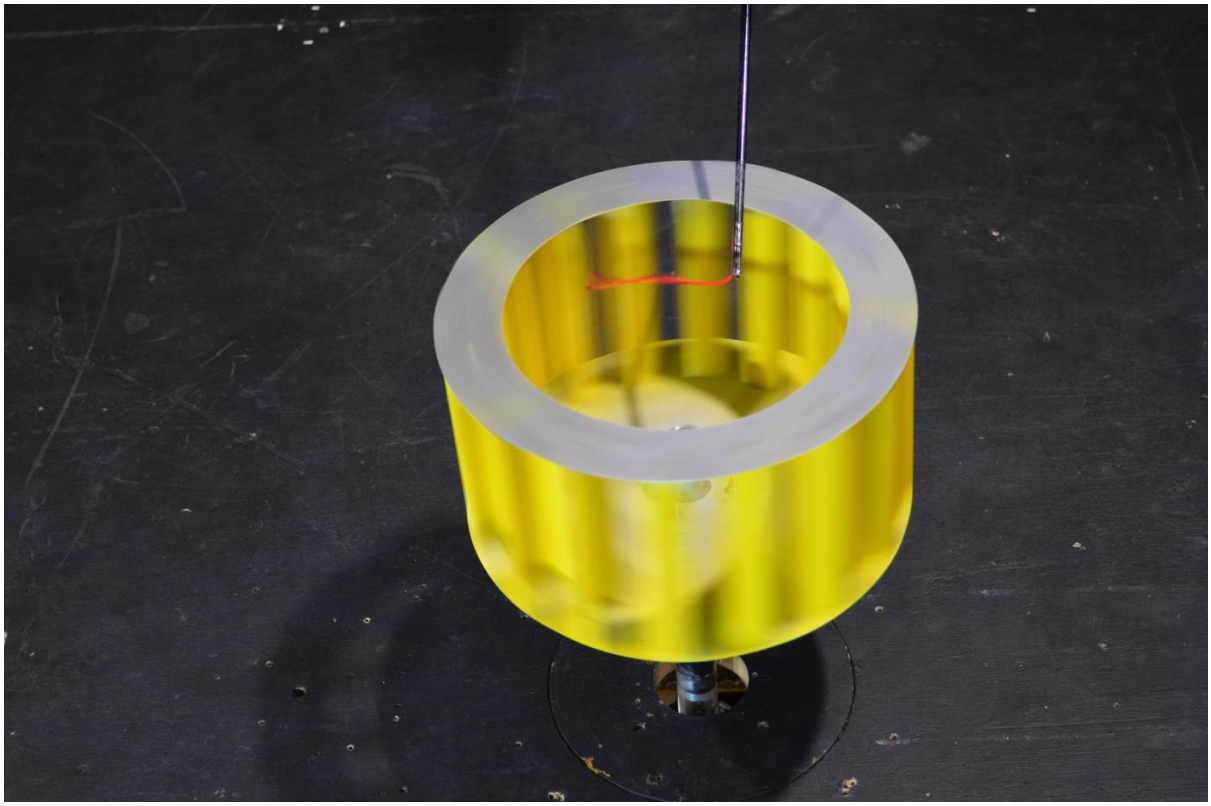

Figure B.6: Side view, sixteen blade rotating model, 4 m/s

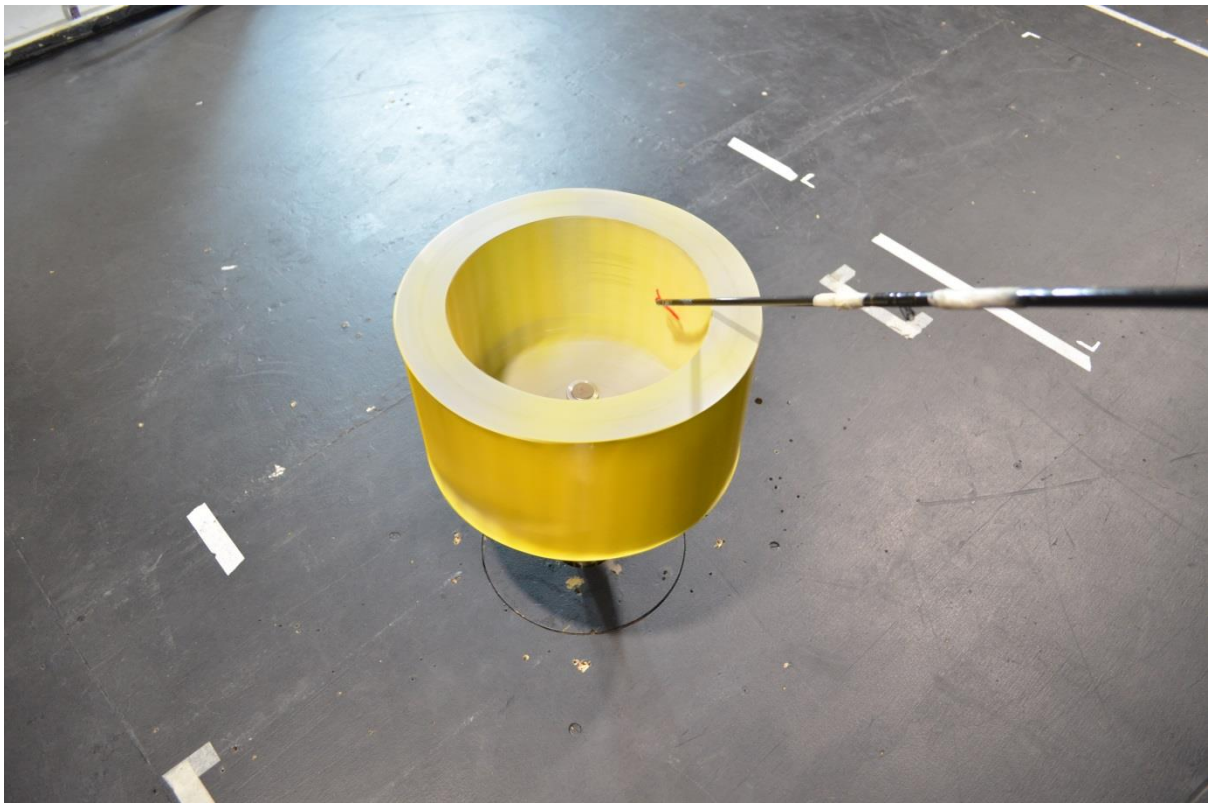

Figure B.7: Side view, thirty two blade rotating model, 4 m/s

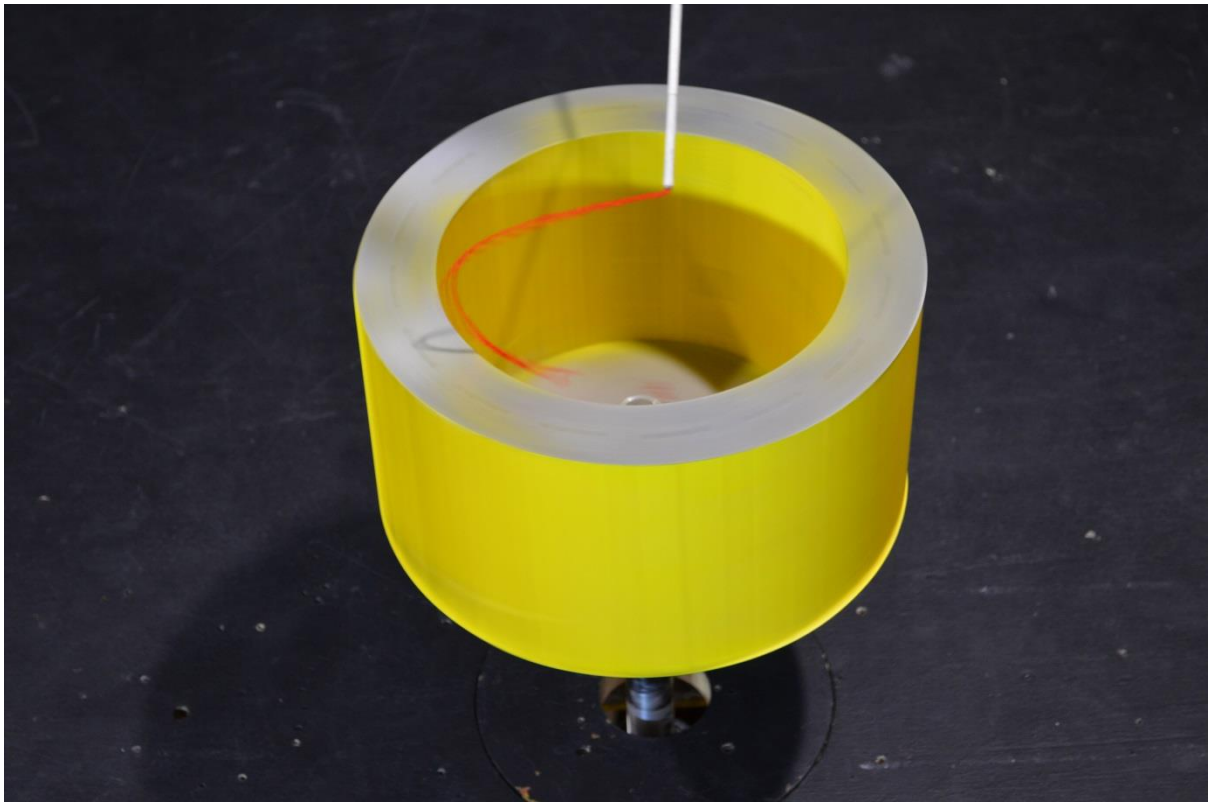

Figure B.8: Side view, forty eight blade rotating model, 4 m/s